

Dissertation
submitted to the
Combined Faculties of the Natural Sciences and Mathematics
of the Ruperto-Carola-University of Heidelberg, Germany,
for the degree of
Doctor of Natural Sciences

Put forward by

BEKDAULET TEMIRBOLATOVICH SHUKIRGALIYEV

born in Zhanaqala, West Kazakhstan region, Republic of Kazakhstan

Oral examination: 28 November 2018

THE LIFE OF STAR CLUSTERS, FROM BIRTH TO DISSOLUTION:
A NEW APPROACH

REFEREES:

PRIV. DOZ. DR. GENEVIÈVE PARMENTIER

PROF. DR. RALF KLESSEN

First edition, September 2018

© Bekdaulet Shukirgaliyev: *The life of star clusters, from birth to dissolution: a new approach,*

This PhD thesis has been carried out by Bekdaulet Temirbolatovich Shukirgaliyev under the supervision of Priv.-Doz. Dr. Eng. Geneviève Parmentier and apl. Prof. Dr. Andreas Just at Astronomisches Rechen-Institut, Zentrum für Astronomie der Universität Heidelberg

*to my parents,
my wife and my children*
in short words: to my family ;-)

ZUSAMMENFASSUNG

Wir untersuchen die Entwicklung von Sternhaufen - von ihrer Geburt in Klumpen aus molekularem Gas bis zu ihrer völligen Auflösung im Gezeitenfeld der Milchstraße. Dazu haben wir Parmentier und Pfalzners (2013) Modell der Sternhaufenentstehung mit direkten N-Körper-Simulationen von Sternhaufen kombiniert, aus denen instantan das bei der Sternentstehung zurückgebliebene Gas ausgestoßen wurde. Unsere Modell-Sternhaufen besitzen ein Sternentstehungseffizienz-(SFE-)Profil, das im Zentrum des Haufens sein Maximum annimmt. Das bedeutet, dass das zurückgebliebene Gas ein flacheres Dichteprofil als die Sterne hat. Wir erzeugen ein großes Gitter von Simulationen, das von drei Parametern - globale SFE, Masse des Sternhaufens und Galaktozentrische Entfernung - aufgespannt wird.

Wir untersuchen, welche unserer Modell-Sternhaufen die instantane Ausstoßung des Gases in der Sonnenumgebung überleben würden. Es zeigt sich, dass eine globale SFE von mindestens 15% nötig ist, damit ein Sternhaufen gravitativ gebunden bleibt. Zudem lässt sich die beobachtete Auflösungszeit von Sternhaufen in der Sonnenumgebung mit unseren Simulationen reproduzieren, falls die Sternhaufenpopulation von Haufen mit niedriger globaler SFE (ca. 15%) dominiert wird. Schließlich können wir zeigen, dass die Überlebensfähigkeit eines Sternhaufen nach instantaner Ausstoßung des Gases, gemessen am Anteil der an den Haufen gebundenen Sterne am Ende der Phase der "violent relaxation", unabhängig vom Gezeitenfeld der Milchstraße ist.

ABSTRACT

We study the evolution of star clusters, starting from their birth in molecular-gas clumps until their complete dissolution in the Galactic tidal field. We have combined the "local-density-driven cluster formation" model of Parmentier and Pfalzner (2013) with direct N-body simulations of star clusters following instantaneous expulsion of their residual star-forming gas. Our model clusters are formed with a centrally peaked star-formation efficiency (SFE) profile, that is, the residual gas has a shallower density profile than stars. We build a large grid of simulations covering the parameter space of global SFEs, cluster masses, sizes and galactocentric distances.

We study the survivability of our model clusters in the solar neighborhood after instantaneous gas expulsion and find that a minimum global SFE of 15 percent is sufficient to produce a bound cluster. Then studying their long-term evolution we find that our simulations are able to reproduce the cluster dissolution time observed for the solar neighborhood, provided that the cluster population is dominated by those formed with a low global SFE (about 15%). Finally, we find that the cluster survivability after instantaneous gas expulsion, as measured by cluster bound mass fraction at the end of violent relaxation, is independent of the Galactic tidal field impact.

PUBLICATIONS

The following publications were used in this thesis:

- Shukirgaliyev, B., G. Parmentier, A. Just, and P. Berczik (2017b). "Impact of a star-formation efficiency profile on the evolution of open clusters." In: *Memorie della Societa Astronomica Italiana* 88, p. 842.
- Shukirgaliyev, B., G. Parmentier, P. Berczik, and A. Just (2017a). "Impact of a star formation efficiency profile on the evolution of open clusters." In: *A&A* 605, A119. DOI: [10.1051/0004-6361/201730607](https://doi.org/10.1051/0004-6361/201730607). arXiv: [1706.03228](https://arxiv.org/abs/1706.03228).
- Shukirgaliyev, Bekdaulet, Geneviève Parmentier, Andreas Just, and Peter Berczik (2018a). "The Long-term Evolution of Star Clusters Formed with a Centrally Peaked Star Formation Efficiency Profile." In: *ApJ* 863, p. 171. DOI: [10.3847/1538-4357/aad3bf](https://doi.org/10.3847/1538-4357/aad3bf).
- Shukirgaliyev, Bekdaulet, Genevieve Parmentier, Peter Berczik, and Andreas Just (2018b). "The star cluster survivability after gas expulsion is independent of the Galactic tidal field impact." In: *MNRAS* (submitted).

I am also the first author or co-author of the following publications which are not included in this thesis:

- Kennedy, Gareth F., Yohai Meiron, Bekdaulet Shukirgaliyev, Taras Panamarev, Peter Berczik, Andreas Just, and Rainer Spurzem (2016). "Star-disc interaction in galactic nuclei: orbits and rates of accreted stars." In: *MNRAS* 460, pp. 240–255. DOI: [10.1093/mnras/stw908](https://doi.org/10.1093/mnras/stw908).
- Panamarev, Taras, Bekdaulet Shukirgaliyev, Yohai Meiron, Peter Berczik, Andreas Just, Rainer Spurzem, Chingis Omarov, and Emmanuil Vilkoviskij (2018). "Star-disc interaction in galactic nuclei: formation of a central stellar disc." In: *MNRAS* 476, pp. 4224–4233. DOI: [10.1093/mnras/sty459](https://doi.org/10.1093/mnras/sty459).
- Shukirgaliyev, Bekdaulet T., Taras P. Panamarev, Aisha Zh. Naurzbaeva, Mukhagali T. Kalambay, Maxim A. Makukov, Emmanuil Y. Vilkoviskij, Chingis T. Omarov, Peter Berczik, Andreas Just, and Rainer Spurzem (2016). "Effect of Gas Accretion Disc Profile on Orbital Parameters of the Accreted Stars." In: *Reports of the National Academy of Sciences of the Republic of Kazakhstan* 5, pp. 5–13.
- Shukirgaliyev, Bekdaulet (2016). "The effect of gaseous accretion disk on dynamics of the stellar cluster in AGN." In: *Star Clusters and Black Holes in Galaxies across Cosmic Time*. Vol. 312, pp. 113–117. DOI: [10.1017/S1743921315007644](https://doi.org/10.1017/S1743921315007644).

CONTENTS

I	INTRODUCTION AND MOTIVATION	1
1	STAR CLUSTERS	3
1.1	General picture of cluster formation and evolution	3
1.2	Bound cluster formation	4
1.3	Star cluster dissolution	6
1.4	Motivation	8
II	METHODS	11
2	INITIAL CONDITIONS	13
2.1	Star-formation efficiency and density profiles	13
2.2	Phase-space distribution of stars at the time of gas expulsion	16
III	RESULTS	23
3	IMPACT OF SFE-PROFILE ON THE EVOLUTION OF OPEN CLUSTERS	25
3.1	Setting up the simulations	25
3.1.1	The tidal field of the Galaxy	25
3.1.2	From N-body to physical units	26
3.2	Cluster-bound fraction evolution	29
3.2.1	Bound fraction of isolated models	29
3.2.2	Bound fraction of non-isolated models	31
3.3	Influence of the cluster initial stellar density	35
3.4	Final bound mass fraction in dependence of SFE	37
3.5	Conclusions	37
4	CLUSTER DISSOLUTION AND CENTRALLY-PEAKED SFE PROFILE	41
4.1	Introduction	41
4.2	Methods	41
4.2.1	Cluster models	41
4.2.2	Random realizations	43
4.2.3	Cluster mass estimates	43
4.3	Stochasticity during cluster expansion	46
4.4	What does cluster dissolution depend on?	48
4.4.1	Cluster life expectancy and initial cluster mass	48
4.4.2	Cluster life expectancy and cluster central density	54
4.5	Discussions and Conclusions	57
5	THE TIDAL FIELD IMPACT ON CLUSTER SURVIVABILITY	61
5.1	Introduction	61
5.2	Parameter space covered by our grid of simulations	63
5.3	The violent relaxation duration	64
5.3.1	Relation between the tidal field impact and the violent relaxation duration	70
5.4	Final bound fraction	74
5.5	Conclusions	78
IV	CONCLUSION	79
6	SUMMARY AND FUTURE WORKS	81
6.1	Summary	81
6.2	Future works	82

V	APPENDIX	85	
A	GASPOTENTIAL ACCELERATION PLUG-IN FOR MKHALO		87
	A.1	Manual	87
	A.2	GASPOTENTIAL code listing	90
	BIBLIOGRAPHY	95	

LIST OF FIGURES

- Figure 1 The simple sketch illustration of star cluster formation and evolution. 4
- Figure 2 SFE profiles of 5 model clusters with $SFE_{gl} = 0.05, 0.10, 0.15, 0.25,$ and 0.40 as a function of outer limit radius R_{cl} given in units of Plummer radius a_* . The black vertical dashed line corresponds to the outer limit adopted in this study $R_{cl} = 10a_*$. The black dotted curve shows the stellar mass of the cluster within the outer limit of R_{cl} . 18
- Figure 3 Relation between the SF duration (t_{SF}) (given in N-body units according to Eq.21) and the global SFE (SFE_{gl}), measured inside $R_{cl} = 10a_*$. The lowest value of the global SFE here in this plot is $SFE_{gl} = 0.007$, which corresponds to an SF duration $t_{SF} = 0.01$ [NB]. 19
- Figure 4 Density profiles of the star cluster (black dashed line), of the residual (solid lines), and initial (dash-dotted lines) gas for different SFE_{gl} in scaled physical units. A total stellar mass $M_* = 3000 M_\odot$ and a 3D half-mass radius $r_h = 1$ pc are assumed. Note that the stellar density profile is a Plummer profile. 20
- Figure 5 Lagrange radii evolution for simulations with an external potential for two different values of $t_{SF} = 0.5$ NBU (top panel) and 100 NBU (bottom panel), which correspond to $SFE_{gl} = 0.02$ and 0.47 respectively. The simulations are quite stable even with very low SFE, which shows that our models are initially in equilibrium with the external potential of the residual gas clump. 21
- Figure 6 Time evolution of the bound fraction F_b of isolated models ($N = 10^4$) as defined by two methods: defined by the fraction of stars with a negative total energy (solid lines), and defined by recalculating the total energy of stars in an iterative process (see text for details; dashed lines). The vertical dotted line corresponds to $t = 20$ Myr when we scale the isolated models with the same scale factor as for a non-isolated model with $M_* = 6000 M_\odot$, which also has $N \approx 10^4$. 29
- Figure 7 Top panel: bound and final bound fraction evolution of an isolated cluster with $SFE_{gl} = 0.15$ (solid and dashed lines, respectively). Bottom panel: Lagrange radius evolution of the same model. Lagrange radii are given in units of the initial stellar half-mass radius. 30

- Figure 8 Evolution of the bound fraction of clusters obtained in our simulations. Different colors correspond to different global SFEs (see the key). The gray lines show the impact of mass loss caused by stellar evolution alone. The vertical dotted line corresponds to $t = 20$ Myr. Top panel: comparison of the bound fraction evolution of isolated (dashed lines) and non-isolated (solid lines) models for $M_{\star} = 6000 M_{\odot}$ with $N \approx 10^4$ stars. Note that the isolated models are the single-mass models without stellar evolution and scaled to the same physical units as the non-isolated models (i.e., $M_{\star} = 6000 M_{\odot}$ and $r_h = 1.26$ pc). Bottom panel: bound fraction (instantaneous tidal mass as a fraction of initial stellar mass) evolution for non-isolated models with different initial stellar masses (see the key for the line-coding). [32](#)
- Figure 9 Different random realizations (see line types in the key) of the model clusters with $M_{\star} = 6000 M_{\odot}$ ($N = 10455$ stars) for $r_h/R_J = 0.052$. [33](#)
- Figure 10 Evolution of a non-isolated cluster of the solar neighborhood with $SFE_{gl} = 0.20$, $M_{\star} = 6000 M_{\odot}$ and $r_h/R_J = 0.052$ over 50 Myr after gas expulsion. We show 49 Lagrange radii, ranging from 2 percent to 98 percent in intervals of 2 percent (solid and dashed lines). The instantaneous tidal radius R_J of the cluster is shown as the dotted line. Thick solid lines correspond to every 10 percent of the Lagrange radius, and the dashed line corresponds to 50 percent of the Lagrange radius. [34](#)
- Figure 11 Evolution of the bound fraction of $M_{\star} = 15000 M_{\odot}$ clusters with different impact of the tidal field (see the key for the line-coding). Different colors correspond to different global SFEs (see the key for the color-coding). [35](#)
- Figure 12 Evolution of the cluster with $M_{\star} = 6000 M_{\odot}$, $SFE_{gl} = 0.20$ and $r_h/R_J = 0.025$ over the first 50 Myr after the instantaneous gas expulsion. [36](#)
- Figure 13 Bound fraction as a function of global or effective SFE. We compare our results (red lines) with previous works. The isolated models are depicted by the red diamonds, and non-isolated models by red crosses. In the top panel we use our global SFE (SFE_{gl}) and in the bottom panel, the eSFE, $eSFE = 1/Q_{\star}$ (which is almost the same as the LSF, the local stellar fraction of our models). [38](#)

- Figure 14 Volume density maps of clusters with a birth mass of $M_{\star} = 15000M_{\odot}$ projected onto the Galactic plane. The left and middle columns correspond to two random realizations of a model cluster with $SFE_{gl} = 0.15$, and the right column corresponds to a $SFE_{gl} = 0.25$ model. From top to bottom, we provide 5 different snapshots of each model cluster at times $t = 0, 5, 10, 30, 70$ Myr. Each point corresponds to one star whose color-coding depicts the local volume density calculated by means of a 50-nearest-neighbor scheme. *Note: the color-scale does not show densities higher than $100 M_{\odot}pc^{-3}$ in order to show the color contrast in low density regions at a later time of cluster evolution. The central densities at the time of gas expulsion are as high as $1.6 \cdot 10^3 M_{\odot}pc^{-3}$. The dashed circles correspond to R_J and $2R_J$. The bound fractions at $t = 30$ Myr are, from left to right: $F_{bound} = 0.06, 0.18$ and 0.5 . The corresponding dissolution times are $t_{dis} = 0.3$ Gyr, 1.2 Gyr and 2.9 Gyr, respectively.* 45
- Figure 15 Volume density profiles of model clusters whose birth mass is $M_{\star} = 15000M_{\odot}$ (same models as in Fig. 14). Each point represents the density at the location of one star. Left and middle panels correspond to two random realizations of the $SFE_{gl} = 0.15$ model, while the right panels correspond to the $SFE_{gl} = 0.25$ model cluster. The top and bottom panels correspond to the density profiles calculated at $t = 30$ Myr and $t = 70$ Myr, respectively. In each panel, the vertical lines show the location of $1R_J$ and $2R_J$. The horizontal lines correspond to the mean density within one Jacobi radius, $\langle\rho_J\rangle$, which is constant for the considered Galactic orbit of star clusters. 46
- Figure 16 The mean bound mass fractions at the end of violent relaxation obtained from random realizations of cluster models with $SFE_{gl} = 0.15$ as a function of the birth mass of star clusters. The error-bars correspond to the standard deviations. The solid line shows mean bound mass fraction of all model clusters with $SFE_{gl} = 0.15$ and shaded area corresponds to the standard deviation. 47
- Figure 17 Cluster dissolution time as a function of bound mass fraction. Cluster birth mass and global SFE are indicated by colors and symbols, respectively, according to the key. 49

Figure 18

Star cluster dissolution time versus cluster mass at the end of violent relaxation ($t = 30$ Myr in top panels and $t = 70$ Myr in bottom panels). We refer to this as the cluster “initial” mass. The left panels show the cluster “initial” mass defined as the Jacobi mass, M_J , while the right panels present it as the “extended mass”, M_{2J} . Each point represents one cluster model, with the color-coding defining the cluster birth mass, and marker shapes coding the global SFE. The solid line with shaded area corresponds to the cluster disruption model for the solar neighborhood of Lamers et al. (2005). The dashed and dash-dotted lines depict the best fits to high-SFE ($SFE_{gl} \geq 0.20$) and low-SFE ($SFE_{gl} = 0.15$) model clusters. The red curve in the lower-right panel connects the median random realizations of the models with $SFE_{gl} = 0.15$. 50

Figure 19

Cluster dissolution time as a function of extended mass at $t = 70$ Myr. The $SFE_{gl} = 0.15$ models are represented by the mean extended mass and mean dissolution time per model with error-bars representing the standard deviations. The red curve connects median random realizations of each model as in the lower right panel of Fig. 18. The dashed, dotted and dash-dotted lines are best fits to the $SFE_{gl} \geq 0.20$, $SFE_{gl} = 0.17$ and $SFE_{gl} = 0.15$ models. The solid line with shaded area corresponds to the MDD relation of Boutloukos and Lamers (2003) for the solar neighborhood (Lamers et al., 2005). 52

Figure 20

Histogram of model clusters by dissolution times for low-SFE and high-SFE clusters (blue and orange lines, respectively). The area subtended by each histogram is unity. 53

Figure 21

Cluster dissolution time as a function of Roche volume filling factor at $t = 30$ and $t = 70$ Myr (top and bottom panels, respectively). In the left panels, the cluster initial mass is estimated as the Jacobi mass, M_J , while in the right panels it is estimated as the extended mass, M_{2J} . Cluster initial masses are shown by the color-coding presented on the right-hand-side color-bar. The half-mass radius, r_h , is measured as the radius containing half of the cluster initial mass and marked as r_h^J when $M_{init} = M_J$ and r_h^{2J} when $M_{init} = M_{2J}$. The gray arrows indicate those $M_* = 15k M_\odot$ model clusters presented in Figs. 14 and 15. 55

- Figure 22 Cluster dissolution time, t_{dis} (top panels) and cluster Jacobi mass, M_J (bottom panels), as functions of volume density contrast between cluster center and outskirts, ρ_c/ρ_J (Eq. 33) measured at $t = 30$ Myr and $t = 70$ Myr (left and right panels, respectively). Unlike in Fig. 18 the color-coding refers to the cluster Jacobi mass at quoted ages in top panels, and to the cluster dissolution time in bottom panels. The best fits (Eq. 34-35) are shown with black curves. The three $M_\star = 15000M_\odot$ model clusters presented in Fig. 14 and Fig. 15 are indicated with the arrows in each panel in the same order, i.e. from left to right, as the corresponding panels of Fig. 14 and Fig. 15. 56
- Figure 23 The rotation curve of the Galaxy model (thick blue line) and its corresponding components (bulge, disc and halo). The black open circles show the radii of the circular orbits on which we put our model clusters: $R_{\text{orb}} = 2.9, 4.64, 8.0, 10.95, 18.0$ kpc. 64
- Figure 24 The bound mass fraction evolution of $M_\star = 30k M_\odot$ clusters for different tidal field impacts. The top panels present the solar neighborhood clusters ($R_{\text{orb}} = 8$ kpc) where the tidal field impact r_h/R_J varies with cluster size r_h (i.e. different mean densities) at the time of instantaneous gas expulsion. The bottom panels show clusters of identical size, but placed at different Galactocentric distances. Therefore the tidal field impact r_h/R_J varies with the Jacobi radius R_J . Left and right panels show the low-SFE (i.e. $\text{SFE}_{\text{gl}} = 0.15$) and high-SFE (i.e. $\text{SFE}_{\text{gl}} = 0.25$) clusters, respectively. The thin vertical dashed lines indicate the end of violent relaxation, which we obtain in this section and whose values are provided in Table 8. 67
- Figure 25 The characteristic mass-loss time (top panels) and the bound mass fraction evolution (bottom panels) of star clusters at two Galactocentric distances $R_{\text{orb}} = 2.9$ kpc and $R_{\text{orb}} = 18$ kpc are shown in left and right panels, respectively. The different colors correspond to cluster global SFEs in such a way that $\text{SFE}_{\text{gl}} = 0.15$ (red), 0.17 (blue), 0.20 (green), and 0.25 (yellow). The red thick line in upper panels corresponds to the median of all simulations at a given time (irrespective of global SFE and birth mass). The black dots show the characteristic mass-loss time of stellar evolution only and correspond to two simulations with $M_\star = 10^5 M_\odot$. The black solid line is the best fit to stellar evolutionary mass loss characteristic time. In bottom panels the black line shows the stellar evolutionary mass-loss of a $M_\star = 10^5 M_\odot$ cluster. In each panel the vertical blue dashed line corresponds to the end of violent relaxation, t_{VR} , with shaded area corresponding to the standard deviation (see the text for more explanations). 69

- Figure 26 The end of violent relaxation as a function of the tidal field impact, characterized by half-mass to Jacobi radii ratio r_h/R_J at the time of gas expulsion. Each point represents all cluster models for a given tidal field impact. The black cross and the green open circle correspond to our ‘standard’ model set ($r_h/R_J = 0.052$ and $R_{orb} = 8.0$ kpc), where the former shows our earlier estimate from Chapter 3 and the latter corresponds to the new generalized estimate obtained in Section 5.3. The models marked with plus symbols are at different Galactocentric distances, while crosses indicate solar neighborhood clusters with different densities, therefore with different impact of the tidal field. 71
- Figure 27 The end of violent relaxation duration as a function of the tidal field impact for the same clusters located at different Galactocentric distances. The solid line is the best fit power-law function. The dashed line corresponds to $t_{VR} \propto R_J$. 72
- Figure 28 The violent relaxation duration as a function of the impact of the tidal field at a fixed Galactocentric distance. The solid line is the best fit power-law function. The dotted lines correspond to $t_{VR} \propto \sqrt{r_h}$ going through the most extreme models. The dashed horizontal line is the mean over all simulations of the solar neighborhood with the shaded area showing the standard deviation. 73
- Figure 29 The final bound mass fraction as a function of cluster birth mass. Panels from top to bottom correspond to three Galactocentric distances of $R_{orb} = 2.9, 8.0, 18.0$ kpc. The corresponding tidal field impacts are: $r_h/R_J = 0.10, 0.052, 0.03$, respectively. The color-coding corresponds to different global SFEs as following: $SFE_{gl} = 0.15$ (red), 0.17 (blue), 0.20 (green), and 0.25 (yellow) and are the same as in Fig. 25. Each point corresponds to the mean and standard deviation of the random realizations performed for each model. 75
- Figure 30 The final bound mass fraction as a function of tidal field impact for different Galactocentric distances. The color-coding corresponds to the global SFE and is the same as in Fig. 29. Each point corresponds to the mean and standard deviation of model clusters with the same global SFE and tidal field impact. 76
- Figure 31 The bound mass fraction at the end of violent relaxation as a function of tidal field impact for different central densities at $R_{orb} = 8.0$ kpc. Different colors correspond to different global SFEs. Each point corresponds to the mean and standard deviation of clusters with the same global SFE at a given tidal field impact. 76

Figure 32

The final bound fraction as a function of global SFE and the tidal field impact. The different colors correspond to the clusters with different the tidal field impact of our model clusters. Green open circles show our So-models. The solar neighborhood clusters with different tidal field impact are shown by cross symbols, while clusters at different Galactocentric distances are presented by plus symbols. Each point correspond to a mean bound fraction of a set of simulations with a given global SFE and r_h/R_J . Each set of simulations consist of models with birth masses range from 3k to 30k M_\odot at least. Black curves correspond to the results of Baumgardt and Kroupa (2007) for the case of instantaneous gas expulsion, where the numbers shown next to black dots the strength of the tidal field in their simulations. 77

LIST OF TABLES

Table 1	Global SFEs (SFE_{gl}) and their corresponding SF durations (t_{SF}) in N-body units (see Eq. 21), the virial ratios Q_* of star clusters, and eSFEs immediately after gas expulsion. 20
Table 2	The numerical values of the Galaxy component parameters from Eq. 24. 25
Table 3	Set of models corresponding to different initial stellar masses. 27
Table 4	Global SFEs (SFE_{gl}) and corresponding values of the SF duration (t_{SF}) in N-body units (Eq. 21) and in units of Myr for the adopted normalization parameters (using Eq. 29). The rows within the box highlight the non-isolated models selected for our simulations. We also show here the mean volume density of the clump (star + gas) inside the half-mass radius. Because we kept the stellar masses constant while varying the global SFE, we varied the fraction of unprocessed gas. When the global SFE increases, the mass of the residual gas decreases (keeping stellar mass constant), and as a consequence, the total volume density decreases as well. 28
Table 5	Scaling factors to the physical time and duration of 20 Myr in N-body units corresponding to different ratios of the cluster half-mass to tidal radius. 35
Table 6	Model cluster parameters. The columns are as follow: (1) total number of stars, (2) birth mass, (3) global SFE, (4) number of random realizations per model (number of those calculated till cluster dissolution), (5) mean bound mass fraction at the end of violent relaxation and its standard deviation when more than one random seed, (6) mean dissolution time. 42

Table 7	Number of random realizations performed for each model cluster, where each model is described by its birth mass (M_*), global SFE and tidal field impact (r_h/R_J). 65
Table 8	End of violent relaxation for different tidal field impacts. 69

Part I

INTRODUCTION AND MOTIVATION

STAR CLUSTERS

The evolution of galaxies and of the Universe as a whole is tightly related to the process of star formation (SF). Stars do not form in isolation and almost all star-forming regions contain star clusters, which are fundamental building blocks of galaxies. Thus constructing a comprehensive picture of how clusters form and evolve is very important to our overall understanding of the star formation process. Some of the massive and dense clusters (e.g. globular clusters) can remain bound and survive for a Hubble time, but most clusters (e.g. open clusters) dissolve shortly after they form and in doing so contribute to the field star population. Therefore, open clusters represent the intermediate stage between the clumpy structure of the interstellar medium and the relatively smooth stellar distribution of a galaxy. As such, they bear crucial information regarding the star-formation histories of galaxies and their evolution.

Star clusters form in dense regions of giant molecular gas clouds, which collapse and form stars. In some cases the mutual gravitational potential of stars can keep them together in clusters for millions and billions of years after formation. Stars in a given cluster, since they formed from the same material and roughly at the same time, have similar ages and chemical compositions. Thereby star clusters became an excellent laboratory to test the stellar evolution theory, by fitting isochrones - same age curves in color-magnitude diagram (Johnson, 1954; Meyer-Hofmeister, 1969). Applying stellar population synthesis models, one can estimate the cluster ages from the collective spectral and photometric properties of stars in clusters (Bruzual and Charlot, 2003). From the age and mass distributions of star clusters one can probe the star-formation history of their host galaxies. But star clusters do not stay the same as they formed initially. They evolve dynamically and can dissolve in the tidal field of the host galaxy. To study the past of a galaxy from the present day properties of its star clusters we need to understand well, how these stellar systems form and evolve through the time.

1.1 GENERAL PICTURE OF CLUSTER FORMATION AND EVOLUTION

Star formation takes place in collapsed cold dense gas clumps in the turbulent molecular cloud gas and produce many stars at a time. Star formation itself is a complicated process and is still being investigated. Once thermonuclear reactions start in the core of the first stars, these stars start to heat, ionize and drive the residual gas out of the star-formation region. The most massive stars are the most destructive for the parent star-forming gas clump with their strong winds, radiation pressure, ionizing radiation and eventually explosion as Super-Novae type II, blowing up the gas from the star-forming region within the first few million years of star-formation. The collective stellar feedback from all stars can terminate star formation and clean the star cluster from its residual gas totally.

The star-formation efficiency (SFE), that is the mass fraction of star-forming gas converted into stars, is usually below 30 percent in star-forming regions of the solar vicinity (Lada and Lada, 2003). That is, more than 70 percent of the total mass escapes from star-forming region thereby weakening the gravitational potential of star clusters significantly. The weakening of the cluster gravitational potential by the residual gas expulsion drives the cluster away from virial equilibrium, possibly causing its expansion depending on the

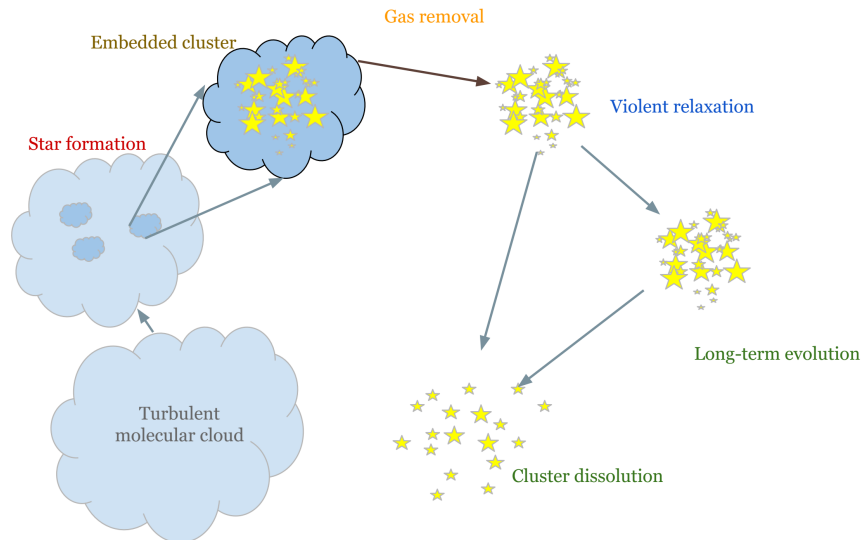


Figure 1: The simple sketch illustration of star cluster formation and evolution.

cluster dynamical state during the gas embedded phase. The evolution of star clusters from the state of dynamical non-equilibrium into a new state of equilibrium is called violent relaxation. During the violent relaxation star clusters can lose their stars, change their structures and masses and even dissolve without reaching a new virial equilibrium. Lada and Lada (2003) reported about high infant mortality of star clusters in the solar neighborhood by analyzing the star cluster age distribution.

Star clusters we observe today as dynamical systems in equilibrium and which have lived for many million years are those clusters who survived the gas expulsion and violent relaxation as gravitationally bound stellar systems. These star clusters then dissolve as time goes by, affected by several cluster dissolution mechanisms like the evaporation by two-body relaxation, stellar evolutionary mass-losses or tidal stripping by the host galaxy.

The general picture of star cluster life described above is illustrated with the simple sketch in Fig 1.

Nevertheless, the life of star clusters is not as simple as depicted above. Each phase of a cluster life, from star-formation till dissolution, has many aspects we still do not know in detail.

1.2 BOUND CLUSTER FORMATION

The formation of bound star clusters can be divided into three phases: 1) SF 2) expulsion of the residual star-forming gas, and 3) violent relaxation, that is, the cluster dynamical response to gas expulsion. The dynamics of stars in young clusters during their formation and after gas expulsion is not fully understood yet. It has been the object of intense scrutiny over the past years, with the applied methods ranging from pure N-body simulations (Baumgardt and Kroupa, 2007; Boily and Kroupa, 2003b; Goodwin, 2009; Lada, Margulis, and Dearborn, 1984; Lee and Goodwin, 2016; Proszkow and Adams, 2009; Smith et al., 2011; Tutukov, 1978) and combined hydrodynamical and N-body simulations (Bonnell et al., 2011; Fujii and Portegies Zwart, 2016; Girichidis et al., 2012; Moeckel et al., 2012) to analytical and semi-analytical models (Adams, 2000; Boily and Kroupa, 2003a; Hills, 1980; Parmentier and Pfalzner, 2013).

Star clusters form in dense ($> 5\text{-}10 \times 10^3 \text{cm}^{-3}$) clumps of gas inside giant molecular clouds (GMC) (Kainulainen, Federrath, and Henning, 2014; Lada, Lombardi, and Alves, 2010; Lada and Lada, 2003). The global SFE (SFE_{gl}), the mass fraction of a star-forming region converted into stars, is defined as

$$\text{SFE}_{\text{gl}} = \frac{M_{\star}}{M_{\text{gas}} + M_{\star}}, \quad (1)$$

where M_{\star} is the total stellar mass and M_{gas} is the mass of unprocessed gas.

The SFE measured from observations vary from a few to 30 percent for the dense clumps of molecular clouds (Higuchi et al., 2009; Lada and Lada, 2003), and from 0.1 percent to a few percent for their host giant molecular clouds (Evans et al., 2009; Murray, 2011).

Several mechanisms (stellar winds, ionizing radiation, radiation pressure, Type II supernova explosions) interrupt the SF process and blow up the unprocessed gas out of the cluster (Dib et al., 2013; Hopkins et al., 2013; Krumholz and Matzner, 2009; Murray, Quataert, and Thompson, 2010). The observed open clusters older than 10 Myr are already gas free (Lada and Lada, 2003; Leisawitz, Bash, and Thaddeus, 1989). The duration of SF is of the order of 1 Myr, with observations of young star clusters revealing stellar age spreads ranging approximately between 0.3 Myr and 5.0 Myr (Kudryavtseva et al., 2012; Reggiani et al., 2011).

The combination of the SF duration with the SFE per free-fall time determines the global SFE achieved by a cluster-forming clump at the time of gas expulsion. The SFE per free-fall time, the fraction of gas mass converted into stars over one free-fall time, was estimated to be 0.01 by Krumholz and Tan (2007), while Murray (2011) suggested that it varies between 0.01 and 0.50 depending on the GMC mass.

Baumgardt and Kroupa (2007) performed a grid of simulations assuming an embedded cluster in virial equilibrium with the residual gas, where both mass density profiles have identical shapes. From these N-body simulations (see also Fig. 1 in Parmentier and Gilmore (2007) for an overview of earlier works) it was concluded that a global SFE of at least 33 percent is needed to form a bound cluster after instantaneous gas expulsion. This minimum global SFE is slightly higher than the SFEs observed for molecular clumps, which vary up to 30 percent and are frequently estimated to be around 10 percent (Higuchi et al., 2009; Kainulainen, Federrath, and Henning, 2014; Murray, 2011). To address this discrepancy between theoretical works and observations, different solutions exist: adiabatic gas expulsion (Baumgardt and Kroupa, 2007; Brinkmann et al., 2017; Geyer and Burkert, 2001; Lada, Margulis, and Dearborn, 1984), a subvirial cluster at the time of gas expulsion (Farias et al., 2015; Goodwin, 2009; Verschueren and David, 1989), or hierarchically formed clusters (Lee and Goodwin, 2016; Smith et al., 2011).

Goodwin (2009) stressed that the critical factor for a cluster to survive gas expulsion is its dynamical state (as measured by its virial ratio) at the onset of gas expulsion, and not its global SFE. Because star clusters are not necessarily in equilibrium with the potential of their clump, he introduced an alternative SFE derived from the virial ratio of a star cluster measured immediately after instantaneous gas expulsion and called the effective SFE, or eSFE (see also Goodwin and Bastian (2006)):

$$\text{eSFE} = \frac{1}{2Q_{\star}}, \quad (2)$$

with the virial ratio defined by

$$Q_{\star} = \frac{T_{\star}}{|\Omega_{\star}|}. \quad (3)$$

Here T_* and Ω_* are the total kinetic and potential energies of a star cluster immediately after gas expulsion, and $Q_* = 0.5$ corresponds to virial equilibrium. The eSFE is equivalent to the global SFE for these models, where the SFE is constant with the distance to the center of the star-forming clump (i.e., stars and gas follow the same density profile shape), and stars are in virial equilibrium with the gravitational potential of residual gas. According to Goodwin (2009), clusters whose virial ratio is $Q_* < 1.5$ (equivalent to $\text{eSFE} > 0.33$) can survive the instantaneous gas expulsion.

Smith et al. (2011, 2013) and Farias et al. (2015) studied this problem by proposing a hierarchical merging scenario of substructured embedded clusters. They also concluded that the dynamical state of a cluster at the time of gas expulsion is important to cluster survival, while the global SFE is not. However, their distributions of stars and star-forming gas are different, while not depending on each other.

The more recent work by Lee and Goodwin (2016) proposed different dynamical states for the subclusters, which are in virial equilibrium with each other within the cluster-forming region. The authors also concluded that the total dynamical state of the whole cluster at gas expulsion onset is the most important factor in predicting whether the cluster survives gas expulsion. They did not link the formation of a bound cluster to its global SFE, however, and, considered only eSFEs. One could nevertheless map their virial ratio to a subcluster mean SFE, assuming that in each subcluster, stars and gas present the same density profile shape.

Parmentier and Pfalzner (2013), however, proposed a semi-analytical model of cluster formation in which the density profile of the embedded cluster is steeper than that of the cluster-forming gas. That is, the SFE varies locally, as it steadily increases from the clump outskirts to the clump inner regions (see Fig. 10 in Parmentier and Pfalzner (2013)). The reason is that the cluster-forming clump is denser, and therefore experiences faster SF, in its central regions than in its outskirts. The results of the cluster formation model of Parmentier and Pfalzner (2013) also explain the star-formation relation between the surface densities of gas and young stellar objects observed in eight nearby molecular clouds by Gutermuth et al. (2011).

The dynamical response to gas expulsion of a cluster where the stellar volume density profile is steeper than that of the gas differs from the most often investigated cases where the gas and stars density profiles have identical shapes. This was first investigated by Adams (2000) with a semi-analytical method. His choice for different gas and star density profiles was not physically motivated, however. Adams (2000) showed that if the stellar mass is more concentrated in the cluster center than the gas mass, the cluster survival probability is significantly increased (see his Fig. 3). The reason is a gas-poor region in the cluster central regions, which promotes the formation of a bound cluster, even when the global SFE is low. In addition, Pfalzner et al. (2014) performed N-body simulations whose initial conditions build on the model of Parmentier and Pfalzner (2013) for a global SFE of about 18 percent.

1.3 STAR CLUSTER DISSOLUTION

Although surviving bound star clusters reach a quasi-equilibrium state as violent relaxation ends, they do not stay unchanged forever and dissolve with the time. Star clusters lose their mass due to the internal evolution of stars and lose their stars due to two-body relaxation. Since star clusters orbit inside their host galaxy, they are the object of tidal stripping.

The two-body relaxation is the re-distribution of energy among all stars of a cluster through the exchange between pairs of stars due to distant gravi-

tational encounters. These cause to set up a Maxwellian velocity distribution at each point inside the cluster on the relaxation time-scale (Chandrasekhar, 1942; Spitzer, 1987)

$$t_r = \frac{0.065v_m^3}{n m^2 G^2 \ln \Lambda}, \quad (4)$$

where G is the gravitational constant, n the number density of stars, m and v_m are the mean mass and the average velocity of stars in the cluster, Λ is proportional to the number of stars N . Every relaxation time a constant fraction of stars acquire energies above the escape velocity, thus the lifetime of star clusters should last multiple relaxation times (Baumgardt, 2001; Chandrasekhar, 1942; Spitzer, 1987). If the star cluster is in virial equilibrium, then the half-mass relaxation time (i.e. measured within half-mass radius, r_h) is

$$t_{rh} = 0.138 \frac{\sqrt{N} r_h^3}{\sqrt{m} \sqrt{G} \ln \Lambda}. \quad (5)$$

Baumgardt (2001) performed direct N-body simulations of star clusters evolving in the tidal field of the host galaxy and showed that their lifetime scales with $t_{rh}^{3/4}$, instead of t_{rh} due to the backscattering of the potential escapers. Spurzem et al. (2005) obtained similar results using the anisotropic gaseous model based on the Fokker-Planck approximation for the number of stars less or equal $N \leq 50000$. It was clear that the star cluster lifetime depends on the number of stars, cluster density and strength of the tidal field (Baumgardt, 2001; Baumgardt, Hut, and Heggie, 2002; Baumgardt and Makino, 2003; Gieles and Baumgardt, 2008; Lamers, Baumgardt, and Gieles, 2010; Spurzem et al., 2005, among many others).

Boutloukos and Lamers (2003) found the mass dependent dissolution relation from the observation of star clusters in the solar neighborhood and nearby galaxies. Their work was supported by the following observational works: Bastian et al. (2012), Lamers, Gieles, and Portegies Zwart (2005), Lamers et al. (2005), and Silva-Villa et al. (2014).

Gieles et al. (2006) noted that the simulations of Baumgardt and Makino (2003) and the observational studies of cluster dissolution by Boutloukos and Lamers (2003) (improved later by Lamers et al., 2005) result in similar power-law relation between cluster dissolution time and initial mass, but the dissolution timescale obtained from the simulations are 5 times longer than that observed for the solar neighborhood. Therefore, an additional destructive process, encounters with giant molecular clouds, has been considered by Gieles et al. (2006) to solve this discrepancy.

Interestingly, Whitmore, Chandar, and Fall (2007), analyzing the star cluster population of the Antennae galaxy-merger, proposed that during the first gigayear of evolution, the dissolution time of star clusters is not only independent of their mass but also of their environment. The mass independent dissolution has been found also in other galaxies, which are not mergers as the Antennae galaxy (e.g. Chandar, Fall, and Whitmore, 2010; Chandar et al., 2014, 2016; Fall and Chandar, 2012; Fall, Chandar, and Whitmore, 2009; Linden et al., 2017). This led to the empirical ‘‘universal law’’ of cluster dissolution (also called Mass Independent Dissolution or MID, Whitmore, 2017).

Although their MID scenario was supported by several follow-up observational studies, no theoretical work was able to support it, until Ernst et al. (2015) showed, by means of N-body simulations, that MID is a potential channel of cluster dissolution during the first Gyr of cluster evolution.

Ernst et al. (2015) performed direct N-body simulations of star clusters with different Roche-volume filling factors, including clusters overfilling

their Roche lobe (i.e. overfilling clusters) and found that the latter can dissolve independently of their mass. They argued that clusters can overfill their Roche volume as a result of residual star-forming gas expulsion, i.e. when the gas is removed from the embedded cluster by stellar feedback, thereby weakening the gravitational potential. Therefore, the Jacobi radius of gas-free clusters shrinks and the stars which inhabit the cluster outskirts can now be located beyond the new Roche volume. In their simulations, star clusters are gas-free and are initially in virial equilibrium. However, if star cluster was previously gas-embedded, its gravitational potential should leave some imprints on the dynamics of gas-free cluster afterwards. That is, straight after gas expulsion, star clusters are not in virial equilibrium as suggested in Ernst et al. (2015). Instead, they should expand after gas expulsion if they were in virial equilibrium with the residual gas potential (Baumgardt and Kroupa, 2007; Brinkmann et al., 2017; Shukirgaliyev et al., 2017).

In 2015, the Legacy Extragalactic UV Survey (LEGUS) collaboration program started its work to investigate the connection between environmental conditions in galaxies and their cluster populations (Calzetti et al., 2015). Observing 50 local (closer than 12 Mpc) galaxies, the LEGUS program aims to discriminate among models of star cluster evolution, explore the impact of environment on star clusters and cluster evolution across the full range of galactic and interstellar medium properties.

Additionally, with the new observational era, started by the GAIA astrometric space telescope, and to be continued with the James Webb Space Telescope in close future, we are all in hope to find answers to our many questions about star formation and cluster evolution. However, as Louis Pasteur said: *“dans les champs de l’observation le hasard ne favorise que les esprits préparés”*, that is, *“in the fields of observation chance favors only the prepared minds”*. In order not to miss the opportunities provided by cornerstone observational facilities, we should therefore prepare ourselves by building good star cluster models. With such a wish in mind we have started to look at the problem of star cluster evolution/dissolution anew.

1.4 MOTIVATION

Our wish is to build a star cluster evolution model starting from its formation and ending with its dissolution in the tidal field of its host galaxy. The ideal case would be to build a grid of hydro-dynamical simulations considering the formation and evolution of star clusters starting from the collapse of turbulent molecular gas clouds. But hydro-dynamical simulations also have many assumptions, especially on assigning the initial velocities to individual newly formed stars (see Clarke, 2010). On top of that they are computationally expensive and limited in terms of the modeled cluster-forming gas mass (e.g. Bonnell et al., 2008, was limited to $4104M_{\odot}$). Bate (2009) reported that his large hydro-dynamic simulation of cluster formation from a $500M_{\odot}$ gas clump covering a 0.285 Myr time span took nearly 100'000 CPU hours running up to 16 processors (i.e. at least 8-9 months of calculations for one model). The situation has not changed significantly in the last decade.

There are hydro-dynamical simulations considering the evolution of entire cluster populations of galaxies (e.g. the MOSAICS model, Kruijssen et al., 2011; Pfeffer et al., 2018), which have to sacrifice spatial resolution and consider an entire cluster as one particle at best. They have many assumptions and depend on the models of cluster evolution applied in simulations (e.g. cluster mass-loss mechanisms). Therefore, these kind of simulations can miss some important details.

Star cluster long-term evolution can be easily studied with N-body simulations. For example Wang et al. (2016) performed their famous DRAGON

million-body simulation of globular clusters calculating the gravitational forces between stars by direct summation. There are many other N-body simulations which have been considered, but almost all of them start from virial equilibrium and are not necessarily connected to cluster-formation models.

In this work, instead of using hydro-dynamical simulations for cluster formation, we decided to use the semi-analytical local-density-driven cluster formation model of Parmentier and Pfalzner (2013) to describe the star-formation phase of our cluster life model. This give us the initial conditions for our subsequent direct N-body simulations and we then model the entire life of star clusters.

We use the local-density-driven cluster formation model, because:

1. it explains the star-formation relation between the surface densities of gas and young stellar objects observed in eight nearby molecular clouds by Gutermuth et al. (2011). That is, it provides us with the observed spatial distribution of gas and stars in embedded clusters without the need for long hydro-dynamical simulations.
2. it yields a volume density profile with a shallower slope for the star-forming residual gas than that of the stars, which is similar to the initial conditions considered by Adams (2000), but now physically justified. That is, our model clusters, with initial conditions derived from the Parmentier and Pfalzner (2013) cluster formation model, should survive instantaneous gas expulsion with lower SFEs.
3. the degree of spatial expansion is very high for surviving star clusters formed with a low SFE. They thus possibly end up as Roche volume overfilled clusters similar to those considered by Ernst et al. (2015). Therefore, it gives us the opportunity to explore the existence of mass independent dissolution of star clusters.

We think that our direct N-body simulations with more physically justified initial conditions than in other N-body works, give us a good opportunity to study the evolution of clusters starting almost from their formation, and up to stellar masses not achieved by hydro-dynamical simulations up to now.

Part II

METHODS

INITIAL CONDITIONS

2.1 STAR-FORMATION EFFICIENCY AND DENSITY PROFILES

A semi-analytical model of star cluster formation from centrally concentrated spherically symmetric gas clumps with a constant SFE per free-fall time, ϵ_{ff} , was developed by Parmentier and Pfalzner (2013). Because the free-fall time is shorter in the clump inner (denser) regions than in the clump outer (less dense) regions, the density profile of the formed star cluster is steeper than the density profiles of the initial and residual gas. The authors considered that the total density profile ρ_0 of the system remains constant.

The total density profile is the sum of the density profiles of the embedded cluster, ρ_* , and the residual gas, ρ_{gas} , at any time t after SF onset:

$$\rho_0(r) = \rho_{\text{gas}}(t, r) + \rho_*(t, r); \quad (6)$$

here r is the distance to the clump center. The density profile of the unprocessed gas at time t is described with Eq. (19) from Parmentier and Pfalzner (2013), which we reproduce here for the sake of clarity:

$$\rho_{\text{gas}}(t, r) = \left(\rho_0(r)^{-1/2} + \sqrt{\frac{8G}{3\pi}} \epsilon_{\text{ff}} t \right)^{-2}. \quad (7)$$

G is the gravitational constant and ϵ_{ff} is the SFE per free-fall time. The mass of the embedded cluster at time t is distributed according to Eq. (20) in Parmentier and Pfalzner (2013):

$$\rho_*(t, r) = \rho_0(r) - \left(\rho_0(r)^{-1/2} + \sqrt{\frac{8G}{3\pi}} \epsilon_{\text{ff}} t \right)^{-2}. \quad (8)$$

Our aim is to investigate the dynamical evolution of such star clusters after instantaneous gas expulsion and to estimate their survival likelihood. The instantaneous gas expulsion corresponds to the case when the timescale of the gas expulsion is significantly shorter than the dynamical timescale of the system. In terms of cluster survivability, it is the worst scenario we can envision. If a star cluster survives instantaneous gas expulsion, it is also able to survive a longer gas expulsion timescale.

We can adopt two different approaches to study this problem.

A. Either the starting point is a molecular clump, with a given density profile $\rho_0(r)$, and we obtain the density profile of the star cluster that formed after some SF time span based on Parmentier and Pfalzner (2013).

B. Alternatively, the starting point is an embedded cluster with a well-known profile (e.g., Plummer or King), and assuming an SF time span, we recover the initial gas density profile of the molecular clump out of which the cluster has formed.

In case (A) we start with the initial spherically symmetric gas clump that has a certain density profile $\rho_0(r)$ at time $t = 0$. Then we assume that a star cluster forms within a time interval $t = t_{\text{SF}}$ called SF duration with a constant SFE per free-fall time $\epsilon_{\text{ff}} = \text{const}$. Its density profile is then given by Eq. 8. Depending on how long the SF process lasts, star clusters with different SFE_{gl} are formed (see Fig 9. in Parmentier and Pfalzner (2013)). At time $t = t_{\text{SF}}$ (corresponding to a certain value of SFE_{gl}), we set the instantaneous gas expulsion, that is, we remove the unprocessed gas from the system. A

star cluster then becomes super-virial because it has lost part of the gravitational potential within which it was in virial equilibrium. This would define the initial conditions of our direct N-body simulations to study the effect of instantaneous gas expulsion.

Because model (A) depends on the SF duration, it results in star clusters with different global SFEs, masses, and spatial and velocity distributions, which makes it difficult to compare the results of the N-body simulations to each other. Additionally, generating the initial conditions of such models for N-body simulations is not trivial.

Our main point is to study the effect of instantaneous gas expulsion on a star cluster in dependence of its global SFE, therefore we can simplify the problem and consider clusters with a fixed stellar mass and spatial distribution while varying the global SFE at gas expulsion. This leads us to our case (B), on which we focus in this paper.

In case (B), we thus assume a fixed density profile and a fixed stellar mass for the embedded clusters at gas expulsion. Then the initial clumps that formed such clusters have therefore different total masses and spatial distributions depending on the assumed global SFE.

As we wish to study the response of a star cluster to gas expulsion as a function of the global SFE, we have to find the cluster velocity distribution for any given global SFE assuming it is in virial equilibrium with the gravitational potential of the residual gas. To find this distribution, which depends on the SF duration, we need to solve the inverse problem to that presented in case (A). That is, having the density distribution of a star cluster $\rho_*(r)$, we determine the density profile of the residual gas at gas expulsion $\rho_{\text{gas}}(r, t_{\text{SF}})$, and following from this, the density profile of the whole cluster-forming clump, $\rho_0(r, t_{\text{SF}})$. Then we modify the cluster velocity distribution function so as to account for its virial equilibrium with the gravitational potential of the residual gas.

The model developed by Parmentier and Pfalzner (2013) can be applied to any clump density profile. So we can choose a well-known density profile ρ_* for the embedded cluster and define the density profile of the residual gas corresponding to an SF duration t_{SF} by modifying Eqs. (6) and (7) and setting $t = t_{\text{SF}}$:

$$\rho_0(r, t_{\text{SF}}) = \rho_{\text{gas}}(r, t_{\text{SF}}) + \rho_*(r), \quad (9)$$

$$\rho_{\text{gas}}(r, t_{\text{SF}}) = \left((\rho_{\text{gas}}(r, t_{\text{SF}}) + \rho_*(r))^{-1/2} + \sqrt{\frac{8G}{3\pi}} \epsilon_{\text{ff}} t_{\text{SF}} \right)^{-2}. \quad (10)$$

In this equation, we note that the SF duration t_{SF} is given in units of Myr if densities $\rho_{(*, \text{gas})}$ are expressed in $M_{\odot} \text{ pc}^{-3}$ and the gravitational constant $G = 0.0045 \text{ pc}^3 M_{\odot}^{-1} \text{ Myr}^{-2}$. Introducing the parameter

$$k = \sqrt{\frac{8G}{3\pi}} \epsilon_{\text{ff}} t_{\text{SF}}, \quad (11)$$

which depends on the SFE per free-fall time ϵ_{ff} and SF duration t_{SF} , we can rewrite Eq. (10) as

$$k^4 \rho_{\text{gas}}^4 - (4k^2 - 2k^4 \rho_*) \rho_{\text{gas}}^3 - (6k^2 \rho_* - k^4 \rho_*^2) \rho_{\text{gas}}^2 - 2k^2 \rho_*^2 \rho_{\text{gas}} + \rho_*^2 = 0. \quad (12)$$

Solving this equation provides us with the residual gas density profile ρ_{gas} as a function of the stellar density profile ρ_* , SFE per free-fall time ϵ_{ff} , and SF duration t_{SF} . The stellar density profile, ρ_* , can be any centrally concentrated spherically symmetric density profile.

Equation (12) can be easily solved using software such as MATHEMATICA. Since the roots of this equation obtained with MATHEMATICA are very long, we made them more compact by introducing the following intermediate terms:

$$\alpha = k^4 \rho_\star^2; \quad (13)$$

$$K_0 = \sqrt[3]{\alpha^3 + 36\alpha^2 + 216\alpha + 24\alpha\sqrt{3(\alpha + 27)}}; \quad (14)$$

$$K_1 = \sqrt{\frac{\alpha^2 + \alpha(K_0 + 24) + K_0(K_0 + 12)}{12k^4K_0}}; \quad (15)$$

$$K_2 = \frac{(\alpha - K_0 + 24)(K_0 - \alpha)}{3k^4K_0}. \quad (16)$$

Then we can write the four roots of Eq. (12) as

$$\rho_{\text{gas}(1,2,3,4)} = \frac{1}{k^2} - \frac{\rho_\star}{2} \pm \frac{1}{2} \sqrt{K_2 + \frac{8}{k^6(\mp K_1)} + (\mp K_1)}. \quad (17)$$

The following relation is true for all real values of k and ρ_\star

$$K_2 < \frac{8}{k^6K_1}, \quad (18)$$

which gives complex numbers for two of the roots in case of $(-K_1)$. The other two roots are real, with one decreasing and the other increasing with ρ_\star . Since we consider a centrally concentrated clump, where the stellar density decreases with increasing radius, the gas density should follow the stellar density and decrease as well. Thus we choose the root that increases together with stellar density toward the clump center with the following expression:

$$\rho_{\text{gas}} = \frac{1}{k^2} - \frac{\rho_\star}{2} - \frac{1}{2} \sqrt{K_2 + \frac{8}{k^6K_1}} + K_1. \quad (19)$$

Parmentier and Pfallzner (2013) used a power-law density profile with a slope of -2 for their cluster-forming clumps. This yields a power-law density profile with a slope of about -3 for a star cluster. Such initial conditions are not ideal for N-body simulations because of their infinite stellar and gas masses. We need either to truncate these power-law profiles, or choose steeper profiles with finite masses. Thus we decide to use one of the well-known spatial density distribution functions for an embedded cluster, that is, the Plummer profile (Plummer, 1911),

$$\rho_\star(r) = \frac{3M_\star}{4\pi a_\star^3} \left(1 + \frac{r^2}{a_\star^2}\right)^{-5/2}, \quad (20)$$

where M_\star is the cluster total mass and a_\star is the Plummer radius, which corresponds to the projected half-mass radius of a star cluster.

Choosing a Plummer profile has many advantages, for instance, a finite mass for both gas and stars, and an analytical expression. It is also supported by almost all N-body codes, which makes it possible to compare the results of different works.

2.2 PHASE-SPACE DISTRIBUTION OF STARS AT THE TIME OF GAS EXPULSION

Since our aim is to perform N-body simulations, we adopted dimensionless N-body ([NB]) units. They are associated with the star cluster parameters, not with the cluster-forming clump parameters:

$$\begin{aligned} G' &= 1.0, & r' &= \frac{r}{a_*}, & m' &= \frac{m}{M_*}, \\ v' &= v \sqrt{\frac{a_*}{GM_*}}, & t' &= t \sqrt{\frac{GM_*}{a_*^3}}. \end{aligned} \quad (21)$$

The N-body units can be converted into physical units when G , a_* , M_* are assigned numerical values in their respective units. Here we note that our 'N-body' time unit depends on the cluster stellar mass M_* and Plummer radius a_* at the time of the instantaneous gas expulsion. It does not represent the dynamical timescale of the cluster (stars only) because the cluster is super-virial and its dynamics bears the imprint of the cluster-forming clump mass at the time of the gas expulsion. Neither does it represent the dynamical timescale of the clump (stars+gas) since the total mass and half-mass radius of the cluster-forming clump differ from the stellar mass and stellar half-mass radius because their density profiles have different shapes. We applied these N-body units for (i) to recover the density profile of the residual cluster-forming gas with Eq. 12, and (ii) to perform the subsequent N-body integration of the gas-free cluster after instantaneous gas expulsion.

To generate the initial conditions of our N-body simulations is not trivial because we need a star cluster in virial equilibrium with the gravitational potential of the residual gas, where the shapes of the gas and star distributions differ. In that respect, our case differs from most previous N-body simulations, as radial variations of the SFE increase the degree of complexity of the problem.

We used the `falcON` program `MKHALO` by McMillan and Dehnen (2007), which produces a spherically symmetric star cluster in virial equilibrium with an external potential as the initial conditions of direct N-body simulations. External potential means a gravitational potential produced by anything but the stars of the cluster. In this framework, the gravitational potential produced by the residual gas constitutes an external potential.

To use `MKHALO` for our purpose, we wrote an additional acceleration plugin `GASPOTENTIAL`, that is, an additional code, which takes into account the new external potential of our models. In this `GASPOTENTIAL` plugin we calculated the gravitational potential and the forces produced by the residual gas knowing its density profile. For this, we used Eq. (3.15') from Duboshin (1968):

$$\Phi_{\text{gas}}(r) = -\frac{4\pi G}{r} \int_0^r r'^2 \rho_{\text{gas}}(r') dr' - 4\pi G \int_r^{R_{\text{gas}}} r' \rho_{\text{gas}}(r') dr'; \quad (22)$$

$$\frac{d\Phi_{\text{gas}}(r)}{dr} = \frac{4\pi G}{r^2} \int_0^r r'^2 \rho_{\text{gas}}(r') dr'; \quad (23)$$

where ρ_{gas} was obtained by solving Eq. 12 (see Sect. 2.1), and R_{gas} is the adopted outer edge of the clump of residual gas. We used $R_{\text{gas}} = 32a_*$, which is the smallest radius possible to use in `MKHALO`. Because the gas density profile, ρ_{gas} , is not a simple function of r , the distance to the clump

center, Eqs. (22) and (23) were integrated numerically using the Simpson method.

In Eq. (22) we need to integrate over two intervals, $[0, r]$ and $[r, R_{\text{gas}}]$. So we could have high errors if we use equal number of bins for these two intervals, when $r \rightarrow 0$ and $r \rightarrow R_{\text{gas}}$. That is why I consider 3 cases with different binning for 2 intervals of integration as following:

- a) $0 \leq r < \frac{1}{4}R_{\text{gas}}, \quad N_{\text{bin}}^{\text{in}} = 2j + 1, \quad N_{\text{bin}}^{\text{out}} = 3(2j + 1);$
- b) $\frac{1}{4}R_{\text{gas}} \leq r < \frac{3}{4}R_{\text{gas}}, \quad N_{\text{bin}}^{\text{in}} = 2(2j + 1), \quad N_{\text{bin}}^{\text{out}} = 2(2j + 1);$
- c) $\frac{3}{4}R_{\text{gas}} \leq r < R_{\text{gas}}, \quad N_{\text{bin}}^{\text{in}} = 3(2j + 1), \quad N_{\text{bin}}^{\text{out}} = 2j + 1.$

Here j is some natural number, $N_{\text{bin}}^{\text{in}}$ and $N_{\text{bin}}^{\text{out}}$ are the numbers of bins for the numerical integrals $\int_0^r r^2 \rho_g(r) dr$ and $\int_r^{R_{\text{gas}}} r \rho_g(r) dr$, respectively. For our calculations $j = 512$ is sufficient and the relative errors are roughly of the order of 10^{-7} for the clump edge $R_{\text{gas}} = 32 a_*$ of the embedded cluster¹. The code listing of the GASPOTENTIAL acceleration plug-in can be found in Appendix A.2.

In the framework of this study, we adopted a fixed SFE per free-fall time of $\epsilon_{\text{ff}} = 0.05$. Then the only parameter we varied in our acceleration plugin to produce the initial conditions is the SF duration t_{SF} . To allow a comparison of our results with other works, however, it is better to use as a main parameter the SFE_{gl} than t_{SF} . To develop a grid of models with a given SFE_{gl} (0.05, 0.10, ...), we still need to infer the corresponding t_{SF} and add them to the models.

We defined the global SFE as the ratio between the stellar and total (stellar + gas) masses residing inside a chosen outer limit, R_{cl} . Because a Plummer model has no finite outer limit, we adopted $R_{\text{cl}} = 10a_*$, which is the radius inside which about 98 per cent of the stellar mass resides. Here we note that because of the slope difference between the density profiles of the embedded cluster and the residual (as well as total) gas, a larger outer limit would imply a lower global SFE, and vice versa. This is illustrated in Fig. 2, which presents the global SFE as a function of outer limit radius R_{cl} . There are SFE profiles of 5 model clusters with $\text{SFE}_{\text{gl}} = 0.05, 0.10, 0.15, 0.25,$ and 0.40 presented. Black dotted curve corresponds to the cluster stellar mass within the outer limit radius and corresponds to the right y-axis. The black vertical line corresponds to the outer limit adopted in this study, $R_{\text{cl}} = 10a_*$.

The relation between the SFE_{gl} and the corresponding SF duration t_{SF} calculated in N-body units is presented in Figure 3. In our study we concentrated on models with an $\text{SFE}_{\text{gl}} < 0.50$. The corresponding values of SFE_{gl} and t_{SF} for different models are presented in Table 1. Using these values, we produced the initial conditions of our simulations with MKHALO. Then, using the generated positions and velocities of the stars, we calculated the initial potential (Ω_*) and kinetic (T_*) energies of our model clusters at the moment of instantaneous gas expulsion, as well as their initial virial ratios and eSFEs, using Eqs. (3) and (2). The corresponding values are also presented in Table 1.

¹ The code ‘MKHALO’ does not generate any particle at a distance larger than $r = 32a_*$. Therefore $R_{\text{gas}} = 32a_*$ is chosen to be the clump edge in ‘GASPOTENTIAL’ acceleration plug-in too.

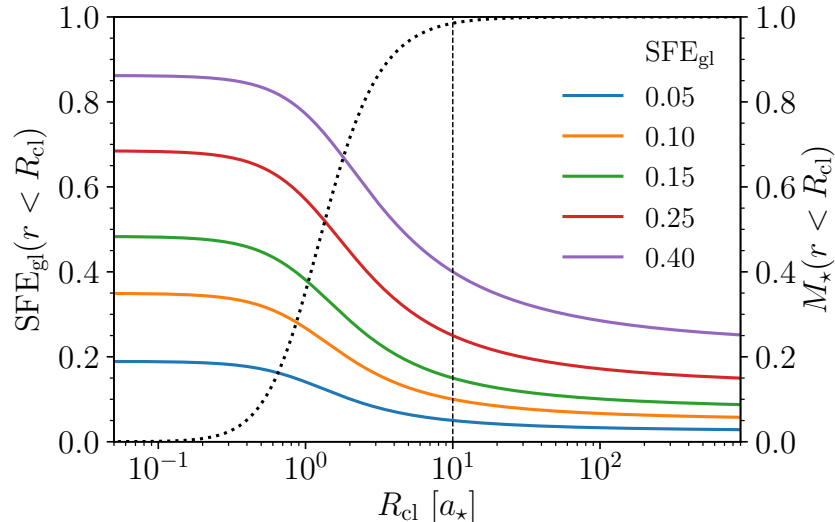


Figure 2: SFE profiles of 5 model clusters with $\text{SFE}_{\text{gl}} = 0.05, 0.10, 0.15, 0.25,$ and 0.40 as a function of outer limit radius R_{cl} given in units of Plummer radius a_* . The black vertical dashed line corresponds to the outer limit adopted in this study $R_{\text{cl}} = 10a_*$. The black dotted curve shows the stellar mass of the cluster within the outer limit of R_{cl} .

We find that in our models the effective and global SFEs are different, unlike the models that used the same density profile for both the stars and gas (see Boily and Kroupa (2003a), Goodwin and Bastian (2006), Goodwin (2009)). Varying the outer edge R_{cl} of the cluster, we infer that these eSFEs are almost the same as the global SFEs measured inside $1.5a_*$, that is, similar within 2-3 percent to the global SFEs measured inside a cluster half-mass radius. The latter also measures the LSF as defined by Smith et al. (2011). Goodwin (2009) noted that star clusters with an initial virial ratio lower than 1.5 are able to survive the instantaneous gas expulsion (in the case of Plummer profiles for both stars and gas), which corresponds to an effective SFE of 33 percent. Taking this into account, we can expect the minimum SFE needed to form a bound cluster to be $\text{SFE}_{\text{gl}} = 0.15$, as it corresponds to $Q_* \approx 1.5$ for our models (see Table 1). This is indeed what we show in Chapter 3.

The density profiles of the embedded cluster, its residual gas before instantaneous gas expulsion, and the initial clump gas for different global SFEs are shown in Figure 4. The models were scaled to physical units assuming a star cluster mass of $M_* = 3000 M_\odot$ and a 3D half-mass radius of $r_h = 1$ pc. The density units are given in $M_\odot \text{pc}^3$ (right y-axis) and molecules per cm^3 (left y-axis). Gas densities on this scale vary within the observed range of dense clumps ($\leq 10^5 \text{cm}^{-3}$). The SF durations t_{SF} for these three models are 0.39 Myr, 2.21 Myr, and 12.77 Myr. As we see, some of our models are inconsistent with observations in the sense that the inferred SF duration is longer than what is observed.

For our high-resolution direct N-body simulations we have chosen the $\phi\text{GRAPE-GPU}$ code developed by Berczik et al. (2011, 2013). As a check of the stability of the initial conditions generated by the code MKHALO , we added our newly created external potential to the $\phi\text{GRAPE-GPU}$ code and tested the dynamics of the embedded cluster within the residual gas potential. We ran a few simulations with external potentials corresponding to different

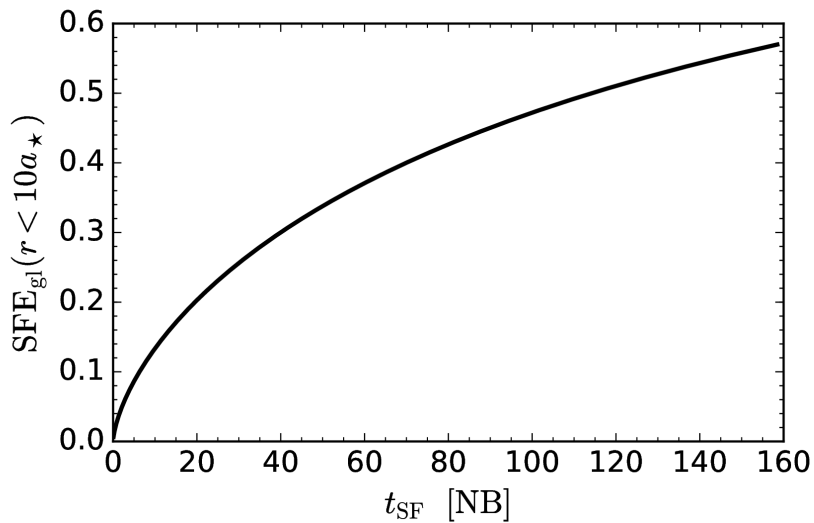


Figure 3: Relation between the SF duration (t_{SF}) (given in N-body units according to Eq.21) and the global SFE (SFE_{gl}), measured inside $R_{\text{cl}} = 10a_{\star}$. The lowest value of the global SFE here in this plot is $\text{SFE}_{\text{gl}} = 0.007$, which corresponds to an SF duration $t_{\text{SF}} = 0.01$ [NB].

t_{SF} . The test runs were performed for isolated clusters with $N = 10\text{k}$ single-mass particles over a time interval of up to 1000 N-BODY time units, which is slightly shorter than three relaxation times of the same cluster in virial equilibrium without external potential. We checked the evolution of the Lagrangian radii and cumulative mass profiles for different SFEs varying the star-formation duration values lt_{SF} from 0.05 to 100 NBU, that corresponds to SFE_{gl} from 0.02 to 0.47. These exercises showed that our newly generated initial conditions are indeed in virial equilibrium with the external gas potential (see Fig. 5).

Table 1: Global SFEs (SFE_{gl}) and their corresponding SF durations (t_{SF}) in N-body units (see Eq. 21), the virial ratios Q_* of star clusters, and eSFEs immediately after gas expulsion.

SFE_{gl}	t_{SF} [NB]	$Q_* = T_*/ \Omega_* $	eSFE = $1/2Q_*$
0.05	2.14	4.34	0.12
0.10	6.30	2.26	0.22
0.13	9.58	1.77	0.28
0.15	12.09	1.55	0.32
0.20	19.53	1.21	0.41
0.25	28.74	1.00	0.50
0.30	39.96	0.87	0.58
0.35	53.53	0.77	0.65
0.40	69.94	0.71	0.70
0.45	89.85	0.66	0.76
0.50	114.22	0.62	0.81

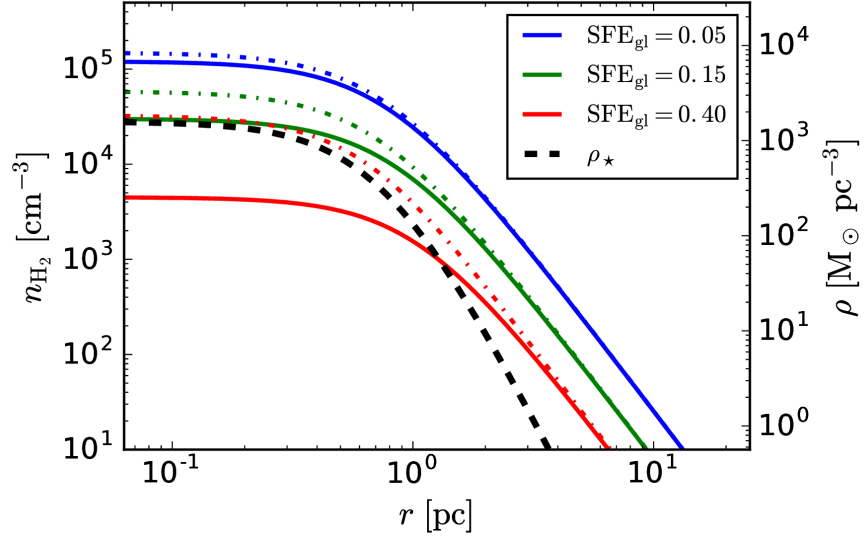


Figure 4: Density profiles of the star cluster (black dashed line), of the residual (solid lines), and initial (dash-dotted lines) gas for different SFE_{gl} in scaled physical units. A total stellar mass $M_* = 3000 M_\odot$ and a 3D half-mass radius $r_h = 1$ pc are assumed. Note that the stellar density profile is a Plummer profile.

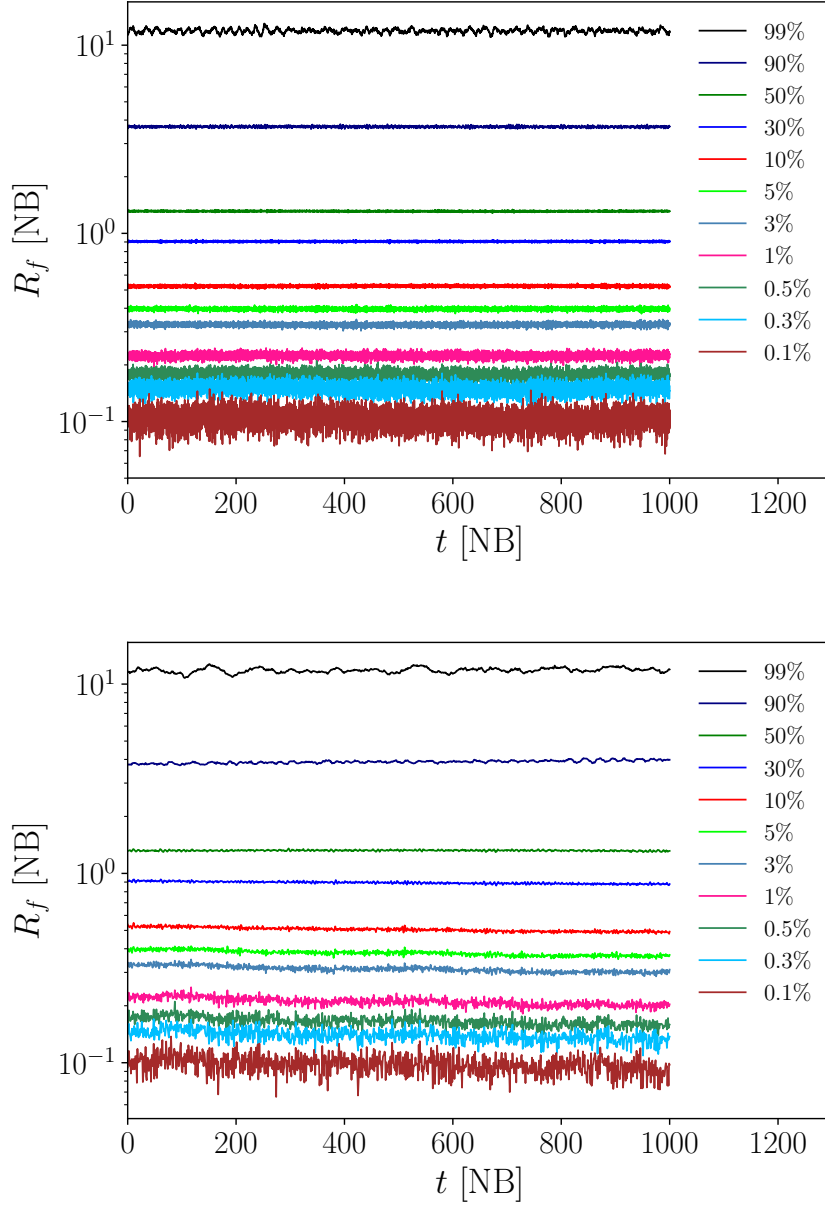


Figure 5: Lagrange radii evolution for simulations with an external potential for two different values of $t_{SF} = 0.5$ NBU (top panel) and 100 NBU (bottom panel), which correspond to $SFE_{gl} = 0.02$ and 0.47 respectively. The simulations are quite stable even with very low SFE, which shows that our models are initially in equilibrium with the external potential of the residual gas clump.

Part III

RESULTS

IMPACT OF SFE-PROFILE ON THE EVOLUTION OF OPEN CLUSTERS

The results presented in this chapter are published in the peer-reviewed paper Shukirgaliyev, B., G. Parmentier, P. Berczik, and A. Just (2017). “Impact of a star formation efficiency profile on the evolution of open clusters.” In: *A&A* 605, A119. B. Shukirgaliyev performed all N-body simulations, analyzed their outputs and wrote most of the text. All authors contributed ideas, comments and suggestions throughout the realization of this study and its preparation as a peer-reviewed paper.

3.1 SETTING UP THE SIMULATIONS

We performed two types of N-body simulations. First, we simulated isolated single-mass clusters without stellar evolution to observe the pure dynamical effect of an instantaneous gas expulsion. We ran these simulations with $N = 10^4$ particles and covered global SFEs ranging from 5 to 50 percent.

Second, we studied a more realistic scenario of violent relaxation by considering star clusters consisting of multi-mass stars that evolve in a Galactic tidal field. We refer to these two sets of simulations as ‘isolated’ and ‘non-isolated’ models.

For the stellar initial mass function (IMF) of our non-isolated models we adopted the IMF of Kroupa (2001) with the lower and upper mass limits of $M_{\text{low}} = 0.08 M_{\odot}$ and $M_{\text{up}} = 100 M_{\odot}$, respectively.

3.1.1 The tidal field of the Galaxy

We consider star clusters on circular orbits in the Galactic disk plane. For the Galactic tidal field we use an axisymmetric three-component Plummer-Kuzmin model (Miyamoto and Nagai, 1975) with the parameters as given in Just et al. (2009). For the sake of clarity we provide here the Equation (32) of Just et al. (2009) describing the Galactic tidal field components

$$\Phi(R, z) = -\frac{GM}{\sqrt{R^2 + \left(a + \sqrt{b^2 + z^2}\right)^2}}, \quad (24)$$

where G is the gravitational potential, M is the mass of the component, and a and b represent the flattening and the core radius of the component. Their numerical values are given in Table 2. The rotation curve obtained from the Galactic potential model is presented in Fig. 23.

Table 2: The numerical values of the Galaxy component parameters from Eq. 24.

Galaxy component	$M [M_{\odot}]$	a [kpc]	b [kpc]
Bulge	1.4×10^{10}	0.0	0.3
Disk	9.0×10^{10}	3.3	0.3
Halo	7.0×10^{11}	0.0	25.0

We also use Equation (13) from Just et al. (2009) to calculate the Jacobi radius:

$$R_J = \left(\frac{GM_J}{(4 - \beta^2)\Omega^2} \right)^{1/3}, \quad (25)$$

where M_J is the Jacobi (bound) mass of the cluster (which is the stellar mass enclosed within one Jacobi radius), $\beta = 1.37$ is the normalized epicyclic frequency and $\Omega = V_{\text{orb}}/R_{\text{orb}}$ is the angular speed of a star cluster moving with an orbital speed V_{orb} on a circular orbit at a Galactocentric distance R_{orb} . This was added to the $\phi_{\text{GRAPE-GPU}}$ code by Just et al. (2009), and we used it keeping their parameters.

We considered that our clusters move on a circular orbit in the plane of the Galactic disk, at a distance of $R_{\text{orb}} = 8$ kpc from the Galactic center.

3.1.2 From N-body to physical units

We normalized our N-BODY units to the real physical units in order to assign the correct timescale to the stellar evolution routines (SSE; Hurley, Pols, and Tout (2000)) implemented in the $\phi_{\text{GRAPE-GPU}}$ code. This means that we assigned certain values to the cluster mass (M_\star) and the initial Plummer radius (a_\star).

Our simulations encompass five different initial cluster stellar masses: $M_\star = 3000, 6000, 10000, 15000, \text{ and } 30000 M_\odot$. Then knowing the distance of the cluster to the Galactic center, we can calculate the cluster tidal (Jacobi) radius R_J for a given mass M_\star using Eq (13) from Just et al. (2009), which we reproduce here for the sake of clarity:

$$R_J = \left(\frac{GM_\star}{(4 - \beta^2)\Omega^2} \right)^{1/3}. \quad (26)$$

Here $\beta = 1.37$ is the normalized epicyclic frequency and $\Omega = V_0/R_{\text{orb}}$ is the angular speed of a star cluster on a circular orbit at a distance R_{orb} from the Galactic center. For $R_{\text{orb}} = 8000$ pc, the orbital speed recovered from the rotation curve of the Galaxy model provided in Just et al. (2009) is $V_0 = 234.24 \text{ km s}^{-1}$.

To make the models comparable with each other, we fixed the half-mass radius to the tidal radius ratio. We calculated it for a cluster mass $M_\star = 3000M_\odot$ with a half-mass radius of $r_h = 1$ pc. This means that we considered clusters with different stellar masses, but the same mean stellar volume densities. The tidal radius of a cluster with $M_\star = 3000M_\odot$ and $r_h = 1$ pc is $R_J = 19.2$ pc, and therefore

$$\frac{r_h}{R_J} \approx 0.052. \quad (27)$$

Thus we normalized the N-BODY length unit into physical units of pc knowing that in a Plummer model $r_h \approx 1.3a_\star$,

$$r_{\text{norm}} = a_\star \approx 0.77r_h \approx 0.04R_J, \quad (28)$$

where the tidal radius is calculated using Eq. (26). For the models with an initial stellar mass $M_\star = 3000 M_\odot$, for instance, the normalized length is equal to $r_{\text{norm}} = 0.77$ pc.

With our definition of the outer limit R_{cl} of our cluster-forming clumps (see Sect. 2.2), star clusters initially fill their tidal radius up to 40 percent. This means that the total radius of a star cluster is initially smaller than its tidal radius: $R_{\text{cl}} = 10a_\star = 0.4R_J$. The properties of a star cluster as a function of its stellar mass are presented in Table 3.

Table 3: Set of models corresponding to different initial stellar masses.

M_\star [M_\odot]	N_\star	R_J [pc]	r_h [pc]	$R_{cl} = 10a_\star$ [pc]
3000	5227	19.211	1.00	7.664
6000	10455	24.204	1.26	9.656
10000	17425	28.697	1.49	11.449
15000	26138	32.850	1.71	13.310
30000	52277	41.389	2.15	16.512

The scale factor of time units, as shown in Eq. 21, can be found as

$$t_{\text{norm}} = \sqrt{\frac{1_{\text{norm}}^3}{GM_\star}} \approx 0.18 \text{ Myr} \quad (29)$$

when $r_h/R_J = 0.052$. Given our assumption of a fixed ratio of the half-mass to tidal radius (see Eqs. 27 and 28), $r_{\text{norm}} \propto R_J \propto (GM_\star)^{1/3}$, t_{norm} is the same for all models as well as the mean stellar volume densities.

The corresponding values of SF duration and total (stars + gas) volume densities averaged within the initial stellar 3D half-mass radius are provided in Table 4. This table shows that the models are consistent with the observations in terms of SF duration and clump mean densities. It is thought that star cluster formation takes between one half and roughly 5 Myr in the solar neighborhood. We therefore consider the models in these limits to make our simulations as consistent with reality as possible. This limits the SF duration of our models between 2.7 and 27 N-BODY time units, which corresponds to 0.5 and 5 Myr for our chosen scale factor of r_h/R_J . Consequently, this also limits us in the range of achievable SFE_{gl} . According to these limits, we decided to calculate models with SFE_{gl} between 10 percent and 25 percent for $\epsilon_{\text{ff}} = 0.05$, which corresponds to an SF duration t_{SF} between 1.15 and 5.25 Myr for all initial cluster masses M_\star . To cover still higher SFEs, we ran two additional models with global SFEs of 30 and 35 percent for $M_\star = 6000M_\odot$. To make these runs consistent with the observations in terms of SF duration, we built on the following feature of Eq. (12): because the parameter k in Eq. (12) is proportional to $\epsilon_{\text{ff}}t_{\text{SF}}$, our results stand for any model where the product $\epsilon_{\text{ff}}t_{\text{SF}}$ is conserved (e.g., a twice higher SFE per free-fall time with a twice shorter SF duration). In our two additional runs the SF durations can therefore be considered as $t_{\text{SF}} = 3.64$ Myr and 4.88 Myr, respectively, if $\epsilon_{\text{ff}} = 0.1$. For comparison, additional models with the same spatial distribution of stars initially in virial equilibrium within a Galactic tidal field, but without any residual star-forming gas, (i.e., equivalent to $\text{SFE}_{\text{gl}} = 1.0$), were run for $M_\star = 3000, 6000, \text{ and } 10000 M_\odot$.

The mean (total and stellar) volume densities of models are also consistent with observations of star-forming molecular clumps, where an SF density threshold has been suggested ($\geq 10^4 \text{ cm}^{-3}$ in Lada, Lombardi, and Alves (2010) and $> 5 \times 10^3 \text{ cm}^{-3}$ in Kainulainen, Federrath, and Henning (2014)) and with stellar densities in embedded clusters, which vary from 100-200 to $1\text{-}2 \times 10^4 \text{ stars pc}^{-3}$ (Hillenbrand and Carpenter, 2000; Lada et al., 1991).

Based on these simulations, we now study the evolution of the bound fraction of star clusters. We present the results of isolated models scaled to physical units such that $M_\star = 6000 M_\odot$ and $r_h = 1.26 \text{ pc}$ (see Table 3) to compare them with $M_\star = 6000 M_\odot$ non-isolated models, which consist of 10455 stars.

Table 4: Global SFEs (SFE_{gl}) and corresponding values of the SF duration (t_{SF}) in N-body units (Eq. 21) and in units of Myr for the adopted normalization parameters (using Eq. 29). The rows within the box highlight the non-isolated models selected for our simulations. We also show here the mean volume density of the clump (star + gas) inside the half-mass radius. Because we kept the stellar masses constant while varying the global SFE, we varied the fraction of unprocessed gas. When the global SFE increases, the mass of the residual gas decreases (keeping stellar mass constant), and as a consequence, the total volume density decreases as well.

SFE_{gl}	t_{SF} [NB]	t_{SF} [Myr]	$\bar{\rho}_{tot}(< r_h)$ [$M_{\odot} \text{ pc}^{-3}$]	$\bar{n}_{H_2,tot}(< r_h)$ [cm^{-3}]
0.05	2.14	0.39		
0.10	6.30	1.15	1490.73	26405
0.13	9.58	1.75	1177.02	20848
0.15	12.09	2.21	1037.99	18386
0.20	19.53	3.56	813.52	14410
0.25	28.74	5.25	680.92	12061
0.30	39.96	7.29	594.24	10526
0.35	53.53	9.77	533.91	9457
0.40	69.94	12.77		
0.45	89.85	16.40		
0.50	114.22	20.85		

3.2 CLUSTER-BOUND FRACTION EVOLUTION

3.2.1 Bound fraction of isolated models

In the classical way, the bound fraction of isolated clusters in virial equilibrium is defined as the fraction of stars whose total energy (i.e., kinetic + potential) is negative, that is, the potential energy dominates the kinetic energy. The bound fraction defined in the “classical” way shown by solid lines in Fig. 6, which presents the bound fraction evolution of our isolated model clusters with different global SFE corresponding to different colors (see the key).

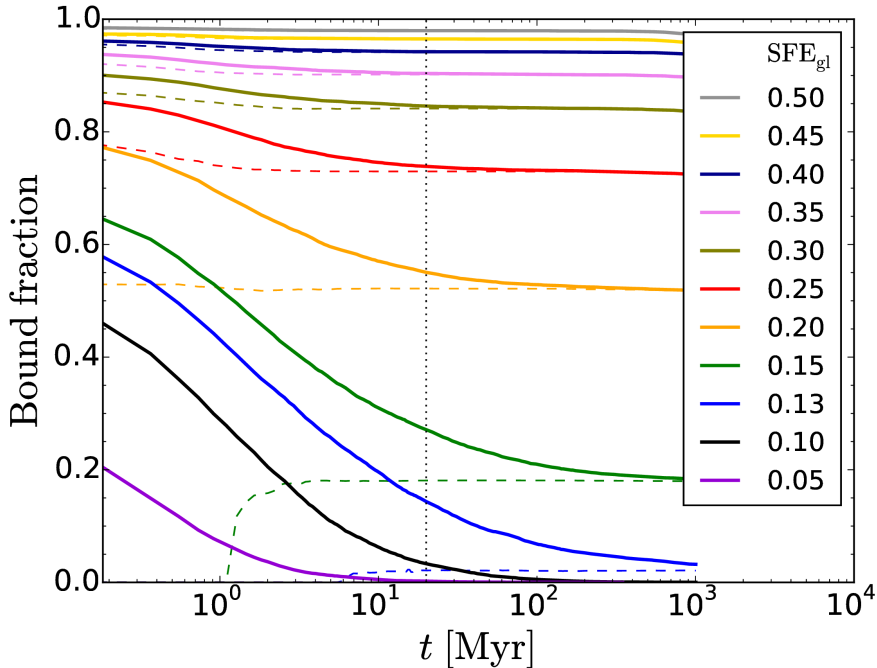


Figure 6: Time evolution of the bound fraction F_b of isolated models ($N = 10^4$) as defined by two methods: defined by the fraction of stars with a negative total energy (solid lines), and defined by recalculating the total energy of stars in an iterative process (see text for details; dashed lines). The vertical dotted line corresponds to $t = 20$ Myr when we scale the isolated models with the same scale factor as for a non-isolated model with $M_\star = 6000 M_\odot$, which also has $N \approx 10^4$.

Our model isolated clusters become supervirial and start to expand quickly after instantaneous gas expulsion, however. Thus it is not trivial to distinguish between bound and unbound stars in such systems during their expansion. The unbound stars can be located anywhere inside a such cluster and make a significant contribution to its gravitational potential depending on global SFE. Thus the bound fraction remains overestimated until bound and unbound stars are clearly spatially separated from each other. For instance, model clusters with global SFEs of 0.05 and 0.10 do not survive the instantaneous gas expulsion. In Fig. 6, however, they retain a significant bound fraction for several Myr. For clusters with global SFEs of 0.13 and 0.15, we need to wait for a long time to reach the final bound fraction, that is, for the unbound stars to have evacuated the cluster region and to no longer contribute to the cluster gravitational potential. This process can take quite a long time in isolated systems, especially if the final bound fraction

is small. For instance, the cluster with $\text{SFE}_{\text{gl}} = 0.15$ needs 1 Gyr to approach the final bound fraction if this is defined in the “classical” way.

These reasons motivated us to develop another technique to define the final bound fraction early on in the evolution of clusters. We recalculated the total energies of stars, removing the unbound stars (i.e., stars whose total energy is positive) from the cluster even if they were located in the center of the cluster. We iterated until no unbound star remained in the cluster. Doing so, we excluded the contribution of unbound stars to the cluster potential. The final bound fraction of our isolated models is defined as the final fraction of stars that remained bound to the cluster - if any - at the end of the iterations. We emphasize that removing the unbound stars does not mean that we removed them from the simulations, but that we removed them from our selected sample at each snapshot for the purpose of our analysis only. For each snapshot in time, we always started the iterative process with the total number of stars.

Figure 7 presents an example of the evolution of the bound fraction and Lagrange radii of an isolated cluster with a global SFE of 15 percent. As

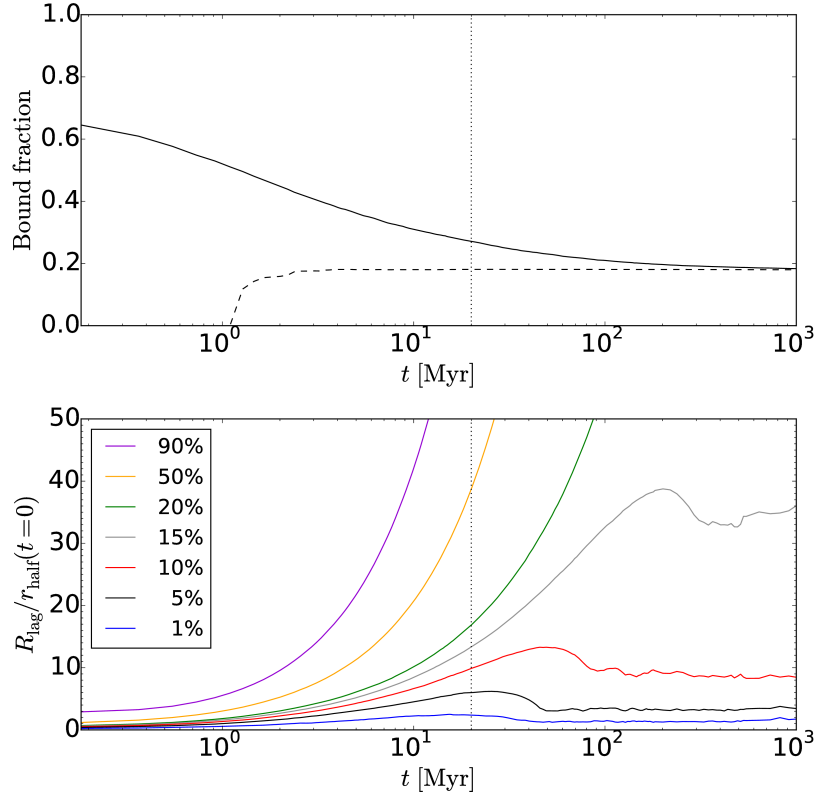


Figure 7: Top panel: bound and final bound fraction evolution of an isolated cluster with $\text{SFE}_{\text{gl}} = 0.15$ (solid and dashed lines, respectively). Bottom panel: Lagrange radius evolution of the same model. Lagrange radii are given in units of the initial stellar half-mass radius.

we see when comparing the top and bottom panels, the bound fraction decreases during the cluster expansion and reaches its final value when its bound stars have collapsed back and form a bound cluster. With the new technique, however, we can predict the final bound fraction already after 2 Myr, when the cluster is still in the expansion phase. Figure 6 and the top panel of Fig. 7 show that the instantaneous bound fraction converges toward

the final bound fraction determined with our technique by the end of the simulations. This shows that with our calculation method we can estimate the final bound fraction even before the inner part of the cluster starts to collapse back and return to virial equilibrium. We caution, however, that with this method we underestimate the final bound fraction of a cluster with a low global SFE during their early evolution after instantaneous gas expulsion. This is caused by removing all unbound stars, including the centrally concentrated ones, which contribute the most to the gravitational field of the cluster (see Fig. 7). This is the reason for the unusual behavior of the final bound fractions of isolated clusters with a global SFE of 0.13 and 0.15, which is 0 at $t \leq 1$ Myr, and why they rise at an early time in the evolution instead of decreasing.

3.2.2 Bound fraction of non-isolated models

For the non-isolated clusters, that is, those evolving within a Galactic tidal field, the bound fraction is defined as the stellar mass residing inside the instantaneous tidal radius normalized to the initial stellar mass,

$$F_{\text{bound}} = \frac{M_{\star}(r < R_J)}{M_{\star}}. \quad (30)$$

In the top panel of Fig. 8 we present the time evolution of the bound fractions of our non-isolated (solid lines) and isolated (dashed lines) models. We note that for the isolated clusters we present the final bound fraction defined with the technique described above, and not the fraction of stars with negative total energy. This clearly provides a method for determining the bound mass very early. For our non-isolated models, we also show the imprint of stellar-evolution mass loss as the gray lines. The model clusters with $\text{SFE}_{\text{gl}} = 1.0$, that is, those that are initially in virial equilibrium without any residual star-forming gas, are depicted as sky-blue lines. To better visualize both the very fast evolution shortly after gas expulsion and the cluster long-term evolution, the scale of the x-axis (time) is logarithmic. The plateau at the very beginning of the bound mass evolution results from our definition of the bound mass fraction, which does not account for the high-velocity unbound stars within the tidal radius. Because the cluster initial size is smaller than its tidal radius ($r_{\text{h}}/R_J = 0.052$), almost all stars reside within the tidal radius during the first few Myr of evolution even when the cluster starts to expand. The bound mass fraction starts to decrease as the escaping stars reach the tidal radius and become unbound by our definition.

From the bound fraction evolution of our non-isolated model clusters we can identify two regimes of mass loss (the solid lines in the top panel of Fig. 8), in addition to the mass loss driven by stellar evolution. During the first 20 Myr after gas expulsion, clusters intensively lose their mass (top panel of Fig. 8: the solid lines on the left-hand side of the vertical dotted line). During this time span, the cluster evolution is dominated by the consequences of gas expulsion, and their response is mostly determined by the cluster initial virial ratio. More or less flat plateaus can be seen in between two identified mass-loss regimes around 20 Myr after gas expulsion. This means that the surviving part of the cluster is not expanding anymore.

The bound fraction then decreases more slowly with time. It is now mostly affected by stellar evolution and the tidal field of the host galaxy (top panel of Fig. 8: the solid lines on the right-hand side of the vertical dotted line).

The bottom panel of Fig. 8 presents results for the non-isolated models alone for the global SFEs and initial cluster stellar masses quoted in the key. The color-coding is identical to the coding used in the top panel. We find

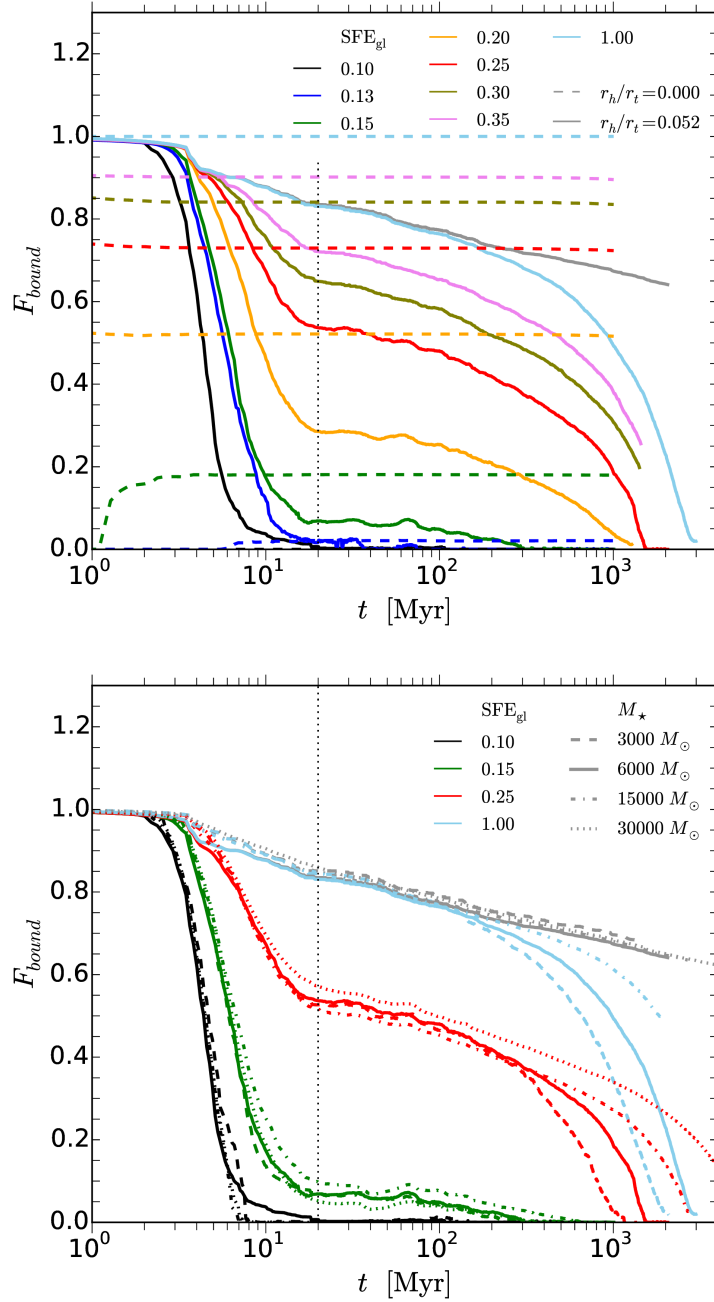


Figure 8: Evolution of the bound fraction of clusters obtained in our simulations. Different colors correspond to different global SFEs (see the key). The gray lines show the impact of mass loss caused by stellar evolution alone. The vertical dotted line corresponds to $t = 20$ Myr. Top panel: comparison of the bound fraction evolution of isolated (dashed lines) and non-isolated (solid lines) models for $M_{\star} = 6000 M_{\odot}$ with $N \approx 10^4$ stars. Note that the isolated models are the single-mass models without stellar evolution and scaled to the same physical units as the non-isolated models (i.e., $M_{\star} = 6000 M_{\odot}$ and $r_h = 1.26$ pc). Bottom panel: bound fraction (instantaneous tidal mass as a fraction of initial stellar mass) evolution for non-isolated models with different initial stellar masses (see the key for the line-coding).

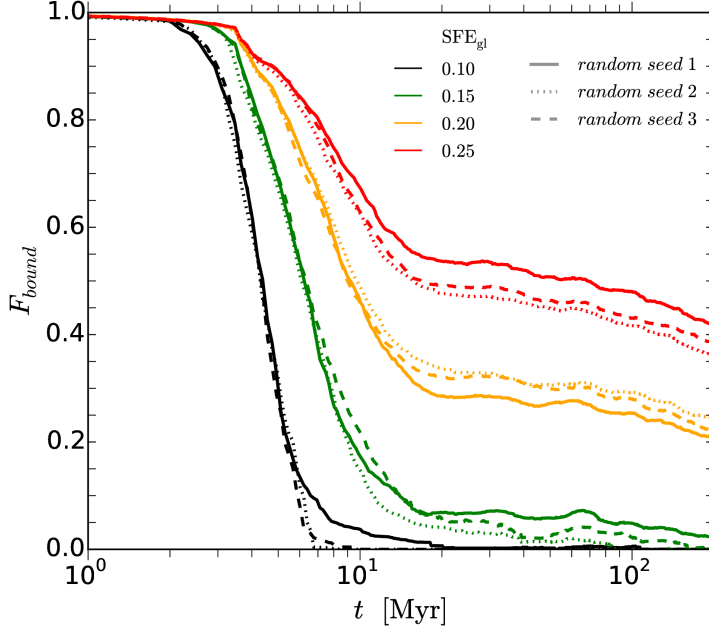


Figure 9: Different random realizations (see line types in the key) of the model clusters with $M_{\star} = 6000 M_{\odot}$ ($N = 10455$ stars) for $r_h/R_J = 0.052$.

that the models with identical global SFE show similar evolutionary tracks within the first 20 Myr (i.e., during the violent relaxation) independently of their initial stellar mass (bottom panel of Fig. 8). In particular, the models with a low global SFE dissolve on similar timescales independently of the initial star cluster mass, M_{\star} (see the black curves). Here we recall that the ratio r_h/R_J is kept constant for now. The model with a global SFE of 13 percent and $M_{\star} = 6000 M_{\odot}$ does survive as a bound cluster, although with a very small bound fraction, around 2 percent (the blue lines in the top panel of Fig. 8). All other stellar mass models with a global SFE of 13 percent dissolve, however, except for the $M_{\star} = 30000 M_{\odot}$ model, which barely survives with a 0.17 percent bound fraction, which corresponds to a bound mass of about $52 M_{\odot}$. Therefore we adopt the models with $\text{SFE}_{\text{gl}} = 0.13$ as the limit between survival and dissolution following cluster gas expulsion for our adopted tidal field impact $r_h/R_J = 0.052$. Cluster models with a global SFE of 0.15 and higher can survive instantaneous gas expulsion, as expected from their initial virial ratios (see Table 1). We note that $\text{SFE}_{\text{gl}} = 0.13$ is about 2.5 times lower than the SFE threshold for cluster survival when (i) the density profiles of the stars and residual gas have the same shape, (ii) gas expulsion is instantaneous, and (iii) the tidal field impact is negligible.

We performed a few simulations for a given parameter set but different random seeds to explore the bound fraction variations that are due to random realizations. Figure 9 shows that the bound mass fraction at $t = 20$ Myr displays a range of variations of about 10 percent for a cluster with $N = 10455$ stars (i.e., $M_{\star} = 6000 M_{\odot}$ cluster). For a cluster with a higher number of stars ($N = 26138$, $M_{\star} = 15000 M_{\odot}$), the range of bound mass fraction variations is about 6 percent. The duration of cluster mass-loss in response to gas expulsion remains shorter than 20 Myr for different random realizations.

After violent relaxation, the cluster life-expectancy depends on its stellar mass, as expected (red lines in the bottom panel of Fig. 8). A higher stellar mass implies a higher probability to survive a longer time (but see Ernst

et al. (2015)). The models corresponding to the high global SFEs in this set of simulations show long-term evolutionary patterns similar to the pure Plummer models (i.e., initially in virial equilibrium without any external potential).

This study shows us that the mass loss of the cluster in response to gas expulsion is completed within 20 Myr, independently of its initial stellar mass and global SFE, and that its dynamical evolution is mostly affected by the tidal field of the host galaxy thereafter (Fig. 8). Since we focus on the cluster bound mass evolution, we consider the violent relaxation as the time span when the cluster loses its mass intensively in response to an instantaneous gas expulsion. We therefore used $t = 20$ Myr to measure the final bound fraction of clusters. We note, however, that the outer shells of surviving clusters need a longer time-span to return to virial equilibrium, as shown by Fig. 10 (see below; see also Brinkmann et al. (2017)). We note therefore that the violent relaxation duration, as defined here, does not strictly equate with the cluster revirialization time.

An example of the Lagrange radius R_f evolution of a non-isolated cluster with $SFE_{gl} = 0.20$ and $M_\star = 6000M_\odot$ is presented in Fig. 10. The Lagrange

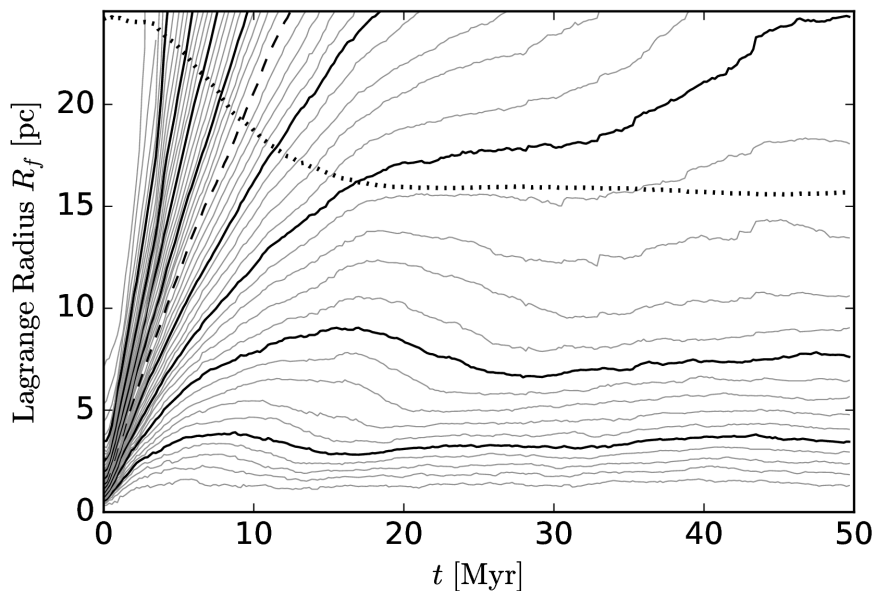


Figure 10: Evolution of a non-isolated cluster of the solar neighborhood with $SFE_{gl} = 0.20$, $M_\star = 6000 M_\odot$ and $r_h/R_J = 0.052$ over 50 Myr after gas expulsion. We show 49 Lagrange radii, ranging from 2 percent to 98 percent in intervals of 2 percent (solid and dashed lines). The instantaneous tidal radius R_J of the cluster is shown as the dotted line. Thick solid lines correspond to every 10 percent of the Lagrange radius, and the dashed line corresponds to 50 percent of the Lagrange radius.

radii are defined based on the fraction of initial stellar mass, not on the number fraction of stars. The dotted line in this figure represents the instantaneous tidal radius. This figure shows that the inner parts of a cluster recede, form a bound cluster, and return to virial equilibrium within 20-30 Myr after gas expulsion. The inner shells of a cluster revirialize faster than the outer shells, as also found in Brinkmann et al. (2017), for example. The cluster tidal radius stays roughly constant after 20 Myr.

Table 5: Scaling factors to the physical time and duration of 20 Myr in N-body units corresponding to different ratios of the cluster half-mass to tidal radius.

r_h/R_J	t_{norm} [Myr]	20 Myr [NB]
0.025	0.0608	329
0.052	0.1826	110
0.07	0.2848	70
0.10	0.4863	41

3.3 INFLUENCE OF THE CLUSTER INITIAL STELLAR DENSITY

To quantify the effect of the tidal field impact, three additional sets of simulations were performed for cluster masses $M_\star = 6000 M_\odot$ and $15000 M_\odot$: one with a weaker tidal field impact ($r_h/R_J = 0.025$), and two with stronger tidal field impact corresponding to $r_h/R_J = 0.07$ and 0.10 . That is, we varied the half-mass radius of our model clusters, keeping them in the solar neighborhood (i.e., keeping the same tidal radius for a given stellar mass). Because we varied the initial density of the cluster, we varied the normalization factor of time units as shown in Table 5. For denser clusters (smaller r_h/R_J), a given physical time-span represents a higher number of N-body time units.

We present the bound mass fraction evolution of $M_\star = 15000 M_\odot$ clusters with different initial densities in Fig. 11. We find that the dense clusters

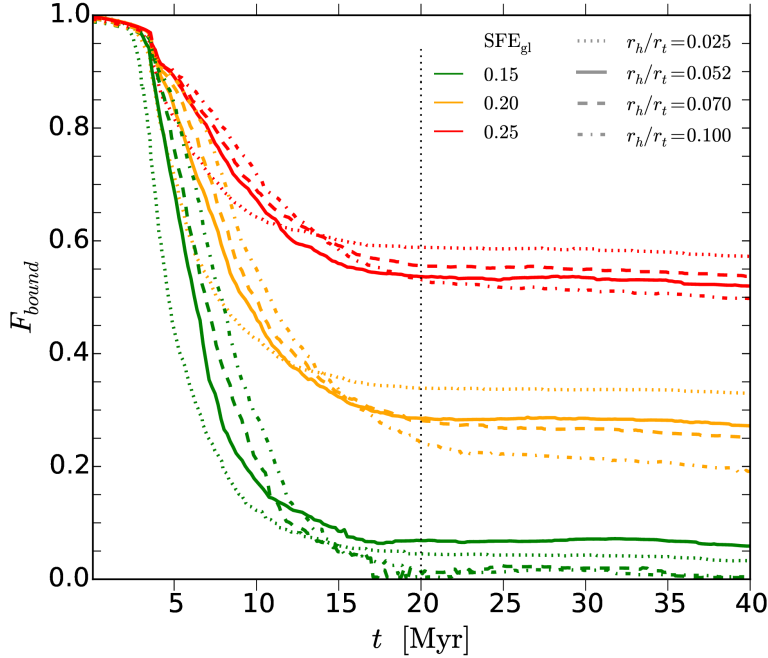


Figure 11: Evolution of the bound fraction of $M_\star = 15000 M_\odot$ clusters with different impact of the tidal field (see the key for the line-coding). Different colors correspond to different global SFEs (see the key for the color-coding).

evolve quicker than the less dense clusters within the first 20 Myr after gas expulsion. The violent relaxation duration of clusters and their bound mass

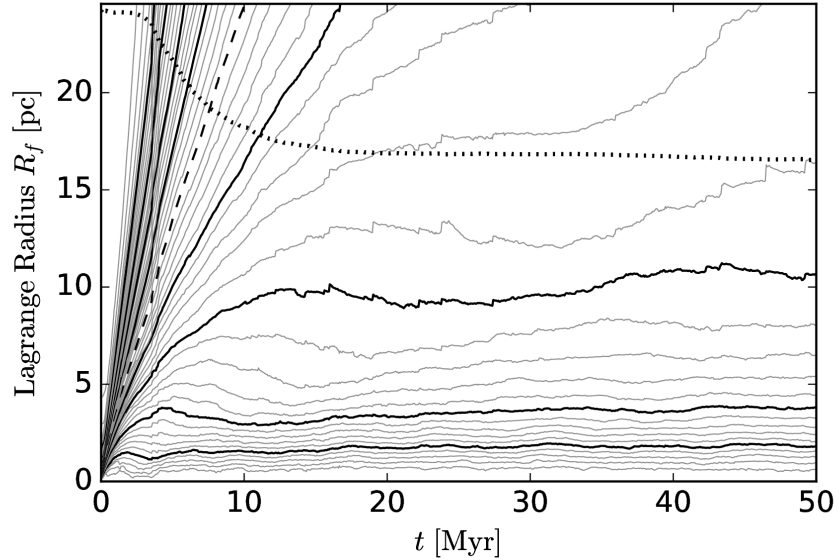


Figure 12: Evolution of the cluster with $M_* = 6000 M_\odot$, $SFE_{gl} = 0.20$ and $r_h/R_J = 0.025$ over the first 50 Myr after the instantaneous gas expulsion.

fraction at $t = 20$ Myr depend on the initial cluster mean densities. This is consistent with Parmentier and Baumgardt (2012) and Banerjee and Kroupa (2013), who showed that dense clusters have shorter revirialization times than less dense clusters. However, we find the cluster violent relaxation to depend fairly weakly on the initial stellar density. The difference during the first 10 Myr results from our definition of the bound mass fraction. That is, the most compact cluster ($r_h/R_J = 0.025$) loses mass in response to gas expulsion faster than the most diffuse cluster ($r_h/R_J = 0.100$). Its escaping stars reach the tidal radius twice faster because their velocity dispersions differ by a factor of 2. Although it is not obvious how to define the duration of violent relaxation accurately, Fig. 11 shows that it remains shorter than 20-25 Myr regardless of the cluster initial density. The key to understanding the violent relaxation duration may reside in the mean stellar density within the tidal radius, which is the same for all considered clusters since they all have the same orbit.

We note that stars that would be bound to the cluster if the cluster is isolated now become unbound once they cross the tidal radius of the cluster. Additionally, they are taken away from the cluster by the Galactic tidal field (see the different behaviors of the 30 percent Lagrange radius in Fig. 10 and Fig. 12).

In Fig. 12 we present an example of Lagrange radii evolution of a most compact cluster with $M_* = 6000 M_\odot$, $SFE_{gl} = 0.20$. We can see that the inner shells of the cluster with $r_h/R_J = 0.025$ revitalize faster than those of a more diffuse cluster with $r_h/R_J = 0.052$.

Figure 11 shows the differences in bound mass fraction at $t = 20$ Myr to be around 10 percent between the most compact and the most diffuse clusters. More diffuse clusters have a lower bound fraction since their outer shells expand beyond their instantaneous tidal radius. We have checked that a higher number of particles ($M_* = 15000 M_\odot$) does not affect our results.

3.4 FINAL BOUND MASS FRACTION IN DEPENDENCE OF SFE

We compare our results (represented by the mean values taken from the model clusters with $r_h/R_J = 0.052$ and different stellar masses) with previous works (Adams, 2000; Baumgardt and Kroupa, 2007; Boily and Kroupa, 2003b; Fellhauer and Kroupa, 2005; Geyer and Burkert, 2001; Lada, Margulis, and Dearborn, 1984) in the top panel of Fig. 32, which shows the bound fraction as a function of global SFE. We note here the improved survival likelihood of star clusters after instantaneous gas expulsion, and that although the tidal field is included in our models. Our model star clusters whose global SFE is lower than 30 percent, but higher than 15 percent, survive and retain a significant fraction of their stars after violent relaxation.

The global SFEs required by our model clusters to survive gas expulsion provide a good match to the SFEs observed in embedded clusters, which are lower than 30 percent (Higuchi et al., 2009; Kainulainen, Federrath, and Henning, 2014; Murray, 2011). Star clusters are now able to survive instantaneous gas expulsion despite a global SFE as low as 15-20 percent. We now have four avenues to understand the presence of star clusters with ages older than few Myr in the solar neighborhood despite the low SFE observed: adiabatic gas expulsion (Baumgardt and Kroupa, 2007; Brinkmann et al., 2017; Geyer and Burkert, 2001; Lada, Margulis, and Dearborn, 1984), sub-virial clusters (Farias et al., 2015; Goodwin, 2009; Verschueren and David, 1989), hierarchically formed clusters (Lee and Goodwin, 2016; Smith et al., 2011), and centrally concentrated cluster formation (this contribution).

We argue that the improved survivability of our model clusters is mostly caused by the difference in density profiles between the embedded cluster and its residual gas, as postulated by Parmentier and Pfalzner (2013), namely, the stars have a density profile steeper than that of the residual and initial gas. This is the consequence of SF taking place with a constant SFE per free-fall time in a centrally concentrated molecular clump.

We reproduce similar results to previous works when we plot the bound fraction as a function of the eSFE instead of the global SFE (see the bottom panel of Fig. 32). We note here again that in our models the eSFE and the LSF are almost the same. Our study thus agrees with all present works, including the most recent paper of Lee and Goodwin (2016), who concluded that the effective SFE is the most important parameter in predicting the cluster survivability. Our study allows us to compare model SFEs to those achieved in observed forming clusters, however.

3.5 CONCLUSIONS

We have performed N-body simulations of violent relaxation and bound cluster formation after instantaneous gas expulsion. The key point of our study is that we used special initial conditions built on the model of Parmentier and Pfalzner (2013). This means that the density profile of our model star cluster is steeper than the density profile of the star-forming gas at the time of instantaneous gas expulsion. If this cluster is in virial equilibrium, including the gravitational potential of residual gas, it should be able to survive gas expulsion despite low SFEs, as shown by Adams (2000) based on a semi-analytical model.

Since our N-body simulations start from the time of instantaneous gas expulsion and do not cover the SF phase, we started with a well-known star cluster model, namely the Plummer model, instead of starting from the star-free molecular clump. For this we obtained the dependency of the residual gas density profile on stellar density profile at the time of instantaneous gas expulsion under the assumptions of Parmentier and Pfalzner (2013). In their

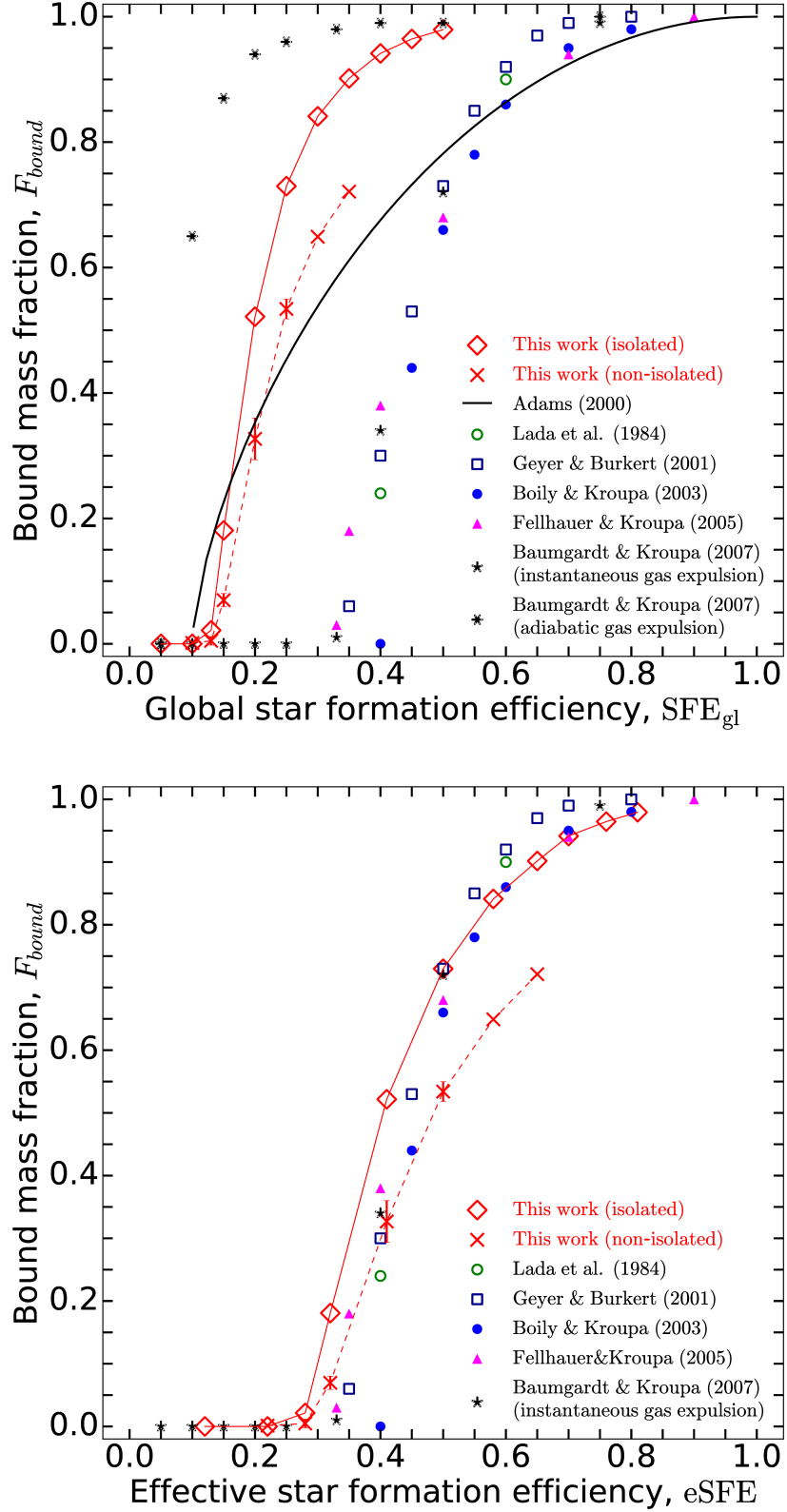


Figure 13: Bound fraction as a function of global or effective SFE. We compare our results (red lines) with previous works. The isolated models are depicted by the red diamonds, and non-isolated models by red crosses. In the top panel we use our global SFE (SFE_{gl}) and in the bottom panel, the eSFE, $eSFE = 1/Q_*$ (which is almost the same as the LSF, the local stellar fraction of our models).

cluster-formation model, the density profile of a clump (i.e., stars + gas) is constant during SF, and SF takes place with a constant SFE per free-fall time. Using this, we produced the initial conditions of embedded clusters for our N-body simulations, which depend on the product of two parameters (SFE per free-fall time and SF duration). With the equations we provide in the section 2.1, one can use any centrally concentrated spherically symmetric density profile for the embedded cluster and recover the initial and residual gas density profiles.

We adapted the `falcON` program `MKHALO` by McMillan and Dehnen (2007) to our problem and have written an additional acceleration plug-in, which represents the gravitational potential of the residual gas in dependence on the SF duration and SFE per free-fall time for a Plummer embedded cluster. Building on this adapted version of `MKHALO`, we produced the initial conditions of our simulations, that is, a Plummer star cluster in virial equilibrium with its residual gas with their respective density profiles obeying Eqs. (18) and (19) of Parmentier and Pfalzner (2013). We related the SF duration to the global SFE to make our set of simulations comparable to earlier works, in which the bound fraction is often presented in dependence on the global SFE.

We performed two types of cluster simulations, each time covering different global SFEs: 1) isolated single-mass clusters, and 2) non-isolated models, that is, star clusters with stellar evolution and dissolving within a Milky Way-like galaxy. We studied the effect of different initial cluster stellar masses as well as of different cluster densities on the evolution of our non-isolated models. The latter are implemented by varying the cluster half-mass to tidal-radius ratio, $r_h/R_J = 0.025, 0.052, 0.07, \text{ and } 0.10$.

Based on the performed simulations, we quantified the bound fraction evolution and the violent relaxation duration of young clusters. We defined the violent relaxation duration as the time span of cluster mass-loss in response to instantaneous gas expulsion. We note that with our definition, the violent relaxation duration differs from the cluster revirialization time. Our models for isolated single-mass clusters allowed us to define an upper limit to the bound fraction as a function of the global SFE. For the models considered in our work with their specific parameters – the stellar density profile (Plummer model), the cluster orbit (with a circular velocity, in the solar neighborhood in the Galactic disk plane), the stellar evolutionary mass-loss from the SSE routine (Hurley, Pols, and Tout, 2000) and for the cluster mean volume density range ($r_h/R_J = [0.025 : 0.100]$) – we conclude that the violent relaxation is not longer than 20 Myr, and its duration depends weakly on the initial stellar density of a cluster. We found that the violent relaxation duration of non-isolated model clusters depends neither on the cluster initial stellar mass nor on the global SFE, keeping the same initial stellar density. Varying the tidal field impact, that is, varying the cluster size while retaining the cluster mass, does not affect the cluster mass-loss in response to instantaneous gas expulsion much.

We also found that the minimum global SFE necessary to form a bound cluster after instantaneous gas expulsion is $\text{SFE}_{\text{gl}} = 0.15$ for a cluster with a circular orbit in the Galactic disk plane at a distance of $R_{\text{orb}} = 8$ kpc from the Galactic center. If the tidal field is stronger, that is, the cluster is closer to the Galactic center, the minimum SFE_{gl} needed to survive instantaneous gas expulsion may be different. For the given r_h/R_J ratio, the bound fraction of surviving clusters that achieved the same global SFE does not depend on the cluster initial stellar mass. The bound mass fraction at the end of violent relaxation for clusters with r_h/R_J of 0.025 and 0.10 differs by only about 10 percent, with denser clusters retaining a higher bound fraction than more diffuse clusters. The evolution of bound clusters after violent relaxation is

mostly driven by the tidal field of the host galaxy, and their life expectancy then depends on their stellar mass.

We compared our results with earlier works. Our final bound fractions are similar to those found in previous works only when the bound fraction is plotted in dependence of the eSFE. Thus we agree with Goodwin (2009) that the virial ratio of a cluster at the time of gas expulsion is a key parameter for predicting whether it survives gas expulsion. However, when working in terms of the global SFE, that is, the SFE that can be measured by observers as the ratio between the stellar mass and the total (gas+star) mass of a star-forming region, the models proposed in this paper improve the survival likelihood of star clusters after instantaneous gas expulsion. This is caused by the difference in density profiles between the embedded cluster and its residual gas, namely, the stellar density profile has a steeper slope than that of the residual gas, which is a consequence of SF taking place with a constant star-formation efficiency per free-fall time in a centrally concentrated molecular clump.

CLUSTER DISSOLUTION AND CENTRALLY-PEAKED SFE PROFILE

This chapter is a partially revised version of the published peer-reviewed paper Shukirgaliyev, B., G. Parmentier, A. Just, and P. Berczik (2018). “The Long-term Evolution of Star Clusters Formed with a Centrally Peaked Star Formation Efficiency Profile.” In: *ApJ* 863(2), 171. B. Shukirgaliyev performed all N-body simulations, analyzed their outputs and wrote most of the text. All authors contributed ideas, comments and suggestions throughout the realization of this study and its preparation as a peer-reviewed paper.

4.1 INTRODUCTION

In previous chapter we have studied how star clusters respond to instantaneous gas expulsion when they form according to the local-density-driven cluster formation model of Parmentier and Pfalzner (2013). That is, model clusters form in centrally-concentrated spherically-symmetric molecular clumps with a constant star-formation efficiency per free-fall time. As a consequence, their *stellar volume density profile is steeper than that of the initial and residual star-forming gas*.

In this chapter, we expand our results and look at the problem of cluster dissolution during the first Gyr of evolution anew. If in chapter 3 we have studied the violent relaxation of star clusters for different stellar masses and global SFEs, now we focus on their long-term evolution. We also focus on our model clusters formed with a low global SFE, i.e. $SFE_{gl} = 0.15$, and investigate if they behave in a similar way to the overfilling cluster models of Ernst et al. (2015), and if they show evidence of MID. In contrast to their study, our model clusters bear the information about their formation conditions and the violent relaxation which follows gas expulsion.

4.2 METHODS

4.2.1 Cluster models

We continue our existing set of direct N-body simulations until the full dissolution of the model star clusters in the tidal field of the Galaxy. We use only the models with $r_h/R_J = 0.05$ and which survive as bound clusters after violent relaxation (i.e. $SFE_{gl} \geq 0.15$). We completed this initial model set with newly-run $SFE_{gl} = 0.17$ models for some birth masses and $SFE_{gl} = 0.15$ models for birth masses higher than what was considered in Chapter 3 (i.e. $M_* = 60k M_\odot$ and $100k M_\odot$, equivalent to $N_* = 105554$ and 174257 stars, respectively, for a Kroupa (2001) IMF with $m_{low} = 0.08 M_\odot$ and $m_{up} = 100 M_\odot$). All model clusters considered in this study have evolved from the time of instantaneous gas expulsion until full dissolution. Therefore all of them bear the information about their formation conditions and violent relaxation. The full parameter space covered by our N-body simulations is provided in Table 7.

Table 6: Model cluster parameters. The columns are as follow: (1) total number of stars, (2) birth mass, (3) global SFE, (4) number of random realizations per model (number of those calculated till cluster dissolution), (5) mean bound mass fraction at the end of violent relaxation and its standard deviation when more than one random seed, (6) mean dissolution time.

N_*	$\frac{M_*}{M_\odot}$	SFE_{gl}	n_{rnd}	$\langle F_{bound} \rangle$	$\left\langle \frac{t_{dis}}{10^9 \text{ yr}} \right\rangle$
5225	3000	0.15	21 (21)	0.07 ± 0.05	0.19 ± 0.11
5225	3000	0.17	1 (1)	0.21	0.52
5225	3000	0.20	1 (1)	0.29	0.71
5225	3000	0.25	1 (1)	0.53	1.07
10455	6000	0.15	26 (26)	0.06 ± 0.04	0.23 ± 0.16
10455	6000	0.17	1 (1)	0.21	0.66
10455	6000	0.20	3 (1)	0.31 ± 0.02	1.29
10455	6000	0.25	3 (1)	0.50 ± 0.03	1.56
17425	10000	0.15	26 (26)	0.06 ± 0.03	0.33 ± 0.15
17425	10000	0.20	1 (1)	0.38	2.11
17425	10000	0.25	1 (1)	0.51	2.55
26138	15000	0.15	22 (22)	0.08 ± 0.04	0.53 ± 0.24
26138	15000	0.17	1 (1)	0.18	1.02
26138	15000	0.20	3 (1)	0.33 ± 0.02	1.84
26138	15000	0.25	3 (1)	0.51 ± 0.01	2.86
52277	30000	0.15	16 (16)	0.08 ± 0.03	0.64 ± 0.32
52277	30000	0.17	1 (1)	0.16	1.37
52277	30000	0.20	1 (1)	0.34	3.58
52277	30000	0.25	1 (1)	0.56	5.49
104554	60000	0.15	15 (9)	0.08 ± 0.02	0.75 ± 0.35
174257	100000	0.15	3 (3)	0.08 ± 0.01	0.96 ± 0.34

4.2.2 *Random realizations*

In chapter 3 we mentioned that the bound mass fraction at the end of violent relaxation, F_{bound} (i.e. the stellar mass fraction remaining bound to the cluster at an age of 20-30 Myr¹) can vary by about 6-10 percent of the birth mass for different random realizations of a given model. Such variations are almost negligible for model clusters with a high $\text{SFE}_{\text{gl}} > 0.15$, as they survive with more than 20 percent of the birth mass. However, the situation changes for our $\text{SFE}_{\text{gl}} = 0.15$ models, as they survive with the lowest bound mass fraction (about or even below 0.10), being the transition models from full destruction following gas expulsion to survival in the parameter space of SFE_{gl} . For such a low bound mass fraction the variations mentioned above are significant. Therefore, we performed additional random realizations of the $\text{SFE}_{\text{gl}} = 0.15$ models to have better statistics for our study. In forth column of Table 7 we give the numbers of random realizations per model and in parentheses the number of runs completed till cluster dissolution. The column 5 shows the mean bound mass fractions and their standard deviations measured at $t = 30$ Myr. The discussions and results on random realizations are presented further in section 4.3.

4.2.3 *Cluster mass estimates*

To estimate cluster masses is a complex issue, both from an observational and theoretical point-of-view. Even the very definition of a star cluster varies through the literature (e.g. see review in Renaud, 2018). To estimate the luminous mass of an observed star cluster is not straightforward due to incompleteness issues and field star contamination. To estimate the dynamical mass of an observed cluster is hindered by the contribution of binaries to the cluster overall velocity dispersion. From a theoretical point of view, the mass determination is not straightforward due to the unknown second integral of motion.

In chapter 3, we refer to the cluster mass as the stellar mass within one Jacobi radius, R_J , which is also supposed to be the bound mass. To calculate the Jacobi radius of a cluster at a given age, we start with its value at the time of gas expulsion and the stellar mass it contains using Eq (13) from Just et al. (2009). Then we re-calculate the Jacobi radius using the mass within the previously defined Jacobi radius. We iterate until the Jacobi radius converges. Our Jacobi radius calculation method works only if we define the cluster density center correctly, which can prove an issue for the following reasons. In our N-body simulations we keep track of all stars, even those which have definitively escaped the cluster in which they initially formed. Therefore, escaped stars live in the tidal tails of our model clusters, which can extend as far as to wrap around the Galaxy making it difficult to define the cluster center as a center of mass of all stars. That the tidal tails contain epicyclic over-densities yields difficulties to find the exact cluster center too. That is, we have struggled to find the correct cluster center in the late stages of cluster evolution, as they are becoming low-mass and diffuse objects. Their low densities can be then comparable to that of the surrounding field, or to the epicyclic over-densities of the tidal tails. Our algorithm can thus incorrectly identify the center of a tidal tail over-density as the cluster center. In order to prevent this, we use to calculate the cluster center only those stars which were within $2R_J$ of it in the previous N-body simulation snapshot. This allowed us to steer clear of the epicyclic over-densities of

¹ In this chapter we refer to the end of violent relaxation as $t = 30$ Myr after instantaneous gas expulsion.

the tidal tails. Yet, it remains difficult to define correctly the cluster center, when it consists of few stars, has an extended core, a low volume density, or presents sub-structures. Usually, this happens in the last stages of evolution of star clusters, before they get fully destroyed by the Galactic tidal field. In such clusters, relatively small shifts of the assumed cluster center can lead to significantly wrong mass estimates because of a wrong Jacobi radius, R_J .

In order to avoid this, we assume that clusters are dissolved if they have less than $100 M_\odot$ left within 2 Jacobi radii:

$$t_{\text{dis}} = t(M_{2J} < 100M_\odot), \quad (31)$$

where M_{2J} is the stellar mass enclosed within 2 Jacobi radii.

We have checked how long some of our model clusters can live beyond the dissolution time, t_{dis} , defined by Eq. (31). Typically the difference is about a few tens of Myr, which is not significant, especially for clusters whose lifetime scales up to a Gyr.

In this contribution we consider two types of cluster-mass estimates. One is the Jacobi mass (or “bound mass”), M_J , which is the stellar mass within one Jacobi radius, R_J . The other one, which we refer to as the “extended mass” M_{2J} , is the stellar mass within $2R_J$. The second mass estimate is important for young clusters as they are surrounded by an envelope of unbound stars (Elson, Fall, and Freeman, 1987), most of them located beyond one Jacobi radius but still within $2R_J$. Such envelopes persist for many Myrs, as Fig. 14 will show. They can count towards the mass of clusters in extragalactic studies, where a membership analysis is impossible, and the cluster mass is estimated by fitting the cluster surface brightness profile.

Figure 14 visualizes the evolution of star clusters with a birth mass of $M_\star = 15k M_\odot$ in the form of volume density maps. Each point in these plots correspond to the position of one star projected onto the Galactic disk plane. The colors correspond to the local volume density obtained by a nearest-neighbor scheme with $N_{\text{nb}} = 50$ neighbor stars. The coordinate system is centered on the density center of the clusters and the two circles correspond to $1R_J$ and $2R_J$. The left and middle panels depict two random realizations of the model with $\text{SFE}_{\text{gl}} = 0.15$ and the right column corresponds to $\text{SFE}_{\text{gl}} = 0.25$. In each column, different snapshots are presented ($t = 0, 5, 10, 30, 70$ Myr).

In Fig. 15 we show the radial volume density profiles of the same 3 model clusters as in Fig. 14 calculated at the end of violent relaxation ($t = 30$ Myr, top panels), and at a later time when clusters are almost cleared of their envelope stars ($t = 70$ Myr, bottom panels). Each point represents the density at the location of one star, calculated using a 50-nearest-neighbor scheme. In each panel, the vertical dashed lines correspond to 1 and 2 Jacobi radii, and the horizontal dotted line corresponds to the mean stellar density within one Jacobi radius, i.e. $\langle \rho_J \rangle = M_J / (4/3\pi R_J^3)$. According to Eq. (13) of Just et al. (2009), for a given environment, i.e. for a fixed circular orbit in the Galactic disk plane, the mean density within one Jacobi radius, $\langle \rho_J \rangle$, is constant and independent of cluster parameters, since $R_J \propto M_J^{1/3}$. In our case, for a circular orbit with $R_G = 8$ kpc, the mean density within one Jacobi radius is $\langle \rho_J \rangle \approx 0.1 M_\odot \text{pc}^{-3}$.

In the left panels of Fig. 15, the region between $1R_J$ and $2R_J$ is well populated by stars such that the distant observer, when calculating the cluster mass by fitting its projected density profile, will use the envelope stars too. For the middle and right columns, however, the envelope stars do not contribute much to the cluster mass, as evidenced by the density contrast between the central part and the outskirts of the clusters (see Fig. 14 and Fig. 15). These density contrasts are about 1-2 orders of magnitude in the

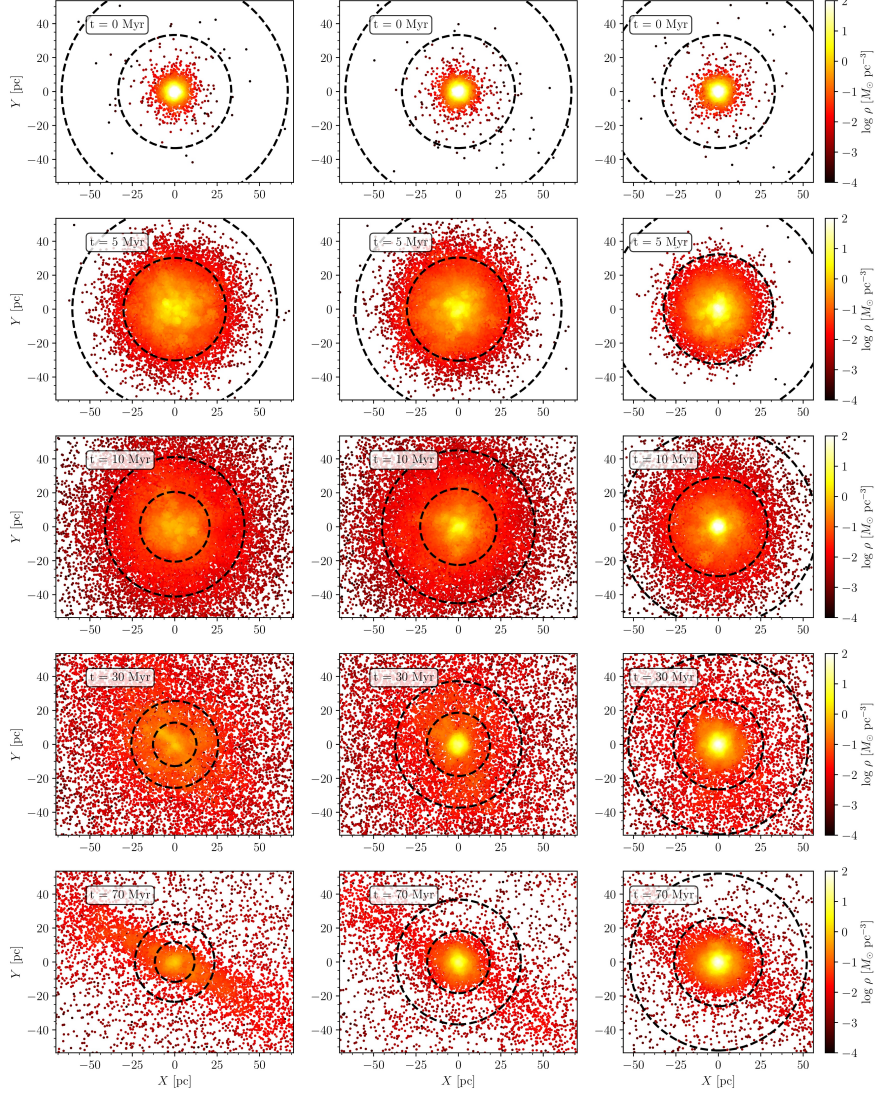


Figure 14: Volume density maps of clusters with a birth mass of $M_{\star} = 15000M_{\odot}$ projected onto the Galactic plane. The left and middle columns correspond to two random realizations of a model cluster with $SFE_{g1} = 0.15$, and the right column corresponds to a $SFE_{g1} = 0.25$ model. From top to bottom, we provide 5 different snapshots of each model cluster at times $t = 0, 5, 10, 30, 70$ Myr. Each point corresponds to one star whose color-coding depicts the local volume density calculated by means of a 50-nearest-neighbor scheme. *Note: the color-scale does not show densities higher than $100 M_{\odot}pc^{-3}$ in order to show the color contrast in low density regions at a later time of cluster evolution. The central densities at the time of gas expulsion are as high as $1.6 \cdot 10^3 M_{\odot}pc^{-3}$.* The dashed circles correspond to R_J and $2R_J$. The bound fractions at $t = 30$ Myr are, from left to right: $F_{\text{bound}} = 0.06, 0.18$ and 0.5 . The corresponding dissolution times are $t_{\text{dis}} = 0.3$ Gyr, 1.2 Gyr and 2.9 Gyr, respectively.

left panels, about 3 orders of magnitude in the middle panels and about 4-5 orders of magnitude in the right panels.

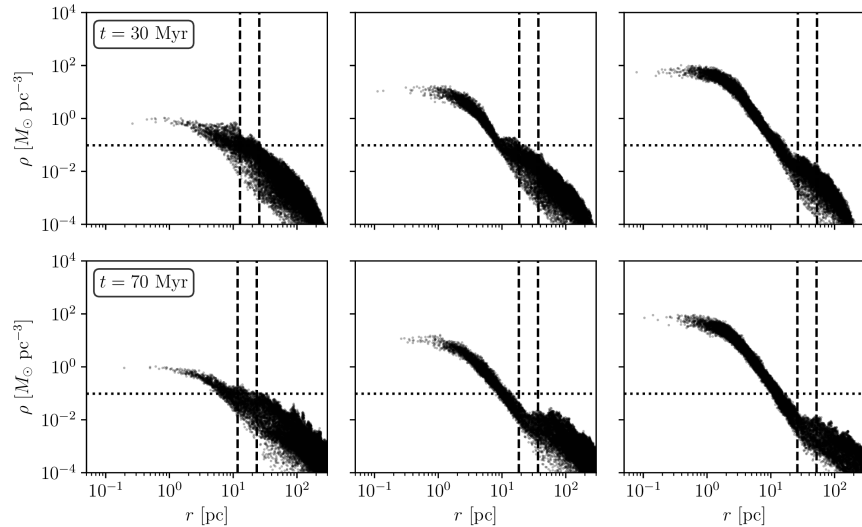


Figure 15: Volume density profiles of model clusters whose birth mass is $M_{\star} = 15000M_{\odot}$ (same models as in Fig. 14). Each point represents the density at the location of one star. Left and middle panels correspond to two random realizations of the $SFE_{gl} = 0.15$ model, while the right panels correspond to the $SFE_{gl} = 0.25$ model cluster. The top and bottom panels correspond to the density profiles calculated at $t = 30$ Myr and $t = 70$ Myr, respectively. In each panel, the vertical lines show the location of $1R_J$ and $2R_J$. The horizontal lines correspond to the mean density within one Jacobi radius, $\langle \rho_J \rangle$, which is constant for the considered Galactic orbit of star clusters.

4.3 STOCHASTICITY DURING CLUSTER EXPANSION

Based on our random realizations of $SFE_{gl} = 0.15$ model clusters, we have studied how distributed the bound mass fractions F_{bound} at the end of violent relaxation ($t = 30$ Myr) are. F_{bound} is here defined as the ratio between the Jacobi mass and the birth mass of a cluster:

$$F_{\text{bound}} = M_J(t = 30\text{Myr})/M_{\star}.$$

Figure 16 shows the mean bound mass fractions of our $SFE_{gl} = 0.15$ cluster models as a function of the birth masses, where the error-bars depict the standard deviation. The solid line and the shaded area depict the total mean bound mass fraction, $\langle F_{\text{bound}} \rangle$, and total standard deviation, obtained for all $SFE_{gl} = 0.15$ model clusters. We find $\langle F_{\text{bound}} \rangle = 0.07 \pm 0.04$. As we see from Fig. 16 the mean bound mass fraction does not significantly depend on the birth mass, being equal to the total mean bound mass fraction within the error bars. That the standard deviations are decreasing with increasing birth mass can result from the smaller numbers of random realizations implemented for models with higher birth mass (see the column 4 in Table 7 for $SFE_{gl} = 0.15$ models). We also find that the bound mass fractions do not change significantly from $t = 30$ Myr to $t = 70$ Myr.

Our simulations show that a number of stars as high as $N_{\star} = 100k$ ($M_{\star} = 60kM_{\odot}$) does not remove the relatively large scatter characterizing the bound fraction of the $SFE_{gl} = 0.15$ models. We think that this might be a consequence of the Poisson noise in the initial phase-space distribution of stars, and of some stochasticity taking place during the cluster expansion. Our model clusters with such a low global SFE as $SFE_{gl} = 0.15$ can

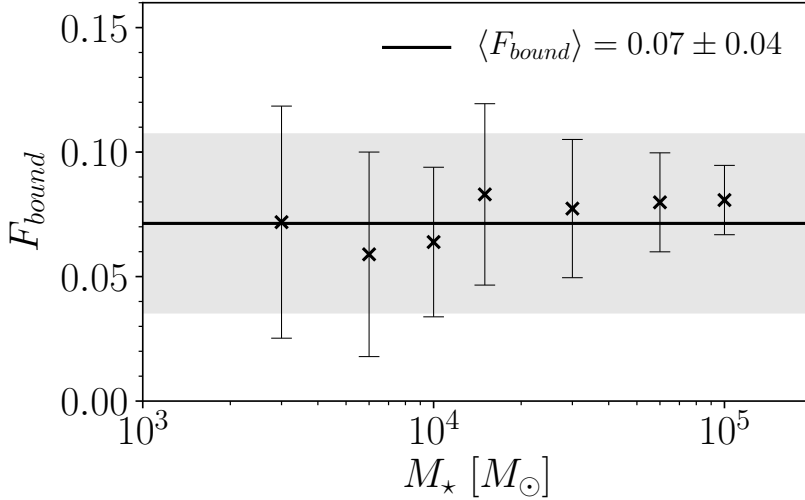


Figure 16: The mean bound mass fractions at the end of violent relaxation obtained from random realizations of cluster models with $SFE_{gl} = 0.15$ as a function of the birth mass of star clusters. The error-bars correspond to the standard deviations. The solid line shows mean bound mass fraction of all model clusters with $SFE_{gl} = 0.15$ and shaded area corresponds to the standard deviation.

expand so much after gas expulsion, that their central density drops down significantly. Density sub-structures can form in the inner region, where density profile becomes shallower, as a result of the local gravitational potential wells of massive stars (more massive than $8M_{\odot}$). Even during the early expansion phase, individual high-mass stars can attract and retain many co-moving stars in their vicinity. That is, stars co-moving with a nearby high-mass star can get trapped by its gravitational potential. As a result, these surrounding stars start to move collectively towards their neighboring high-mass star and deepen the local potential well. This collective motion continues even after the high-mass star goes supernova. The more high-mass stars involved in this sub-cluster formation process, the more massive the sub-cluster formed. Eventually, the sub-structures formed during expansion can merge into one bigger cluster, or expand further and dissolve depending on their bound mass and kinetic energy. This can be seen by comparing the left and middle panels of Fig. 14, as we discuss later in this section.

Stochastic effects could be significant at this stage due to the relatively small number of massive stars which do not escape the cluster. Since we have applied the Kroupa (2001) IMF, the number fraction of massive stars is about 0.6 percent. That means we have about 600 massive stars at the time of gas expulsion for a cluster with $N_{\star} = 100k$ stars and about 60 high-mass stars for a $N_{\star} = 10k$ cluster. If about 93 percent of these massive stars escape to the field, as expected for a $SFE_{gl} = 0.15$ model whose mean bound fraction is $F_{bound} = 0.07 \pm 0.04$, at the end of violent relaxation we are left with about 42 massive stars within one Jacobi radius R_J for the former, and about only 4-5 high-mass stars for the latter.

If we look at the left and middle columns of Fig. 14 we can see the evolution of two initially identical cluster models with $M_{\star} = 15k M_{\odot}$ and $SFE_{gl} = 0.15$. Although model clusters in the left and middle panels are almost identical at the time of gas expulsion ($t = 0$ Myr), they slightly differ

from each other already at $t = 5$ Myr, the one in the middle panel being slightly more centrally-concentrated than the other. Both clusters have almost the same Jacobi radii R_J , and therefore, the same bound mass (i.e. the stellar mass within one Jacobi radius, R_J). However, this is still the expansion phase. The middle-panel cluster has a slightly higher number of massive stars close to its center, while the massive stars of the left-panel cluster are distributed broadly within R_J . This is seen by the distribution of local over-densities at the centers of which high-mass stars are usually located.

Later, at $t = 10$ Myr the difference becomes even clearer. The left-panel cluster has an extended core whose size is almost one Jacobi radius, while the middle-panel cluster has formed a relatively dense central core. Again, at this time, both clusters have comparable bound masses, but markedly different structures already.

At the end of violent relaxation at $t = 30$ Myr (when clusters stop losing mass in response to gas expulsion, although not the re-virialization time yet) and later on at $t = 70$ Myr, these two $SFE_{gl} = 0.15$ clusters present markedly different bound masses, even though they started with the same birth mass and the same global SFE. This is the consequence of the highly-stochastic spatial distribution of high-mass stars inside a broad central core.

By $t = 70$ Myr model clusters have re-virialized and regain a more spherically-symmetric shape within the Jacobi radius, which becomes a good estimator of the cluster radius onward. The clusters are cleaned from the envelope stars and we can see the tidal tails as streaky features at $t = 70$ Myr (see the lowest panels of Fig. 14). We remind the reader that we have axisymmetric (bulge, halo, disk) Galactic potential without any other features like spiral arms, bar or disk wrap.

4.4 WHAT DOES CLUSTER DISSOLUTION DEPEND ON?

4.4.1 Cluster life expectancy and initial cluster mass

In this section we study the relation between cluster dissolution time and mass. From the random realizations of model clusters with $SFE_{gl} = 0.15$ we find that the differences in bound mass fraction at the end of violent relaxation also results in different star cluster lifetimes. Figure 17 presents the dissolution time t_{dis} of star clusters as a function of the bound mass fraction F_{bound} at the end of violent relaxation. The cluster dissolution time is defined according to Eq. (31). The color-coding and symbol-coding correspond to cluster birth mass and global SFE, respectively (see the key). The general trend is that the higher the bound mass fraction, the longer lives a cluster. However, the large scatter and the fact that Fig. 17 considers various birth masses do not give us much more information about the relation between cluster dissolution time and its mass.

The cluster dissolution time, t_{dis} , as a function of cluster “initial” mass is presented in Fig. 18. By “initial” mass, M_{init} , we mean here the cluster mass once violent relaxation is over, that is, when the long-term secular evolution starts. Our cluster “initial” masses are therefore measured at $t = 30$ Myr (top panels) and $t = 70$ Myr (bottom panels), and are lower than the birth masses given in Table 7 (the ratio between Jacobi and birth masses is the bound fraction F_{bound}). We have done so to be consistent with studies which ignore the violent relaxation phase of cluster evolution when inferring the cluster dissolution time as a function of cluster mass.

When plotting the cluster dissolution time as a function of cluster initial mass, not only do we measure the mass at two different cluster ages, we also consider two definitions of cluster masses in terms of cluster spatial coverage. Specifically, the cluster initial mass is defined either as the Jacobi mass

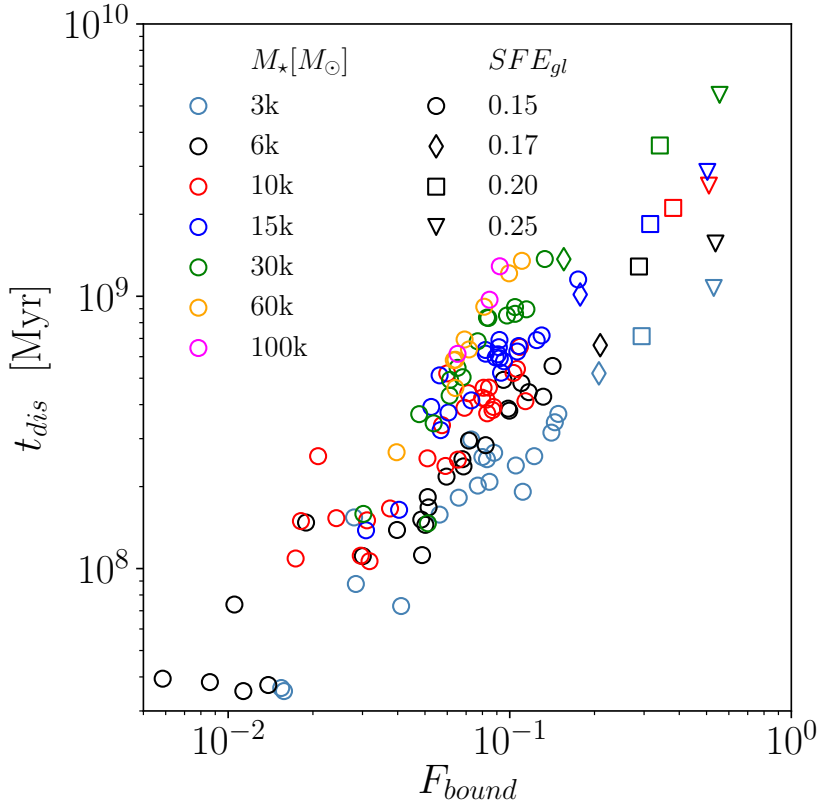


Figure 17: Cluster dissolution time as a function of bound mass fraction. Cluster birth mass and global SFE are indicated by colors and symbols, respectively, according to the key.

M_J (left panels), or as the “extended mass” M_{2J} (right panels). We therefore investigate 4 different cases in total. The color-coding shows the birth mass of the model clusters, while the different symbols correspond to different SFE_{gl} (see the key). The scatter arising from the random realizations of a given model (given birth mass and given SFE_{gl}) is therefore illustrated by symbols of a given color and of a given type.

The solid line, with the shaded area accounting for the error-bars, corresponds to the MDD relation of [Boutloukos and Lamers \(2003\)](#)

$$t_{dis} = t_4^{dis} \left(\frac{M_{init}}{10^4 M_\odot} \right)^\gamma, \quad (32)$$

where M_{init} is cluster “initial” mass and t_4^{dis} is the dissolution time for a cluster with “initial” mass of $M_{init} = 10^4 M_\odot$. Here we re-call that M_{init} is the equivalent of the Jacobi mass, M_J , or the extended mass, M_{2J} , at $t = 30$ or 70 Myr, but not of the birth mass, M_* . The values of $t_4^{dis} = (1.3 \pm 0.5) \cdot 10^9$ Gyr and $\gamma = 0.6$ are taken from [Lamers et al. \(2005\)](#) for the solar neighborhood. The dashed and dash-dotted lines show the best fits to our high-SFE ($SFE_{gl} \geq 0.20$) and low-SFE ($SFE_{gl} = 0.15$) model clusters, respectively. The bold red curve in the lower-right panel connects, for each cluster birth mass (i.e. for each symbol color), the medians of $SFE_{gl} = 0.15$ model random realizations.

The overall impression from [Fig. 18](#) is that star clusters dissolve in agreement with MDD, although with some significant scatter. Especially model clusters formed with a relatively high global SFE ($SFE_{gl} \geq 0.20$, open squares

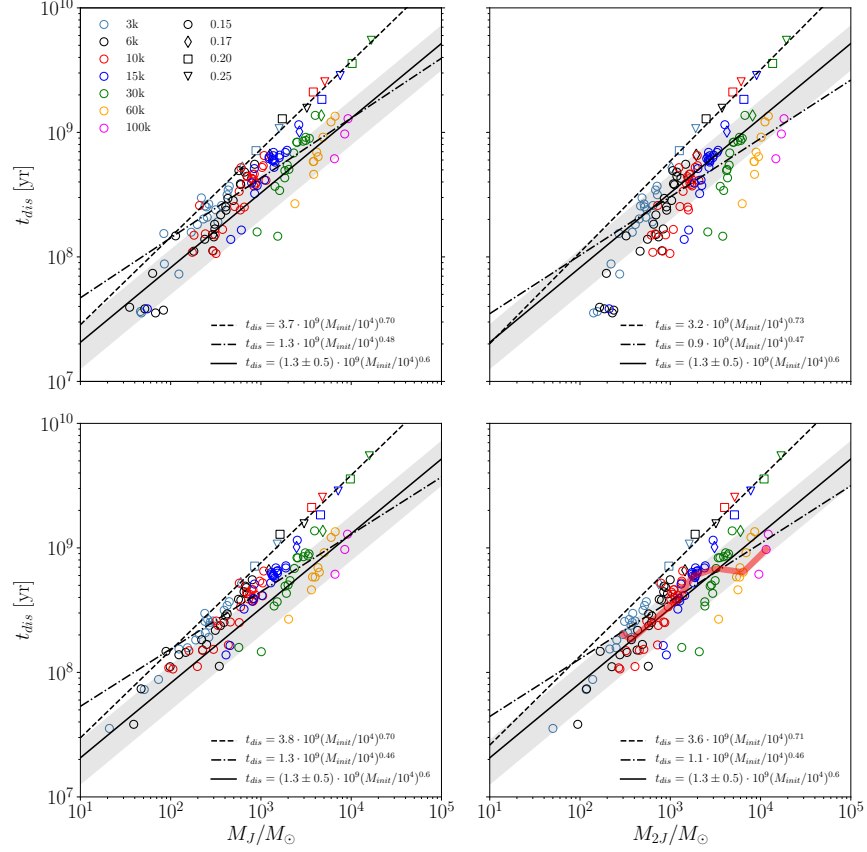


Figure 18: Star cluster dissolution time versus cluster mass at the end of violent relaxation ($t = 30$ Myr in top panels and $t = 70$ Myr in bottom panels). We refer to this as the cluster “initial” mass. The left panels show the cluster “initial” mass defined as the Jacobi mass, M_J , while the right panels present it as the “extended mass”, M_{2J} . Each point represents one cluster model, with the color-coding defining the cluster birth mass, and marker shapes coding the global SFE. The solid line with shaded area corresponds to the cluster disruption model for the solar neighborhood of Lamers et al. (2005). The dashed and dash-dotted lines depict the best fits to high-SFE ($\text{SFE}_{\text{gl}} \geq 0.20$) and low-SFE ($\text{SFE}_{\text{gl}} = 0.15$) model clusters. The red curve in the lower-right panel connects the median random realizations of the models with $\text{SFE}_{\text{gl}} = 0.15$.

and triangles in Fig. 18) nicely follow an MDD relation (dashed line), with a slope a bit steeper ($\gamma \sim 0.7$) than that given by Boutloukos and Lamers (2003), and a dissolution time longer ($t_4^{\text{dis}} \sim 3.8$ Gyr, lower left panel of Fig. 18) than the estimate of Lamers et al. (2005) for the Solar Neighbourhood (solid line). This is consistent with other theoretical works, that Roche-volume-filling or under-filling clusters in virial equilibrium dissolve in a mass-dependent way. However, the cluster dissolution time obtained from our high-SFE models ($t_4^{\text{dis}} \sim 3.8$ Gyr) is almost a factor of two shorter than that predicted by Baumgardt and Makino (2003) with their $t_4^{\text{dis}} = 6.9$ Gyr. This can result from different models for the Galactic gravitational potential: while we consider an axisymmetric three-component model (Just et al., 2009), Baumgardt and Makino (2003) consider a spherically-symmetric logarithmic potential. Another probably more crucial reason is the “initial” density profile of the star clusters: our density profiles at $t = 30$ Myr differ from the virialized

King models (with $W_0 = 5$ and $W_0 = 7$) used by Baumgardt and Makino (2003).

We do not notice any significant difference for the high-SFE models between the 4 panels. Therefore, for the high-SFE models, how the cluster initial mass is defined (at $t = 30$ or $t = 70$ Myr; bound mass, M_J or extended mass, M_{2J}) hardly influences the corresponding predicted MDD relation.

In contrast to high-SFE ones, low-SFE models show broad scatter and differ from panel to panel. The scatter is maximum for extended mass at $t = 30$ Myr (upper right panel) and minimum for Jacobi mass at $t = 70$ Myr (lower left panel). Since the difference between the Jacobi mass and the extended mass is larger for low-SFE clusters and negligible for high-SFE clusters the initial masses are characterized by a broader scatter in right panels than in left panels of Fig. 18. When the clusters have evolved a bit more in time, the envelope gets cleaned up by an age of $t = 70$ Myr and the extended mass of our model clusters then becomes comparable to their Jacobi mass (bottom panels of Fig. 18), although the scatter persists. Our best fits to low-SFE models provide a dissolution time in agreement with Lamers et al. (2005), $t_4^{\text{dis}} \sim 1.3$ Gyr, but a slightly shallower slope $\gamma \sim 0.5$ (lower left panel of Fig. 18). For the $\text{SFE}_{\text{gl}} = 0.15$ models, we can see that the scatter in bound mass fractions can yield significant differences in the cluster lifetime (open circles of a given color). As shown in Fig 14 and 15, (left and middle panels) this is the result of the development with time of markedly different density profiles. Additionally, if we consider a vertical bin embracing cluster masses from 2×10^3 to $4 \times 10^3 M_\odot$ in the right panels of Fig. 18, we can see that such clusters can dissolve as fast as within 100–200 Myr or can live as long as about a Gyr.

For the sake of clarity Fig. 19 shows each low-SFE model (i.e. given birth mass and global SFE) represented by its mean and standard deviation. The initial mass is defined as the extended mass, M_{2J} , and the age is $t = 70$ Myr. Figure 19 is thus equivalent to the lower right panel of Fig. 18, apart from the low-SFE models being represented by mean values. Now the results for the $\text{SFE}_{\text{gl}} = 0.17$ models can be seen clearly as open diamonds with the corresponding fit having $t_4^{\text{dis}} = 1.8$ Gyr and $\gamma \sim 0.5$ (dotted line). The other lines are as in the lower right panel of Fig. 18, namely, the MDD relation of Boutloukos and Lamers (2003) and the best fits to the $\text{SFE}_{\text{gl}} \geq 0.20$ and $\text{SFE}_{\text{gl}} = 0.15$ models. The combination of these 3 groups of star clusters can yield a relation close to that of Boutloukos and Lamers (2003), especially if low-SFE clusters dominate the cluster population. This is a real possibility for the solar neighborhood, since observations of nearby gas-embedded clusters tell us that low-SFE embedded clusters are more common than high-SFE ones (Evans et al., 2009; Kainulainen, Federrath, and Henning, 2014; Kennicutt and Evans, 2012; Lada and Lada, 2003; Peterson et al., 2011).

Gieles et al. (2006) noted that the dissolution time of a $10^4 M_\odot$ cluster in the solar neighborhood as inferred from observations by Lamers et al. (2005) ($t_4^{\text{dis}} = 1.3 \pm 0.5$ Gyr) differs by about a factor of 5 from what was predicted by Baumgardt and Makino (2003) ($t_4^{\text{dis}} = 6.9$ Gyr). They suggested that the discrepancy can be eliminated by accounting for the influence on star clusters of Giant Molecular Cloud encounters. Here, we propose yet another channel to explain the shorter dissolution time of Lamers et al. (2005), namely, that the star clusters of the solar neighborhood are predominantly the survivors of embedded clusters formed with a global SFE of $\text{SFE}_{\text{gl}} \approx 0.15$. We expect that most of these clusters will dissolve by the time they reach an age of 1 Gyr. In contrast to other theoretical studies who consider compact clusters in virial equilibrium as initial conditions, our model clusters have experienced violent relaxation, which is a natural process affecting the evolution of young clusters. With our approach we are thus able

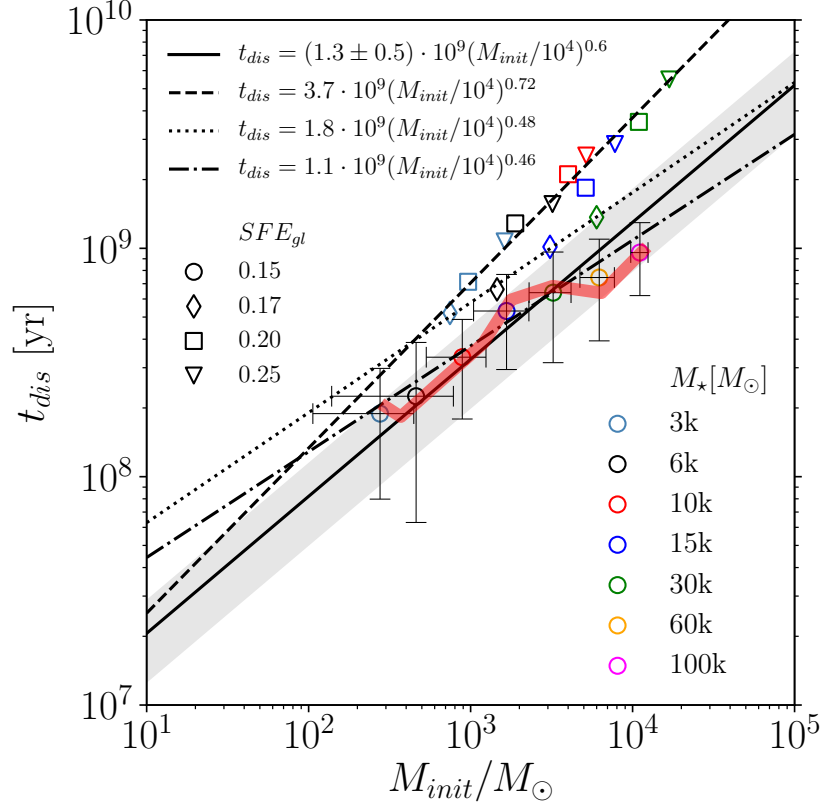


Figure 19: Cluster dissolution time as a function of extended mass at $t = 70$ Myr. The $SFE_{gl} = 0.15$ models are represented by the mean extended mass and mean dissolution time per model with error bars representing the standard deviations. The red curve connects median random realizations of each model as in the lower right panel of Fig. 18. The dashed, dotted and dash-dotted lines are best fits to the $SFE_{gl} \geq 0.20$, $SFE_{gl} = 0.17$ and $SFE_{gl} = 0.15$ models. The solid line with shaded area corresponds to the MDD relation of Boutloukos and Lamers (2003) for the solar neighborhood (Lamers et al., 2005).

to simulate the evolution of clusters which have survived violent relaxation as bound, but diffuse, objects. They dissolve faster than their compact counterparts, even for otherwise equal “initial” masses, and we probably observe them as open clusters in the solar neighborhood.

If the low-SFE clusters dominate the cluster census of Galactic disk, then not many clusters are able to live beyond 1 Gyr as we can see from Fig. 20. It shows the histogram of cluster dissolution times for low-SFE ($SFE_{gl} = 0.15$, blue) and higher-SFE ($SFE_{gl} \geq 0.17$, orange) clusters. Each histogram is normalized such that the sum of all bins equals to unity. The combination of both distributions, each with each own contribution, will provide the distribution of dissolution times of a cluster population. The latter can give us a hint about the shape of the corresponding cluster age distribution. A cluster population dominated by low-SFE clusters should feature a peak in cluster logarithmic age distribution ($dN/d \log t$) earlier than 1 Gyr (if the cluster formation rate is constant), since most low-SFE clusters die before 1 Gyr. The peak at about a few hundred Myr in the age distribution of solar

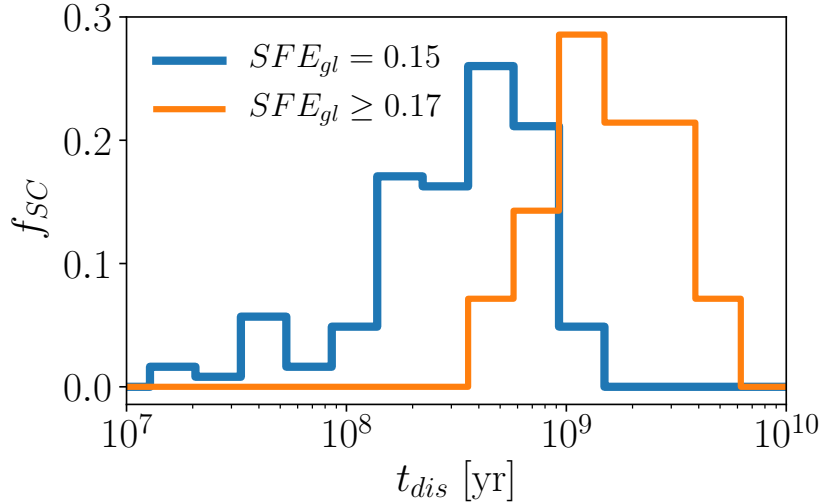


Figure 20: Histogram of model clusters by dissolution times for low-SFE and high-SFE clusters (blue and orange lines, respectively). The area subtended by each histogram is unity.

neighborhood star clusters has been discussed in Lamers et al. (2005) and Piskunov et al. (2018).

The question whether the age distribution of low-SFE clusters will change if we continue our simulations towards massive clusters sounds reasonable. We should remind the reader that since the initial cluster mass function is a power-law function with an index of “-2” the number of massive clusters is quite low. If we take into account that to produce a low-SFE cluster as massive as $10^6 M_\odot$ we will need a molecular clump with a mass of $10^8 M_\odot$. That is because the “initial” mass of such cluster is only about 1% ($F_b SFE_{gl} = 0.07 \times 0.15$) of the total mass of the star-forming clump. This lowers the number of possible very massive low-SFE clusters in cluster census of the Galaxy, because the mass function of molecular clumps is also a power-law with an index of -2. Additionally, according to Rahner et al. (2017) the higher the mass of star-forming clump the higher the SFE it requires to be destroyed by newly formed star cluster. Otherwise, the re-collapse of the gaseous shell could happen and produce more stars enhancing the SFE (Rahner et al., 2018). Therefore the distribution presented in Fig. 20 should not dramatically change if we consider more massive low-mass clusters.

An interesting trend emerges when we consider $SFE_{gl} = 0.15$ models in Fig. 19. If we ignore the low-mass end ($\leq 10^3 M_\odot$, i.e. the mass range for which the cluster sample is incomplete in most extra-galactic studies) and if we take into account that, in extra-galactic observations, the masses of young clusters can be over-estimated due to the contribution of an envelope of unbound stars (i.e. the cluster “initial” mass has to be defined as our extended mass, M_{2J}), an apparent MID mode may be emerging. For initial mass M_{2J} between 10^3 and $10^4 M_\odot$ low-SFE clusters actually show similar mean (and median) dissolution times, with even increasing standard deviations. On top of that, if we consider model clusters formed with very low $SFE_{gl} < 0.15$, which do not survive instantaneous gas expulsion and the resulting violent relaxation ($t_{dis} < 30$ Myr), but still observable as young clusters, then the effect of an apparent MID can be further strengthened.

However, since we do not cover that large a range of cluster masses and do not have that high a number of random realizations for good statis-

tics (especially at high-mass), we cannot argue firmly in favor of a mass-independent dissolution relation for low-SFE star clusters. Here, we stress that with a mean bound fraction at the end of violent relaxation of $F_{\text{bound}} = 0.07$, to model a star cluster with an “initial” mass $> 10^4 M_{\odot}$ and which formed with $\text{SFE}_{\text{gl}} = 0.15$, requires a birth mass of at least $10^5 M_{\odot}$. We are currently expanding our sample for $M_{\star} = 10^5 M_{\odot}$, for which we have one single fully dissolved model at the moment (purple open circle in Fig. 19). Nevertheless, we can firmly say that we have found a large scatter in the relation between the cluster “initial” masses and the cluster dissolution times for low-SFE clusters and for a given birth mass. This scatter results from the massive-star driven stochastic effects taking place during violent relaxation. Such effects yield, for a given birth mass and given $\text{SFE}_{\text{gl}} = 0.15$, different density profiles (hence different degrees of cluster compactness) and different bound fractions at the end of violent relaxation (hence different cluster “initial” masses).

In summary so far we have found that clusters formed with a high SFE_{gl} (> 0.15) dissolve in an MDD regime. Clusters formed with a low SFE_{gl} ($= 0.15$) also dissolve in an MDD regime, albeit with a significant scatter. Their dissolution time is comparable to that observationally inferred by Lamers et al. (2005). There is a strong mass-dependent upper limit to the cluster dissolution time, which means that, for a given environment, low-mass clusters cannot live as long as their high-mass *compact* counterparts. However, some high-mass clusters can dissolve as quickly as low-mass ones in the same environment.

4.4.2 Cluster life expectancy and cluster central density

Investigating further the parameters of our model clusters we have found a correlation between the cluster dissolution time, t_{dis} , and the Roche volume filling factor measured at the end of violent relaxation, although with significant scatter (Fig. 21). The Roche volume filling factor is defined as the half-mass to Jacobi radius ratio, and the half-mass radius refers to the Jacobi mass or the extended mass (left and right panels of Fig. 21, respectively). The filling factors are calculated at $t = 30$ and 70 Myr in top and bottom panels as in Fig. 18. The color-coding depicts the Jacobi mass, M_{J} (left panels) and the extended mass, $M_{2\text{J}}$ (right panels) indicated by the common color-bar at the right-hand-side. Note that the color coding is different from Fig. 18 where it refers to the birth mass of clusters. The shapes of markers still show the global SFEs. With gray arrows we indicate those $M_{\star} = 15000 M_{\odot}$ clusters presented in Figs. 14 and 15, namely from right-to-left, two random realizations of the $\text{SFE}_{\text{gl}} = 0.15$ model (open circles) and one random realization of $\text{SFE}_{\text{gl}} = 0.25$ model (open triangle). The indicated model clusters here are in the reverse order to that of the order of panels in Fig. 14.

The correlation is such that for a given “initial” mass, the higher the filling factor, the shorter the dissolution time, as found in Ernst et al. (2015). However, a comparison between our results and those of Ernst et al. (2015) is not fully self-consistent. Firstly, our model clusters are still expanding and have not returned to virial equilibrium yet when they over-fill their Roche volume. In contrast, model clusters of Ernst et al. (2015) are initially in virial equilibrium while overfilling their Roche volume. Secondly, our star clusters can present different density profiles (shallow or steep, with extended or compact core) after violent relaxation, therefore the Roche volume filling factor, as defined here, cannot characterize them universally.

We also find a correlation between the cluster life expectancy, t_{dis} , and the volume density contrast between cluster center and outskirts, defined

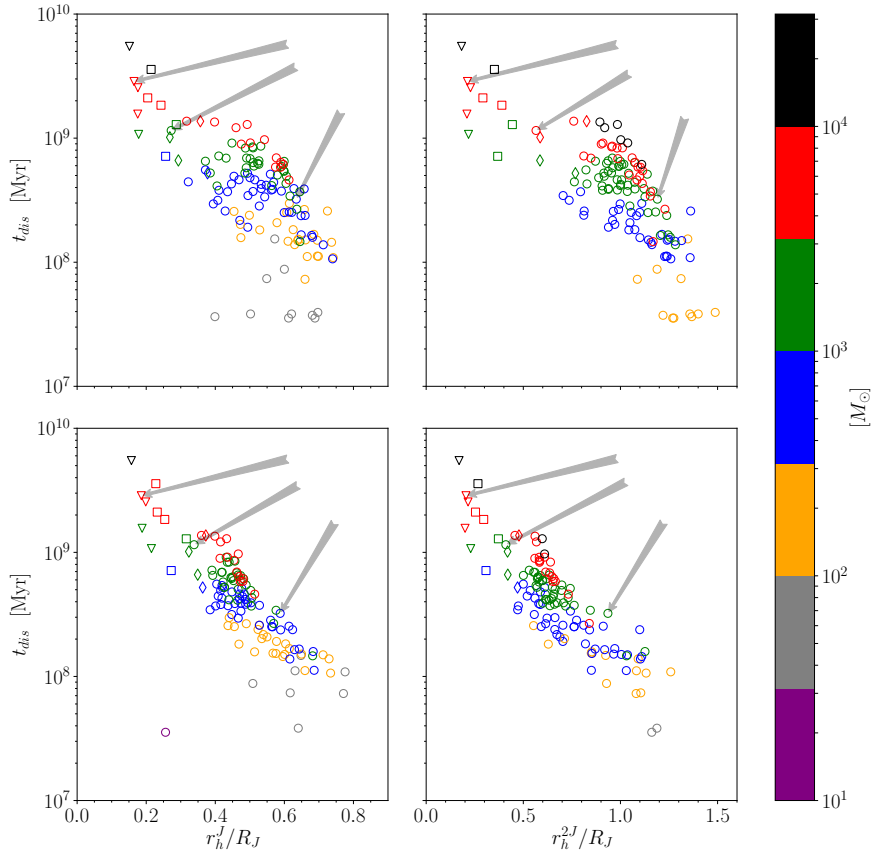


Figure 21: Cluster dissolution time as a function of Roche volume filling factor at $t = 30$ and $t = 70$ Myr (top and bottom panels, respectively). In the left panels, the cluster initial mass is estimated as the Jacobi mass, M_J , while in the right panels it is estimated as the extended mass, M_{2J} . Cluster initial masses are shown by the color-coding presented on the right-hand-side color-bar. The half-mass radius, r_h , is measured as the radius containing half of the cluster initial mass and marked as r_h^J when $M_{\text{init}} = M_J$ and r_h^{2J} when $M_{\text{init}} = M_{2J}$. The gray arrows indicate those $M_\star = 15k M_\odot$ model clusters presented in Figs. 14 and 15.

as the central volume density, ρ_c , to the volume density at Jacobi radius, ρ_J , ratio:

$$\rho_c/\rho_J = \frac{\rho(r=0)}{\rho(r=R_J)}. \quad (33)$$

This is shown in upper left panel of Fig. 22 as measured at the end of violent relaxation ($t = 30$ Myr). The smaller the density contrast, the faster the cluster dissolves and vice versa. The correlation is the tightest if we consider the density contrast of slightly more evolved clusters ($t = 70$ Myr, top right panel of Fig. 22), when the envelope at $R_J < r < 2R_J$ has been cleaned up of most of its stars. The color-coding corresponds to the Jacobi mass at the

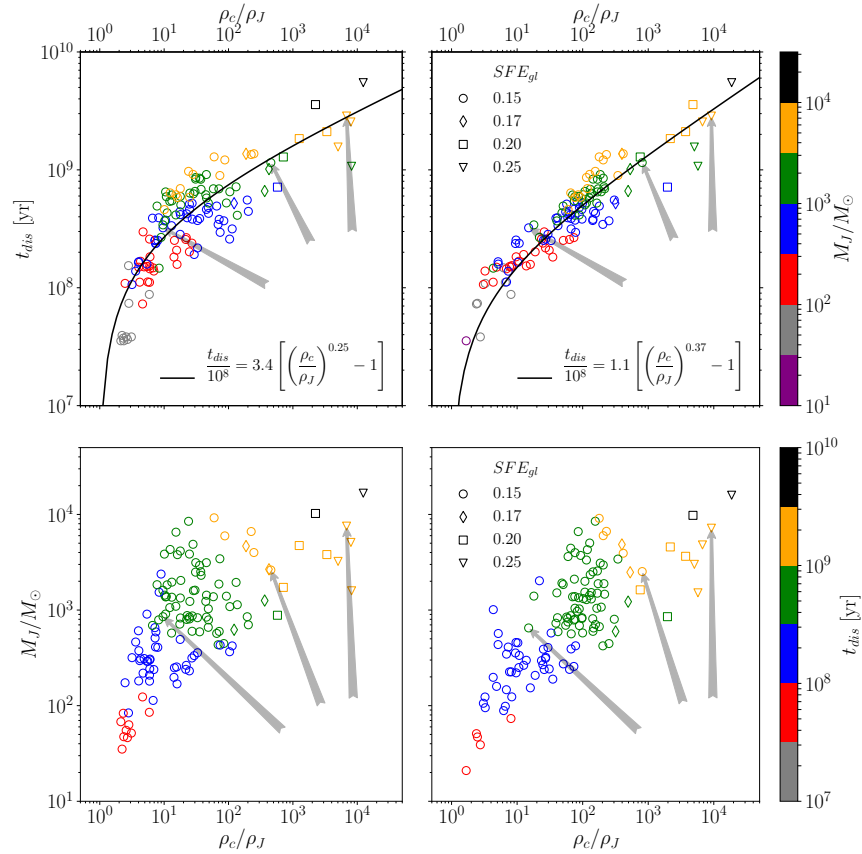


Figure 22: Cluster dissolution time, t_{dis} (top panels) and cluster Jacobi mass, M_J (bottom panels), as functions of volume density contrast between cluster center and outskirts, ρ_c/ρ_J (Eq. 33) measured at $t = 30$ Myr and $t = 70$ Myr (left and right panels, respectively). Unlike in Fig. 18 the color-coding refers to the cluster Jacobi mass at quoted ages in top panels, and to the cluster dissolution time in bottom panels. The best fits (Eq. 34-35) are shown with black curves. The three $M_\star = 15000M_\odot$ model clusters presented in Fig. 14 and Fig. 15 are indicated with the arrows in each panel in the same order, i.e. from left to right, as the corresponding panels of Fig. 14 and Fig. 15.

corresponding ages. The best fits, in the form of

$$t_{dis} = 3.4 \left[\left(\frac{\rho_c}{\rho_J} \right)^{0.25} - 1 \right] \times 10^8 \text{ yr} \quad (34)$$

and

$$t_{\text{dis}} = 1.1 \left[\left(\frac{\rho_c}{\rho_J} \right)^{0.37} - 1 \right] \times 10^8 \text{ yr}, \quad (35)$$

are shown with black curves in the top left and top right panels respectively. For high density contrast ($\rho_c/\rho_J > 10^3$) clusters in the top panels of Fig. 22 we can see nice patterns showing that their dissolution times are mass-dependent, which is again consistent with earlier studies of dissolution of Roche Volume filling or under-filling clusters.

When a cluster has a shallow density profile, the shrinking of its Jacobi radius due to cluster mass-loss (e.g. stellar evolution, tidal stripping, etc.) will leave outside the new Jacobi radius a number of stars higher than in case of a steeper density profile. Such clusters therefore dissolve more quickly than those with a steep density profile. Alternatively, if a cluster has developed a large core, comparable to the Roche volume, this also leads to the total destruction of the cluster. Such clusters are located at the very left of the top panels in Fig. 22, with low density contrasts and therefore short lifetimes.

In order to see better the correlation between these three parameters, ρ_c/ρ_J , t_{dis} and M_J , we swapped the dissolution time for the Jacobi mass in the bottom panels. The bottom panels of Fig. 22 show the Jacobi mass, M_J , as a function of the density contrast, ρ_c/ρ_J , color-coded by the dissolution time, t_{dis} . As it is seen now clearly here with more or less nice pattern the dissolution time depends on both “initial” mass and density contrast, wherein short dissolution time of massive clusters are explained by their low density contrast (low concentration) and vice versa. This is also consistent with other theoretical works, where the evolution of globular clusters with initially low concentration has been discussed (see e.g. Fukushige and Heggie (1995), Takahashi and Portegies Zwart (2000) and Vesperini and Zepf (2003))

As we see from the foregoing results, when studying the long-term secular evolution of star clusters it is worth estimating their “initial” mass at $t = 70$ Myr after gas expulsion in order not to be biased by the processes taking place during violent relaxation. The latter is very different from the subsequent long-term evolution of star clusters. As we showed in Shukirgaliyev et al. (2017), clusters formed with very low global SFE (< 0.15) dissolve during violent relaxation, and their dissolution time is independent of their birth mass.

We remind the reader that we have modeled the clusters in a given tidal-field environment (i.e. star clusters have the same mean density at the time of instantaneous gas expulsion), and that they have the same stellar density profile at the time of instantaneous gas expulsion. All relations we have found could thus be affected if birth conditions are different. Star clusters which at the time of gas expulsion are more compact or more diffuse than our models may have evolutionary tracks different from those analyzed here, forming denser or more diffuse bound clusters after violent relaxation.

4.5 DISCUSSIONS AND CONCLUSIONS

We have performed a large set of direct N-body simulations of the evolution of star clusters in the solar neighborhood starting from their birth in molecular clumps until complete dissolution in the Galactic tidal field. We have not considered any hydro-dynamical simulations to account for the formation of our model embedded clusters. Instead we have used a semi-analytical approach – the local-density-driven cluster formation model of Parmentier and Pfalzner (2013), and assumed instantaneous gas expulsion. The modeling of the evolution of our clusters therefore covers the time-span from their

formation to complete dissolution. As a result, our model clusters bear the information about their formation conditions and their violent relaxation all through their evolution, even for dissolution times longer than 1 Gyr.

We have found that model clusters with $SFE_{gl} = 0.15$ present a significant stochasticity during the expansion phase. That is, initially almost identical clusters can follow very different tracks in terms of bound mass fraction, structure and dissolution time. At the end of violent relaxation these clusters retain quite a small bound mass fraction, with relatively large scatter, $F_{bound} = 0.07 \pm 0.04$. The bound mass fraction F_{bound} does not depend on the cluster birth mass (see Fig. 16 for $SFE_{gl} = 0.15$ models or column (5) in Table 7) and the scatter persists even for a number of stars as high as $N_{\star} \approx 174k$. The reason could be in the relatively high virial ratio of low-SFE clusters ($Q \sim 1.55$), combined with Poisson noise in the phase-space distribution of stars at the time of gas expulsion and with the stochasticity characterizing the expansion phase due to the relatively small number of massive stars staying bound to the cluster surviving core.

To be consistent with the other works where the violent relaxation is neglected we introduce the cluster “initial” mass as its mass at the end of violent relaxation, when the cluster stops to lose mass violently due to gas removal. In the scope of this study we have provided two cluster “initial” mass estimates, the Jacobi mass and the “extended” mass. The Jacobi mass is the stellar mass within one Jacobi radius, R_J , while the extended mass is the stellar mass within two Jacobi radii, $2R_J$. We have estimated the latter, because escaping stars form an envelope around their natal cluster, which stays in the cluster surroundings for a few tens of Myrs (see Fig. 14). Such an envelope possibly contributes to the mass estimate of extra-galactic young star clusters, where the membership analysis is impossible and the measurement of the tidal radius is not straightforward.

From our simulations we have found that star clusters formed with a high global SFE (≥ 0.20) dissolve in a tight mass-dependent regime ($t_{dis} \propto M_{init}^{0.7}$), in agreement with earlier works (Fig. 18). In the solar neighborhood, these clusters dissolve in a way similar to the empirical relation of Boutloukos and Lamers (2003), with a dissolution time for a $10^4 M_{\odot}$ cluster of $t_4^{dis} = 3.8$ Gyr. This is almost a factor of two shorter than the estimate of Baumgardt and Makino (2003) ($t_4^{dis} = 6.9$ Gyr), but, still longer than that given in Lamers et al. (2005) ($t_4^{dis} = 1.3 \pm 0.5$ Gyr).

In contrast, model clusters formed with $SFE_{gl} = 0.15$ dissolve more quickly than high SFE clusters ($t_4^{dis} \sim 1.3$ Gyr), present a shallower MDD relation ($t_{dis} \propto M_{init}^{0.5}$), and their dissolution time is affected by a relatively large scatter. That is, variations of the bound mass fraction at the end of violent relaxation (due to the stochastic impact of the massive stars described above) can modify sensitively the cluster dissolution time. The lower the bound mass fraction, the shorter the dissolution time (Fig. 17). We have found that some of our $SFE_{gl} = 0.15$ model clusters can dissolve within 100-200 Myr, while the high-SFE clusters with the same “initial” mass can live longer than a Gyr (e.g. consider the vertical bin embracing a cluster mass range from $2 \times 10^3 M_{\odot}$ to $4 \times 10^3 M_{\odot}$ in the right panels of Fig. 18).

Nevertheless, taken all together, our model clusters follow an MDD relation, albeit with a relatively large scatter. The relation between the dissolution time and cluster initial mass becomes close to that observationally found by Lamers et al. (2005) for the solar neighborhood if the cluster population is dominated by low-SFE ($SFE_{gl} = 0.15$) clusters. Such an assumption is a real possibility for the solar neighborhood since nearby embedded clusters usually show low SFEs. Therefore, in this study, we propose an alternative way to decrease the cluster dissolution time for the solar neighborhood found by Lamers et al. (2005) to that proposed by Gieles et al. (2006). While

Gieles et al. (2006) propose that cluster dissolution time inferred from observations by Lamers et al. (2005) is shorter than the prediction of Baumgardt and Makino (2003) due to the additional destructive processes associated to GMC encounters, we propose here that the difference between theory and observations can be removed once one takes into account diffuse weakly bound star clusters, arising from low $SFE_{gl} = 0.15$.

The distribution of the dissolution times of high-SFE ($SFE_{gl} \geq 0.17$) and low-SFE ($SFE_{gl} = 0.15$) clusters is provided in Fig. 20. It shows that our low-SFE clusters usually dissolve within 1 Gyr and our high-SFE clusters, in contrast, usually survive beyond a Gyr.

If we consider our low-SFE clusters only, estimate their initial mass as the extended mass at $t = 70$ Myr and neglect the low-mass end, as for extra-galactic observations for which the unbound envelope-stars usually contribute to the cluster mass and the low mass clusters often remain undetectable, an interesting apparent MID relation can emerge (see the flat part of red curve with $10^3 M_{\odot} < M_{2J} < 10^4 M_{\odot}$ in Fig. 19). But since our simulations do not cover that high a range of cluster “initial” masses, we cannot firmly argue about MID based on our current data-set.

We have found a correlation between the cluster life expectancy and the volume density contrast between cluster center and outskirts (top panels of Fig. 22). The higher the density contrast, the longer the cluster lives. We have found that they also correlate with cluster initial mass, which is shown with nice patterns in the bottom panels of Fig. 22.

All correlations found in this paper are tighter if we consider them at the age of $t = 70$ Myr rather than at $t = 30$ Myr. Therefore, we propose that for cluster lifetime studies, it is more appropriate to measure cluster “initial” parameters as mass, central density and structure about 70 Myr after gas expulsion, when star clusters have mostly re-virialized and are cleaned up from their expanding stellar envelope.

So we summarize that low-mass clusters are unable to live for as long as their high-mass counterparts. However, high-mass clusters can easily dissolve on a short time, if formed with a small SFE, but still outlive most of their low-mass counterparts. Overall, our model clusters dissolve in a mass-dependent regime, although with different dissolution times for low- and high-SFE models. For low-SFE ($SFE_{gl} = 0.15$), an apparent MID mode can emerge if we define the extended mass as the initial mass of clusters and if we restrict our attention to clusters more massive than $10^3 M_{\odot}$, as is after the case in extra-galactic studies with a dissolution time less than 1 Gyr.

THE TIDAL FIELD IMPACT ON CLUSTER SURVIVABILITY

This Chapter was submitted for publication to MNRAS as Shukirgaliyev, B., G. Parmentier, A. Just, and P. Berczik (2018). “The star cluster survivability after gas expulsion is independent of the Galactic tidal field impact”. B. Shukirgaliyev performed all N-body simulations, analyzed their outputs and wrote most of the text. All authors contributed ideas, comments and suggestions throughout the realization of this study and its preparation as a peer-reviewed paper.

5.1 INTRODUCTION

In Chapter 3, we studied the survivability of star clusters after instantaneous gas expulsion, assuming that clusters form according to the local-density-driven cluster formation model of Parmentier and Pfalzner (2013). We reported in Shukirgaliyev et al. (2017) that our model star clusters which form with a centrally peaked SFE profile are more resilient to instantaneous gas expulsion than earlier models (e.g. Baumgardt and Kroupa, 2007, and references therein). That is, our model clusters survive instantaneous gas expulsion with a critical global SFE of $SFE_{gl} = 0.13$ instead of $SFE_{gl} = 0.33$ as estimated previously. However, Shukirgaliyev et al. (2017) is not the only work which decreased the critical SFE for cluster survivability after instantaneous gas expulsion. Smith et al. (2013) considered instantaneous gas expulsion in hierarchically formed star clusters within different arbitrary external potentials mimicking the residual gas. Farias et al. (2018) also considered clusters with fractal distributions and tried to link the initial conditions at the time of gas expulsion to the preceding star-formation phase using hydrodynamical simulations. But both papers considered isolated clusters and did not take into account the impact of the tidal field. The advantages of our models are that the potential of the residual gas is justified by a semi-analytical cluster-formation model, and the tidal stripping by the Milky-Way-like galaxy is taken into account. The latter results in a final bound fraction lower than if clusters were isolated.

We studied mostly the violent relaxation phase of cluster evolution in Chapter 3. By violent relaxation we mean here the evolution of star clusters from the dynamical state of non-equilibrium induced by instantaneous gas expulsion into a new state of quasi-equilibrium. In other words, since our clusters are super-virial after gas expulsion – being assumed to be in virial equilibrium with the gas potential – the violent relaxation is also associated with a rapid cluster mass loss in response to gas expulsion. When violent relaxation ends, clusters stop losing their mass in response to gas expulsion and other mass loss mechanisms (e.g. stellar evolution, tidal stripping) come into play. The end of violent relaxation is the starting point of the long term evolution of star clusters which have survived instantaneous gas expulsion. In Chapter 4 investigating the long-term evolution of our model star clusters we showed that both the cluster formation conditions and the violent relaxation phase influence significantly the subsequent long-term evolution/dissolution of the clusters. That is, the dissolution time of low-SFE ($SFE_{gl} = 0.15$) clusters is shorter than that of high-SFE ($SFE_{gl} > 0.15$), even when considering clusters with equal masses at the end of violent relaxation. Generally, the results presented in Chapter 4 confirm the mass dependent

dissolution of clusters, which have survived their violent relaxation. The relation for low-SFE clusters (see Fig. 18 in Chapter 4), however, present a large scatter and, possibly, a mass independent trend for clusters more massive than $10^3 M_{\odot}$. In contrast to the long-term evolution, the evolution of star clusters is mass independent during the violent relaxation.

Controversial results have been presented by observers regarding the dependence of the cluster dissolution time on the cluster mass and environment (see Lamers, 2009; Whitmore, 2017, for an overview). One group of observers reported that star cluster dissolution depends on the cluster initial mass and cluster environment, i.e. the cluster dissolution time is longer for higher masses and weaker tidal field of the host galaxy (Bastian et al., 2012; Boutloukos and Lamers, 2003; Lamers, Gieles, and Portegies Zwart, 2005). However, Chandar, Fall, and Whitmore (2010), Chandar et al. (2014), Fall, Chandar, and Whitmore (2009), and Whitmore, Chandar, and Fall (2007) reported from their extragalactic observations that star clusters dissolve independently of their mass and of their environment.

In 2015, the Legacy Extragalactic UV Survey (LEGUS) collaboration started its work to investigate the connection between environmental conditions in galaxies and their cluster populations (Calzetti et al., 2015). One of the aims of the LEGUS collaboration is to investigate the influence of the environment on the cluster evolution/dissolution in nearby galaxies. The most recent paper from the LEGUS collaboration (Messa et al., 2018) studies the cluster population of the M51 galaxy as a function of galactocentric distance, and location with respect to the spiral arms (i.e spiral arms and inter-arm regions). Considering the clusters younger than 200 Myr they conclude that the shape of the cluster mass function does not change with galactocentric distance and is described by a power law with a slope close to -2 . The cluster age distribution, however, depends on both galactocentric distance and ambient density, showing evidence for faster cluster disruption in the inner and denser regions than in the outer and diffuse (inter arm) ones, under the assumption of a constant rate of cluster formation. Clusters younger than 10 Myr were not accounted in the age distribution function because their census is contaminated by quickly dissolving unbound clusters.

From a theoretical point of view, numerous works have studied the impact of the tidal field on the cluster evolution/dissolution using N-body simulations (e.g. Baumgardt and Makino, 2003; Ernst et al., 2015; Fukushige and Heggie, 1995; Renaud et al., 2008; Rossi, Bekki, and Hurley, 2016; Spurzem et al., 2005; Tanikawa and Fukushige, 2005, among others). All these studies show that the impact of the tidal field is significant – the stronger the tidal field, the quicker the cluster dissolves. However, all these works have considered the long-term evolution of star clusters, starting from them being in virial equilibrium. That is, the violent relaxation is neglected, or assumed to be over.

Theoretical works considering the violent relaxation, which precedes the re-virialization of star clusters and their long-term evolution, usually neglect the impact of the tidal field of the host galaxy. Only a few papers in the literature have considered the effect of the tidal field on the cluster early evolution and survivability after gas expulsion in their N-body simulations: Baumgardt and Kroupa (2007), Goodwin (1997), and Kroupa, Aarseth, and Hurley (2001). Baumgardt and Kroupa (2007) are the only ones who mapped the parameter space of global SFE, gas expulsion time-scale and tidal field impact in a comprehensive way. They reported that the impact of the tidal field on the cluster survivability is significant. They considered cluster Plummer models with a radially constant SFE (thus implying that only clusters whose SFE is larger than at least 0.33 survive instantaneous gas expulsion) and a spherically symmetric Galactic gravitational potential.

The impact of the tidal field is usually characterized by the ratio of the cluster half-mass radius to the Jacobi (tidal) radius, r_h/R_J . The tidal field is stronger when a cluster orbits nearer the Galactic center, and is weaker for a larger Galactocentric distance, R_{orb} . That is, for a given cluster mass, the Jacobi radius increases with Galactocentric distance and, therefore, r_h/R_J decreases for a fixed cluster size. Instead of changing the Galactocentric distance one can also modify the cluster size (e.g. the half-mass radius) only and thus change r_h/R_J while the Jacobi radius stays constant for given mass and Galactocentric distance. In that case, the tidal field impact is weaker for a compact cluster (small r_h) and stronger for a diffuse cluster (large r_h).

In Chapter 3, we also investigated the impact of the tidal field by varying the size of clusters on a given orbit and found that it is not significant within the uncertainty¹ of 10% on the bound mass fraction retained by star clusters at the end of their violent relaxation. However, only a small number of simulations were performed to study the impact of tidal field and we were limited to only two different birth masses and 3 random realizations per model. Therefore in this Chapter, we expand our previous results and we study the impact of the tidal field in a more comprehensive way, also varying the cluster Galactocentric distance R_{orb} . This will be helpful for us to understand and interpret extragalactic observations and also to compare the models with the observed reality of the Universe.

5.2 PARAMETER SPACE COVERED BY OUR GRID OF SIMULATIONS

In previous chapters 3 and 4, we considered the evolution of clusters after instantaneous gas expulsion for different global SFEs ($\text{SFE}_{\text{gl}} = [0.1, 0.25]$) and different cluster birth masses $M_\star = [3\text{k}, 100\text{k}] M_\odot$ (equivalent to a number of stars $N_\star \approx [5 \times 10^3, 1.7 \times 10^5]$). We studied both their violent relaxation and their long-term evolution till their final dissolution in the Galactic tidal field. All our model clusters have circular orbits in the Galactic disk plane at the Galactocentric distance of $R_{\text{orb}} = 8$ kpc. They all have the same tidal field impact, $r_h/R_J = 0.052$, at the time of instantaneous gas expulsion.

Now we expand our set of N-body simulations and we study the impact of the tidal field on star cluster survivability after instantaneous gas expulsion. We consider our previous models with $r_h/R_J = 0.052$ as our ‘standard’ set of models, or ‘So-models’.

We limit ourselves to clusters that survive instantaneous gas expulsion (i.e. $\text{SFE}_{\text{gl}} \geq 0.15$), and we consider the efficiencies $\text{SFE}_{\text{gl}} = 0.15, 0.17, 0.20, 0.25$, and birth masses $M_\star = 3\text{k}, 6\text{k}, 10\text{k}, 15\text{k}, 30\text{k}, 60\text{k} M_\odot$. We do not consider any eccentric or inclined (with respect to the Galactic disk plane) orbits in this study.

In the scope of this paper we vary the impact of the tidal field, characterized by the ratio of the cluster half-mass radius to Jacobi (tidal) radius, r_h/R_J , in two ways with respect to our standard set of models:

- 1) We vary the Galactocentric distance R_{orb} of the model clusters while keeping constant their physical size (r_h) at the time of instantaneous gas expulsion. We have chosen 4 additional Galactocentric distances: $R_{\text{orb}} = 2.9, 4.64, 10.95$, and 18.0 kpc, which correspond to $r_h/R_J = 0.1, 0.075, 0.04$, and 0.03 . This completes our initial set of “standard” So-model clusters, i.e. $r_h/R_J = 0.052$ at $R_{\text{orb}} = 8.0$ kpc. We name the additional models as ‘extra Inner-’ (xI), ‘Inner-’ (I), ‘Outer-’ (O) and ‘extra Outer-’ (xO) orbit model clusters, respectively. In Fig. 23, which

¹ The uncertainty is a consequence of the randomization of the initial conditions of the N-body simulations.

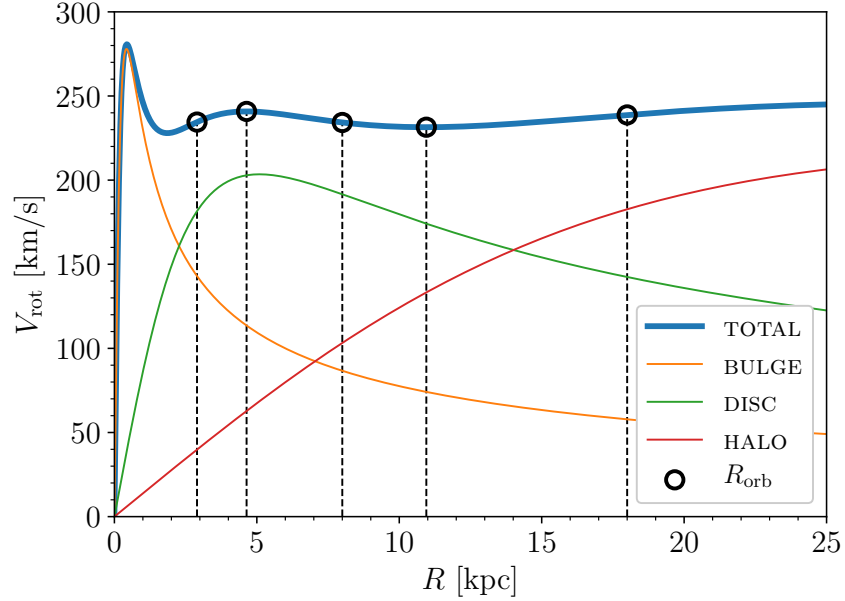


Figure 23: The rotation curve of the Galaxy model (thick blue line) and its corresponding components (bulge, disc and halo). The black open circles show the radii of the circular orbits on which we put our model clusters: $R_{\text{orb}} = 2.9, 4.64, 8.0, 10.95, 18.0$ kpc.

presents the rotation curve of the Galaxy model, their positions are indicated by black open circles.

- 2) We vary the physical size r_h of the ‘So-model’ clusters, while keeping them in the solar neighborhood ($R_{\text{orb}} = 8.0$ kpc). That is, we vary the cluster density. In this case, we expand the few simulations already performed in Chapter 3 for $r_h/R_J = 0.1, 0.075, 0.025$ and consider a larger range of birth masses and more random realizations per model. These models are named: ‘the most diffuse’ (or S+2, when $r_h/R_J = 0.1$), ‘the diffuse’ (or S+1, 0.075) and ‘the compact’ (or S–1, 0.025) model clusters.

The number of random realizations performed per model, where each model is described by a global SFE (SFE_{gl}), cluster birth mass M_* and tidal field impact r_h/R_J , are presented in Table 7.

5.3 THE VIOLENT RELAXATION DURATION

The impact of the tidal field on the cluster survivability can be quantified by the variations of the cluster bound mass fraction at the end of violent relaxation. We consider the cluster bound mass as the stellar mass enclosed inside one Jacobi radius at a given time, also called the Jacobi mass M_J . Although it has been discussed that there are stars beyond the Jacobi radius staying around the cluster for several mega-years (Just et al., 2009; Ross, Mennim, and Heggie, 1997), we decide to keep our definition of the bound mass as the Jacobi mass to avoid any overestimation.

Before proceeding any further, we have to clarify the definition of the violent relaxation and its duration, i.e the criteria used to determine the end of violent relaxation. This is important since we measure our final bound fraction at the end of violent relaxation.

Table 7: Number of random realizations performed for each model cluster, where each model is described by its birth mass (M_*), global SFE and tidal field impact (r_h/R_J).

M_*/M_\odot	SFE _{gl}	n_{rnd}							
		$r_h/R_J =$	0.100	0.100	0.075	0.070	0.050	0.040	0.030
		S+2	xI	I	S+1	So	O	xO	S-1
3000	0.15	15	15	16	15	26	16	15	15
3000	0.17	6	6	6	6	6	6	6	6
3000	0.20	6	6	6	6	6	6	6	6
3000	0.25	1	1	1	1	1	1	1	1
6000	0.15	10	10	11	10	36	11	10	10
6000	0.17	6	6	6	6	6	6	6	6
6000	0.20	8	8	6	8	8	6	8	8
6000	0.25	3	3	1	3	3	1	3	3
10000	0.15	11	11	11	11	36	11	11	11
10000	0.20					1			
10000	0.25					1			
15000	0.15	11	11	12	11	32	12	11	11
15000	0.17	6	6	6	6	6	6	6	6
15000	0.20	8	8	6	8	8	6	8	8
15000	0.25	3	3	1	3	3	1	3	3
30000	0.15	10	10	11	10	27	11	10	10
30000	0.17	6	6	6	6	6	6	6	6
30000	0.20	6	6	6	6	6	6	6	6
30000	0.25	1	1	1	1	1	1	1	1
60000	0.15		8	15		15	15		
60000	0.17			1		1	1		
60000	0.20			1		1	1		
60000	0.25			1		1	1		
100000	0.15					3			
300000	0.15					1			

By definition, violent relaxation is the dynamical evolution of a star cluster from a state of non-equilibrium into a new state of (quasi-)equilibrium (Lynden-Bell, 1967). Our model clusters become super-virial once the instantaneous gas expulsion has taken place, because they were in virial equilibrium with the total (gas+stars) gravitational potential. The violent relaxation, as a response to instantaneous gas expulsion in our case, starts immediately after gas expulsion and causes clusters to lose their mass rapidly (violently). This mass-loss should stop when the violent relaxations ends, that is, when the cluster has returned to virial-equilibrium, if it survived as a bound cluster.

In previous works, we assumed that the violent relaxation ends at an age of 20 Myr², when the bound mass fraction of all model clusters becomes more or less constant (see Fig. 3 of Chapter 3). We reported that the violent relaxation ends within 20 Myr independently of the global SFE and of the birth mass of star clusters for a given tidal field impact. However, varying the cluster size r_h , hence the impact of the tidal field r_h/R_J , influences the violent relaxation duration. The violent relaxation ends earlier for a denser cluster than for a diffuse one, but the time difference does not correlate with the crossing time of star clusters (i.e. it does not scale with $\sqrt{r_h^3}$, see Chapter 3 or consider the upcoming Fig. 28 at the end of this section).

The evolution of the bound mass fraction for a $M_* = 30k M_\odot$ cluster with a low SFE (left panels) and a high SFE (right panels), and for different half-mass radii r_h at $R_{orb} = 8kpc$, is shown in the top panels of Fig. 24. In this case, the tidal field impact r_h/R_J varies because of the variation of r_h .

Now in the bottom panels of Fig. 24, we place our ‘standard’ So-model clusters at different Galactocentric distances R_{orb} . We can see that the violent relaxation, as a rapid mass loss in response to instantaneous gas expulsion, ends within different time-spans depending on the tidal environment (the different colors correspond to different Galactocentric distances). We now need to define the end of the violent relaxation, since this is the time at which we need to measure the bound fraction to assess the cluster survivability after gas expulsion when varying the tidal field impact.

Since our model clusters are not isolated, but evolve in the tidal field of the Galaxy, and consist of evolving stars, different mass-loss mechanisms are involved during the evolution after gas expulsion. They are: stellar evolutionary mass loss, rapid (violent) mass loss in response to gas expulsion, and on the long-term, mass-loss through the two-body relaxation (evaporation) and long-term mass loss due to the tidal stripping. The cluster evaporation through two-body relaxation is the least efficient mass-loss mechanism among those considered here. The stellar evolutionary mass loss is quite significant and cause the clusters to lose their mass within the first hundred mega-years, due to the quick evolution of massive and intermediate mass stars. It is especially high within the first 3-4 Myr after the cluster formation. Stellar evolutionary mass-losses become less significant at a later time because low-mass stars evolve (read: lose their mass) more slowly.

The rapid (violent) mass loss of star clusters in response to gas expulsion is very significant and happens in the very beginning of the cluster evolution after gas expulsion while it is expanding. This type of cluster mass loss highly depends on the SFE, the dynamical state of the cluster immediately before gas expulsion, the gas expulsion time-scale, and the spatial distribution of stars and gas relative to each other (Baumgardt and Kroupa, 2007; Brinkmann et al., 2017; Goodwin, 2009; Shukirgaliyev et al., 2017; Smith et al., 2013; Verschueren and David, 1989, among others).

² i.e. 20 Myr after the instantaneous gas expulsion

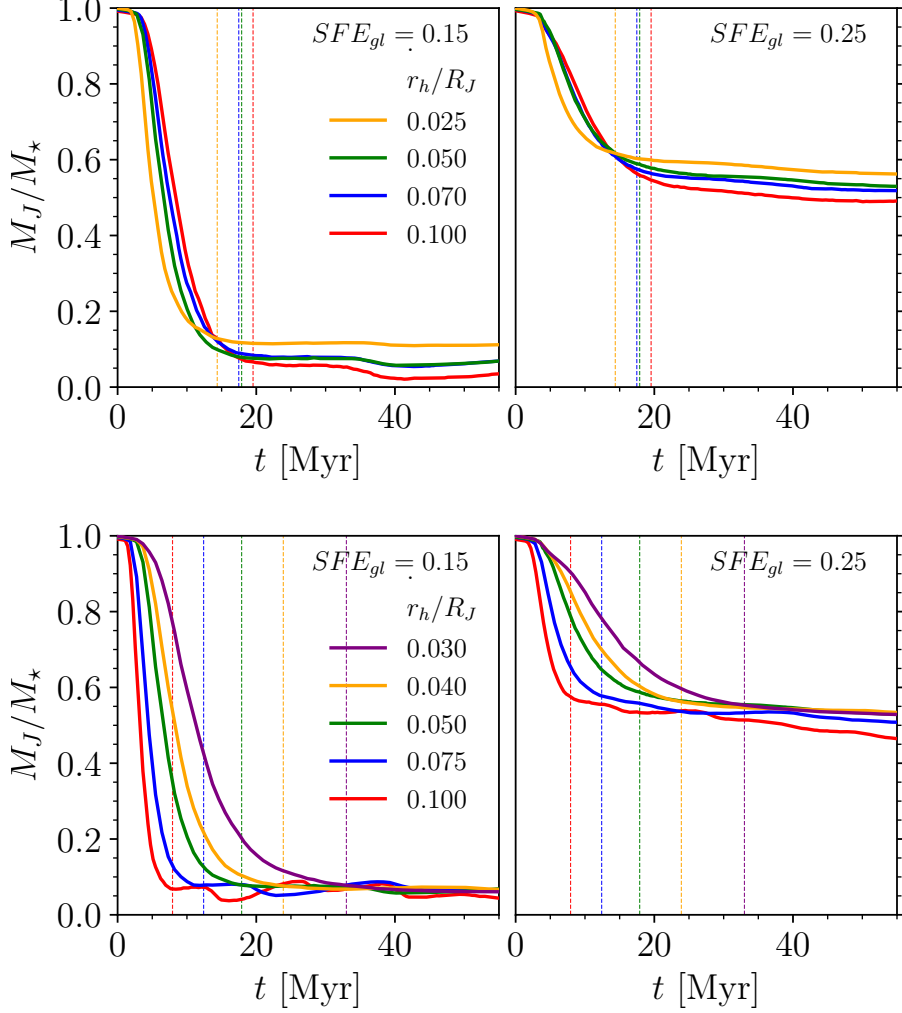


Figure 24: The bound mass fraction evolution of $M_* = 30k M_\odot$ clusters for different tidal field impacts. The top panels present the solar neighborhood clusters ($R_{\text{orb}} = 8$ kpc) where the tidal field impact r_h/R_J varies with cluster size r_h (i.e. different mean densities) at the time of instantaneous gas expulsion. The bottom panels show clusters of identical size, but placed at different Galactocentric distances. Therefore the tidal field impact r_h/R_J varies with the Jacobi radius R_J . Left and right panels show the low-SFE (i.e. $SFE_{gl} = 0.15$) and high-SFE (i.e. $SFE_{gl} = 0.25$) clusters, respectively. The thin vertical dashed lines indicate the end of violent relaxation, which we obtain in this section and whose values are provided in Table 8.

The tidal stripping would be another long-term mass-loss mechanism which would not be highly significant at the beginning of cluster evolution if our model clusters remained in virial-equilibrium. But as we mentioned before, our model clusters expand after gas expulsion and lose their mass rapidly. Here the tidal stripping comes in combination with rapid mass loss and cut out those stars which went beyond the Jacobi radius. We note that these “far traveled stars” would be bound to the cluster if the latter were isolated. Once the violent relaxation is over, that is, the cluster is not expanding any more, the mass-loss due to the tidal stripping becomes negligibly small compared to stellar evolutionary mass-losses.

Therefore, we assume that the violent relaxation ends when the cluster mass-loss rate is equal to, or less than the stellar evolutionary mass losses.

In top panels of Fig. 25 we present the evolution with time of the characteristic mass loss time-scale of star clusters, defined as the inverse of the cluster mass loss rate normalized to the cluster birth mass:

$$\tau = \frac{1}{\frac{dM_{\text{J}}/M_{\star}}{dt}} = -\frac{M_{\star}}{\dot{M}_{\text{J}}}. \quad (36)$$

We show here as an example only clusters at two Galactocentric distances, $R_{\text{orb}} = 2.9$ kpc and $R_{\text{orb}} = 18.0$ kpc in the left and right panels of Fig. 25, respectively. In the bottom panels of Fig. 25 the corresponding bound mass fraction evolutions are presented. The different colors correspond to different global SFEs (red, blue, green and yellow for $\text{SFE}_{\text{gl}} = 0.15, 0.17, 0.20$ and 0.25 , respectively). The red thick curve in the top panels shows the median value of the characteristic mass-loss times of all model clusters for a given environment (i.e. R_{orb}). The black dashed line in the bottom panels depicts stellar evolutionary mass-loss. The stellar evolutionary mass-loss time-scales as defined by Eq. 36 for two $M_{\star} = 10^5 M_{\odot}$ cluster models are shown with black dots in top panels. The thin solid black curve corresponds to the best fit to the stellar evolutionary mass loss characteristic time within the time interval from 4 Myr to 100 Myr:

$$\tau_{\text{STEV}} = -\frac{M_{\star}}{\dot{M}_{\text{STEV}}} = 17.8 (t - 2)^{1.06} \quad [\text{Myr}]. \quad (37)$$

Lamers et al. (2005) already provided some approximation, which describes the stellar evolutionary mass loss fraction of their model clusters for ages $t > 12.5$ Myr with an accuracy of a few per cent. However, we need an expression of the stellar evolutionary mass-loss which is valid also at younger ages. Additionally, we use the IMF Kroupa (2001), instead of the IMF of Salpeter (1955) as Lamers et al. (2005) did. Therefore, we fit our own approximation (Eq. 37), which provides an excellent fit for all ages younger than 100 Myr.

The stellar evolutionary mass loss rate normalized to the cluster birth mass is the same for any cluster mass, except for a large background noise in the case of low-mass clusters. Therefore, we decide to compare the characteristic times τ (Eq. 36) of all models with the fit function for stellar evolution provided in Eq. 37. That is, we identify the time when the characteristic mass-loss time of model clusters becomes longer than the fit function. We then take the average over all model clusters of a given tidal field impact and define it as the end of violent relaxation. This average t_{VR} is indicated by the vertical dashed lines in each panel of Fig 25, where the shaded area corresponds to the standard deviation. The numerical values are provided in Table 8.

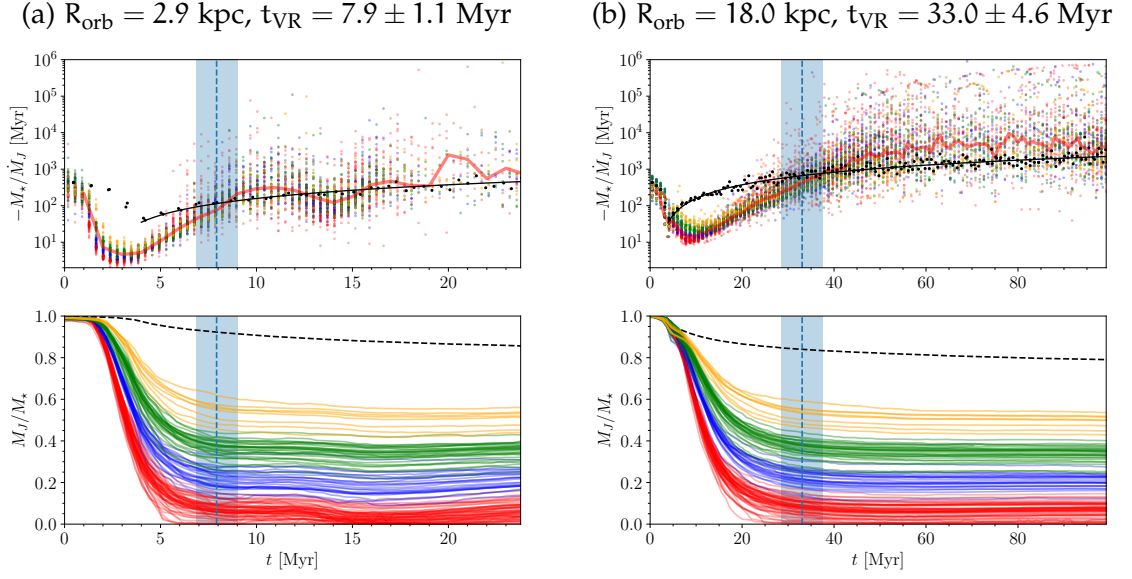


Figure 25: The characteristic mass-loss time (top panels) and the bound mass fraction evolution (bottom panels) of star clusters at two Galactocentric distances $R_{\text{orb}} = 2.9$ kpc and $R_{\text{orb}} = 18$ kpc are shown in left and right panels, respectively. The different colors correspond to cluster global SFEs in such a way that $\text{SFE}_{\text{gl}} = 0.15$ (red), 0.17 (blue), 0.20 (green), and 0.25 (yellow). The red thick line in upper panels corresponds to the median of all simulations at a given time (irrespective of global SFE and birth mass). The black dots show the characteristic mass-loss time of stellar evolution only and correspond to two simulations with $M_{\star} = 10^5 M_{\odot}$. The black solid line is the best fit to stellar evolutionary mass loss characteristic time. In bottom panels the black line shows the stellar evolutionary mass-loss of a $M_{\star} = 10^5 M_{\odot}$ cluster. In each panel the vertical blue dashed line corresponds to the end of violent relaxation, t_{VR} , with shaded area corresponding to the standard deviation (see the text for more explanations).

Table 8: End of violent relaxation for different tidal field impacts.

Model name	R_{orb} [kpc]	$r_{\text{h}}/R_{\text{J}}$	t_{VR} [Myr]
xI	2.9	0.100	7.9 ± 1.1
I	4.64	0.075	12.4 ± 2.3
O	10.95	0.040	23.9 ± 2.9
xO	18.0	0.030	33.0 ± 4.6
S+2	8.0	0.100	19.5 ± 3.2
S+1	8.0	0.070	17.5 ± 1.9
S0	8.0	0.050	17.9 ± 2.3
S-1	8.0	0.025	14.4 ± 1.7

5.3.1 Relation between the tidal field impact and the violent relaxation duration

Figure 26 shows the time of the end of violent relaxation, t_{VR} , as a function of the tidal field impact, r_h/R_J . The black cross at the center of the figure stands for our earlier estimate of the end of violent relaxation as measured by eye for ‘standard’ So-models in Chapter 3, while the green open circle indicates the generalized estimate of the end of violent relaxation based on the method described in previous subsection. As we can see from this figure, both results are consistent with each other. The cluster models of the solar neighborhood with different densities are indicated with crosses, while the model clusters with different Galactocentric distances are indicated with plus symbols (see the key).

The violent relaxation duration t_{VR} does not change significantly for the clusters with different densities but the same Galactocentric distance, while a change of more than 20 Myr shows up when considering different Galactocentric distances.

The violent relaxation duration, t_{VR} , correlates almost linearly with the Jacobi radius at the time of gas expulsion, when we consider identical clusters at different Galactocentric distances (Fig. 27). This means that the violent relaxation duration is proportional to the Jacobi radius, or rather to the cluster crossing time measured at the Jacobi radius:

$$t_{\text{VR}} \propto \frac{R_J}{V}. \quad (38)$$

Here V is the characteristic speed of the cluster stars, which is constant when we consider different galactocentric distances, because in that case we do not change any other physical parameters of clusters such as mass, size or velocity dispersion.

On the other hand, when we vary the impact of the tidal field for a fixed galactocentric distance (i.e. the Jacobi radius is fixed) by changing the cluster half-mass radius, we modify the cluster velocity dispersion too. This is because we assume that our clusters are in virial equilibrium before gas expulsion when the forming cluster total mass is $M_{\text{tot}} = M_{\star} + M_{\text{gas}} = M_{\star}/\text{SFE}_{\text{gl}}$, and therefore:

$$V \propto \sqrt{\frac{M_J}{r_h \text{SFE}_{\text{gl}}}}. \quad (39)$$

Chapter 3 already showed that the duration of the violent relaxation does not scale with the crossing time measured at the half-mass radius as we mentioned before. Let us assume that the violent relaxation duration scales with the crossing time (Eq. 38) measured at Jacobi radius instead, as we found in the case of different galactocentric distances. Then in Eq. 38 we can substitute V by Eq. 39, where M_J is replaced by R_J^3 according to Eq. 25. In this case we have the following expression for the end of violent relaxation:

$$t_{\text{VR}} \propto \sqrt{\frac{r_h \text{SFE}_{\text{gl}}}{R_J}}. \quad (40)$$

Since SFE_{gl} varies only from 0.15 to 0.25 in our simulations, the dependence of t_{VR} on SFE_{gl} is quite weak, less than 15%. Therefore, we average the duration of violent relaxation over all SFE_{gl} -models. Then, since the Jacobi radius is fixed for a given Galactocentric distance and a given mass, the violent relaxation duration is expected to scale mostly with the square root of the half-mass radius.

But, Fig. 28 shows us that the duration of violent relaxation for a given Galactocentric distance (i.e. the S+2, S+1, So and S−1 models) does not scale

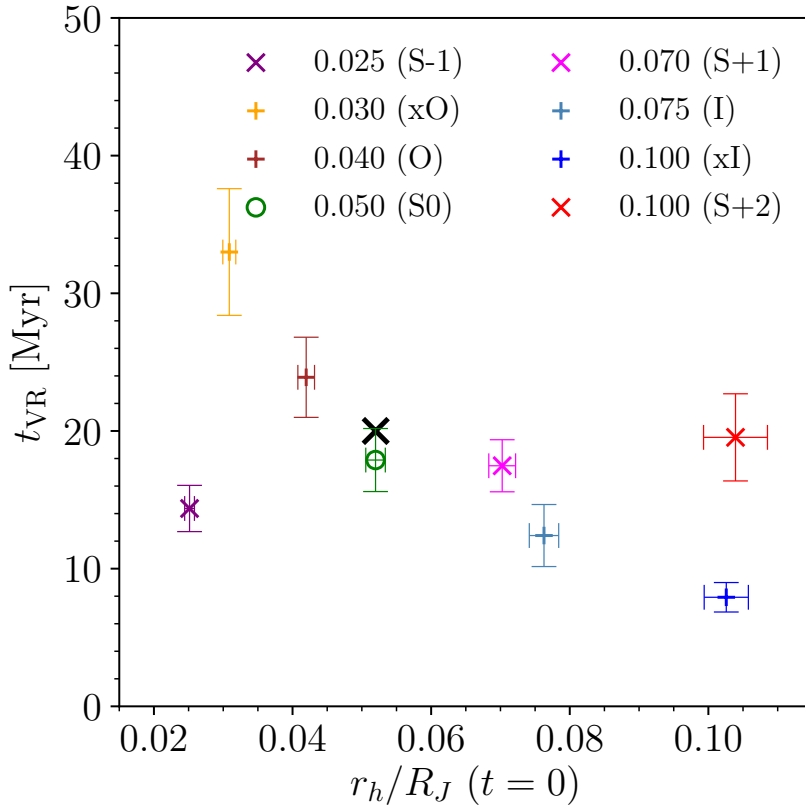


Figure 26: The end of violent relaxation as a function of the tidal field impact, characterized by half-mass to Jacobi radii ratio r_h/R_J at the time of gas expulsion. Each point represents all cluster models for a given tidal field impact. The black cross and the green open circle correspond to our ‘standard’ model set ($r_h/R_J = 0.052$ and $R_{orb} = 8.0$ kpc), where the former shows our earlier estimate from Chapter 3 and the latter corresponds to the new generalized estimate obtained in Section 5.3. The models marked with plus symbols are at different Galactocentric distances, while crosses indicate solar neighborhood clusters with different densities, therefore with different impact of the tidal field.

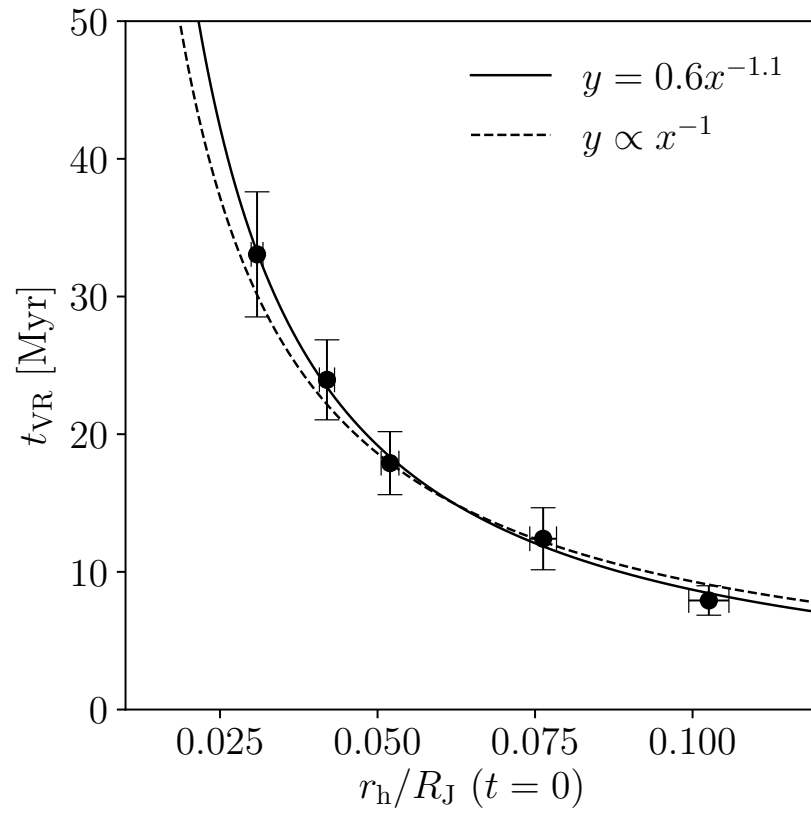


Figure 27: The end of violent relaxation duration as a function of the tidal field impact for the same clusters located at different Galactocentric distances. The solid line is the best fit power-law function. The dashed line corresponds to $t_{VR} \propto R_J$.

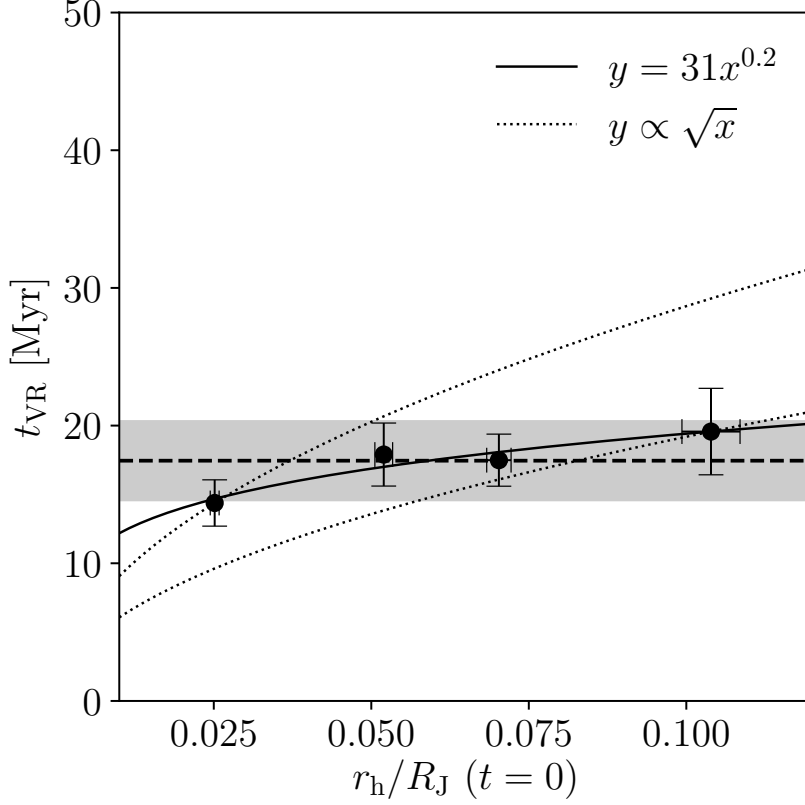


Figure 28: The violent relaxation duration as a function of the impact of the tidal field at a fixed Galactocentric distance. The solid line is the best fit power-law function. The dotted lines correspond to $t_{\text{VR}} \propto \sqrt{r_{\text{h}}}$ going through the most extreme models. The dashed horizontal line is the mean over all simulations of the solar neighborhood with the shaded area showing the standard deviation.

with the cluster half-mass radius to the power of $1/2$. We over-plot the relation $t_{\text{VR}} \propto \sqrt{r_{\text{h}}}$ through the most extreme cases with dotted lines in Fig. 28. Also the mean violent relaxation duration averaged over all simulations at $R_{\text{orb}} = 8$ kpc is shown with the dashed line. The shaded area corresponds to its standard deviation. The solid black line is the best fit power-law function. it has an index of $1/5$.

Probably, when we consider the fixed Jacobi radius and vary the cluster size, for a small $r_{\text{h}}/R_{\text{J}}$ (i.e. compact cluster), the surviving bound part of a cluster does not expand as much as to fill the Jacobi radius. Then this bound part of a cluster, when it stops its expansion, can still be surrounded by some to-be-unbound stars which are about to escape, but still need some time to reach the Jacobi radius. Therefore, the end of violent relaxation can be prolonged compared to a diffuse cluster as all unbound stars are leaving the Jacobi radius of the cluster.

In case of a diffuse cluster, that is, large $r_{\text{h}}/R_{\text{J}}$, the central part of a cluster can expand as much as to even overfill the Jacobi radius. Therefore the duration of the violent relaxation can become shorter for clusters with large $r_{\text{h}}/R_{\text{J}}$ than expected if it was following the relation $t_{\text{VR}} \propto \sqrt{r_{\text{h}}}$.

If that is the case, we can expect to have slightly higher final bound fraction for compact clusters, and lower final bound fraction for diffuse clusters.

5.4 FINAL BOUND FRACTION

The final bound fraction F_{bound} is the bound mass fraction measured at the end of violent relaxation t_{VR} . This is an indicator of cluster survivability after gas expulsion. We showed previously that the final bound fraction does not depend on the cluster birth mass M_* for solar neighborhood clusters (Chapter 3, Chapter 4). This stands also for other galactocentric distances. Figure 29 shows the final bound fraction against the birth mass at different Galactocentric distances ($R_{\text{orb}} = 2.9, 8.0, 18.0$ kpc from top to bottom). As we can see, for each global SFE (i.e. for each color) the final bound fraction stays constant within the error-bars and does not show any clear dependence on the birth mass of star clusters in all three panels (i.e. for all three galactocentric distances). Therefore, in the following figures, the final bound fraction for a given global SFE and a given tidal field impact has been averaged through all cluster birth masses.

Now, Figure 30 demonstrates that the final bound fraction of our model clusters is not significantly affected by the tidal field when we consider clusters at different Galactocentric distances. The color-coding, again, corresponds to the global SFE and is the same as in Fig.25 and 29.

Figure 31 presents the final bound fraction of star clusters as a function of tidal field impact for a fixed Galactocentric distance of $R_{\text{orb}} = 8$ kpc. The black dashed lines are the linear fits to the final bound fractions of a given global SFE as a function of $r_{\text{h}}/R_{\text{J}}$. Their slopes are shown on the right hand side of the figure. In this case, where different tidal field impacts are driven by various cluster densities (i.e. our solar neighborhood model clusters), a clear trend can be seen where the final bound fraction is a decreasing function of the tidal field impact (Fig. 31). Nevertheless, the differences in the final bound fraction are not very large and remain consistent with each other within the error-bars.

Figure 32 presents the final bound fraction as a function of the global SFE and the tidal field impact. Our model clusters with a given global SFE and tidal field impact are represented by the mean final bound fraction averaged over all birth masses and random realizations performed per model. Standard deviations are not shown for the sake of clarity. Our standard So-model clusters are indicated by green open circles. Solar neighborhood clusters with different tidal field impacts are represented by \times -symbols. Model clusters with different tidal field impacts due to different Galactocentric distances are indicated by $+$ -symbols. For each case, the color-coding corresponds to different tidal field impacts (see the key). We compare our results with those of Baumgardt and Kroupa (2007) obtained for instantaneous gas expulsion and different tidal field impacts $r_{\text{h}}/r_{\text{t}} = 0.01, 0.033, 0.06$ and 0.100 (black dots connected with lines, from top to bottom).

As we mentioned before, Baumgardt and Kroupa (2007) considered clusters with radially constant SFE, on circular orbit in a spherical gravitational potential representative of the host galaxy. In contrast, we consider clusters formed with a centrally-peaked SFE profile, as a result of star-formation taking place with a constant efficiency per free-fall time, and moving on circular orbits in the disk plane of an axisymmetric Galactic potential consisting of a bulge, a disk and a dark halo. In addition, we consider the impact of the tidal field not only at different Galactocentric distances, but also for clusters of different sizes, but at the same galactocentric distance.

As it is shown in Fig. 32, not only are our model clusters formed with a centrally-peaked SFE profile able to resist instantaneous gas expulsion on SFE as low as $\text{SFE}_{\text{gl}} = 0.15$, their survival likelihood is also independent of the impact of the tidal field within the scope of our simulations.

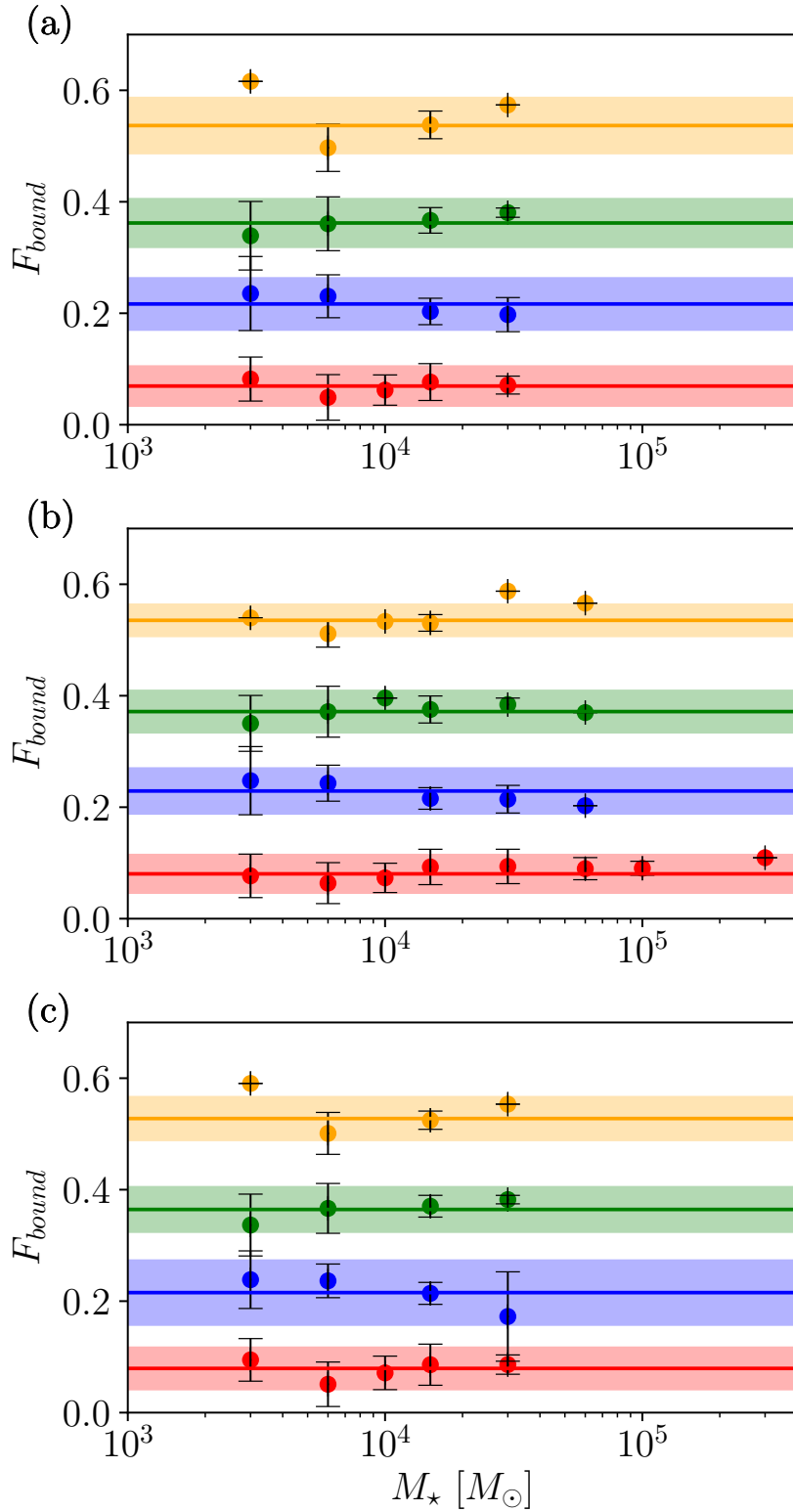


Figure 29: The final bound mass fraction as a function of cluster birth mass. Panels from top to bottom correspond to three Galactocentric distances of $R_{\text{orb}} = 2.9, 8.0, 18.0$ kpc. The corresponding tidal field impacts are: $r_{\text{h}}/R_{\text{J}} = 0.10, 0.052, 0.03$, respectively. The color-coding corresponds to different global SFEs as following: $\text{SFE}_{\text{gl}} = 0.15$ (red), 0.17 (blue), 0.20 (green), and 0.25 (yellow) and are the same as in Fig. 25. Each point corresponds to the mean and standard deviation of the random realizations performed for each model.

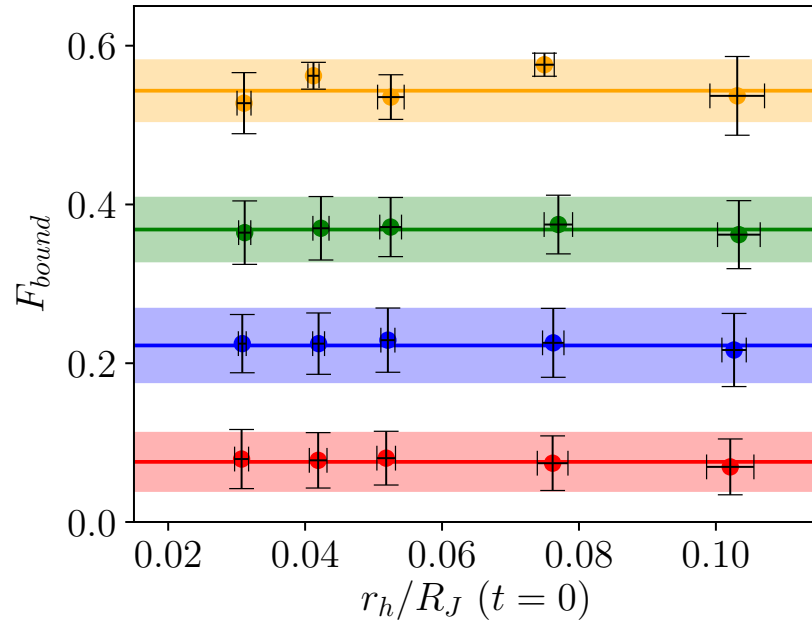


Figure 30: The final bound mass fraction as a function of tidal field impact for different Galactocentric distances. The color-coding corresponds to the global SFE and is the same as in Fig. 29. Each point corresponds to the mean and standard deviation of model clusters with the same global SFE and tidal field impact.

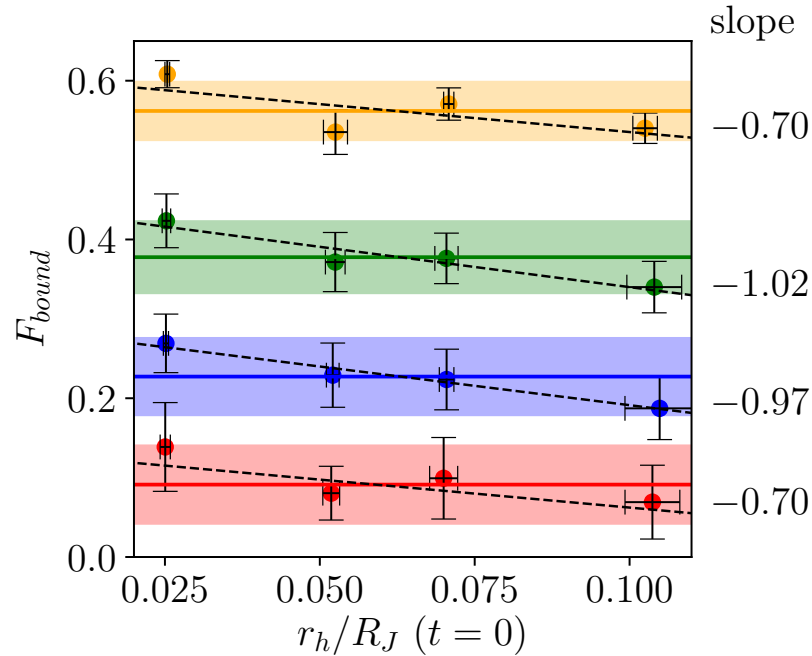


Figure 31: The bound mass fraction at the end of violent relaxation as a function of tidal field impact for different central densities at $R_{\text{orb}} = 8.0$ kpc. Different colors correspond to different global SFEs. Each point corresponds to the mean and standard deviation of clusters with the same global SFE at a given tidal field impact.

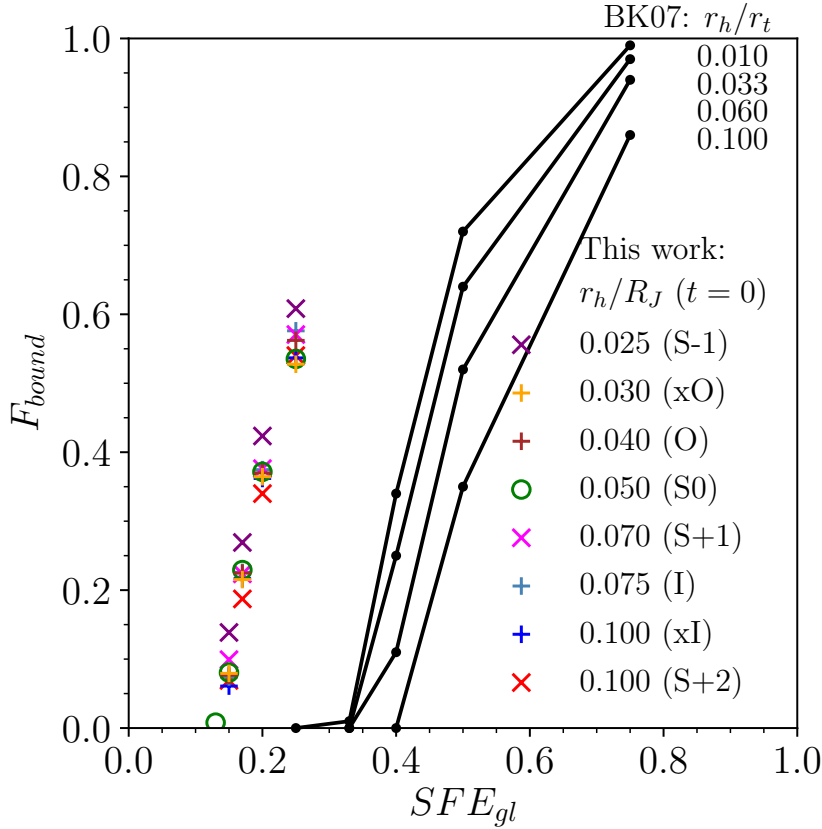


Figure 32: The final bound fraction as a function of global SFE and the tidal field impact. The different colors correspond to the clusters with different the tidal field impact of our model clusters. Green open circles show our So-models. The solar neighborhood clusters with different tidal field impact are shown by cross symbols, while clusters at different Galactocentric distances are presented by plus symbols. Each point correspond to a mean bound fraction of a set of simulations with a given global SFE and r_h/R_J . Each set of simulations consist of models with birth masses range from $3k$ to $30k M_\odot$ at least. Black curves correspond to the results of Baumgardt and Kroupa (2007) for the case of instantaneous gas expulsion, where the numbers shown next to black dots the strength of the tidal field in their simulations.

Relying on the results of our simulations we conclude that the survivability of star clusters after instantaneous gas expulsion is independent of the tidal field impact at different Galactocentric distances. The impact of the tidal field on clusters with different densities at a given Galactocentric distance results in small variations of about 0.1 in the final bound fraction.

5.5 CONCLUSIONS

We have studied the influence of the tidal field impact on the survivability of star clusters after instantaneous gas expulsion. To do so, we have expanded our grid of simulations from Chapter 3 and Chapter 4, and considered different Galactocentric distances ($R_{\text{orb}} = 2.9, 4.64, 8.0, 10.95, 18.0$ kpc), as well as solar neighborhood clusters (i.e. $R_{\text{orb}} = 8$ kpc) with different volume densities. Both cases yield variations of the impact of the tidal field, that we define as r_h/R_J .

Our model star clusters are formed with a centrally-peaked SFE profile and have circular orbits in the Galactic disc plane, with the Galactic potential modeled as a three-component axisymmetric Plummer-Kuzmin model (Just et al., 2009; Miyamoto and Nagai, 1975).

We have measured the duration of violent relaxation for all our model clusters. We define the end of violent relaxation as the moment when stellar evolutionary mass losses start dominating the rapid (violent) mass-loss resulting from gas expulsion.

As we showed previously in Chapter 3 the violent relaxation duration does not depend significantly on the cluster global SFE and birth masses. Therefore the violent relaxation duration is averaged over all birth masses and global SFEs for a given tidal field impact. We have found that the violent relaxation duration, measured at different Galactocentric distances, scales with the cluster crossing time measured at its Jacobi radius (Fig. 27). However, it is more or less constant when the impact of the tidal field varies through variations of cluster size/density at a given Galactocentric distance ($R_{\text{orb}} = 8$ kpc, see Fig 28). The violent relaxation does not last longer than 40-50 Myr in our simulations.

We have also measured the final bound fraction (i.e. bound mass fraction at the end of violent relaxation) of our clusters to quantify the impact of the tidal field on the cluster survivability. Identical clusters located at different Galactocentric distances, which thus experience different impacts of the tidal field, show the same final bound fraction at the end of violent relaxation irrespective of their galactocentric distance (Fig. 30). However, clusters at the same Galactocentric distance of 8 kpc, but different volume densities, which also experience different tidal field impacts, present small variations of about 0.1 in their final bound fraction such that compact clusters retain a higher final bound fraction than diffuse clusters. Therefore, we conclude that, within the scope of our simulations, the cluster survivability after instantaneous gas expulsion as measured by their bound mass fraction at the end of violent relaxation F_{bound} , is independent of the tidal field impact r_h/R_J .

Part IV

CONCLUSION

SUMMARY AND FUTURE WORKS

6.1 SUMMARY

Using a novel approach we have studied the evolution of star clusters from their formation in gaseous clumps till complete dissolution in the tidal field of their host galaxy. To that purpose, we have combined the semi-analytical “local-density-driven” cluster formation model of Parmentier and Pfalzner (2013) with direct N-body simulations of clusters following instantaneous gas expulsion. Our model clusters are formed with a centrally peaked SFE profile, that is, the residual gas has a density profile that is shallower than that of the embedded cluster. This configuration is expected if star formation proceeds with a constant star-formation efficiency per free-fall time in a centrally concentrated, spherically symmetric, molecular gas clump.

We have built a large grid of N-body simulations covering the parameter space of global SFE ($SFE_{gl} = [0.1, 0.25]$), cluster birth mass ($M_{\star} = [3 \times 10^3, 10^5]M_{\odot}$) and the tidal field impact ($r_h/R_j = [0.025, 0.10]$). The variation of the impact of the tidal field has been considered by varying the cluster galactocentric distance, as well as by the varying the size (hence volume density) of those located at a galactocentric distance of 8 kpc. The initial conditions for our direct N-body simulations were generated by the program “MKHALO” from the package “falcON”, adapted for our models with the specially developed acceleration plug-in GASPOTENTIAL. Our model star clusters have a Plummer profile and are in virial equilibrium with the gravitational potential of the cluster-forming clump immediately before gas expulsion. The residual gas contribution is computed from the local-density driven clustered star formation model in our GASPOTENTIAL plug-in. Our simulations include cluster mass loss by stellar evolution as well as the tidal field of a Milky-Way-like host galaxy.

We have studied the effect of the instantaneous expulsion of the residual star-forming gas on model star clusters of the solar neighborhood in Chapter 3. We have found that a star cluster with a minimum global SFE of 15 percent is able to survive instantaneous gas expulsion and to produce a bound cluster. Its violent relaxation lasts no longer than 20 Myr, independently of its global SFE and initial stellar mass. At the end of violent relaxation, the bound fractions of the surviving clusters with identical global SFEs are similar, regardless of their birth stellar mass M_{\star} . Their subsequent lifetime in the gravitational field of the Galaxy depends on their bound stellar masses. We therefore conclude that the critical SFE needed to produce a bound cluster is 15 percent, which is roughly half the earlier estimate of 33 percent. Thus we have markedly strengthened the survival likelihood of young clusters after instantaneous gas expulsion. Young clusters can now survive instantaneous gas expulsion with a global SFE as low as the SFEs observed for embedded clusters in the solar neighborhood (15-30 percent). The reason is that the star cluster density profile is steeper than that of the residual gas. However, in terms of the effective SFE, measured by the virial ratio of the cluster at gas expulsion, our results are in agreement with previous studies. The results were published in Shukirgaliyev et al. (2017).

Then, we have studied the long-term evolution of star clusters of the solar neighborhood, until their complete dissolution in the Galactic tidal field in Chapter 4. We have studied the relation between cluster dissolution time, t_{dis} , and cluster “initial” mass, M_{init} , defined as the cluster mass at the

end of the dynamical response to gas expulsion (i.e., violent relaxation), when the cluster age is 20–30 Myr. We have considered the “initial” mass to perform consistent comparisons with other works that neglect violent relaxation. We have found that the model clusters formed with a high SFE follow a tight mass-dependent relation, in agreement with previous theoretical studies. However, the low-SFE models present a large scatter in both the “initial” mass and the dissolution time and a shallower mass-dependent relation than high-SFE clusters, and most dissolve within 1 Gyr (cluster teenage mortality). Both groups differ in their structural properties on average. Combining two populations of clusters, high- and low-SFE ones, with domination of the latter, yields a cluster dissolution time for the solar neighborhood in agreement with that inferred from observations, without needing any additional destructive processes such as giant molecular cloud encounters. An apparent mass-independent relation may emerge for our low-SFE clusters when we neglect low-mass clusters (as expected for extragalactic observations), although more simulations are needed to investigate this aspect. Chapter 4 has been published as Shukirgaliyev et al. (2018a).

Finally, in Chapter 5 we have studied the impact of the Galactic tidal field on the survivability of star clusters following instantaneous gas expulsion. We have measured the duration of violent relaxation and the bound mass fraction of all our model clusters at the end of violent relaxation. We have found that the violent relaxation duration at different Galactocentric distances scales with the cluster crossing time measured at its Jacobi radius. In contrast, it is about constant when the impact of the tidal field varies through variations of the cluster size/density at a given Galactocentric distance of 8 kpc. The violent relaxation does not last longer than 40–50 Myr in our simulations. Identical model clusters placed at different Galactocentric distances result in a bound fraction at the end of violent relaxation independent of the tidal field impact. Clusters at a given Galactocentric distance, but with different densities, also experience tidal field impact variations, which result in limited variations of about 0.1 of their final bound fraction. We have concluded that the cluster survivability after instantaneous gas expulsion, as measured by their bound mass fraction at the end of violent relaxation, F_{bound} , is independent of the tidal field impact, r_h/R_J , where r_h and R_J are cluster half-mass radius and Jacobi radius. The results presented in Chapter 5 have been submitted for publication in MNRAS as Shukirgaliyev et al. (2018b).

6.2 FUTURE WORKS

There are a few projects that are already planned as a continuation of this thesis. In one of them we will study the few Gyr evolution of star clusters in the Milky Way (MW) and Large Magellanic Cloud (LMC). For that we will continue our existing simulations for the MW and will run new simulations of star cluster evolution, with our specific ICs, in the LMC using the LMC tidal-field model developed by Rossi, Bekki, and Hurley (2016). Luca Rossi has agreed to provide us with his code and tools in private communication.

Based on our simulations we will study:

- The effects of varying model input parameters quoted above on the first few Gyr of evolution of clusters. In particular, we will follow the cluster bound mass, size and structure, and estimate their lifetime. Different SFEs will result in different SC Roche volume filling factors and SC structures at the end of violent relaxation. Therefore they can lead to different dissolution mechanisms. Varying the cluster orbit we will investigate if a cluster dissolution mechanism independent of the tidal field impact exists.

- The observational biases on cluster mass and size estimates for the Solar neighborhood and LMC. In most cases the cluster mass is estimated by fitting the observed cluster surface brightness (SB) profile with King profiles. However, Meylan (2002) showed that tidally disrupting globular clusters with tidal tails are not well fitted with King models (see also Elson, Fall, and Freeman, 1987). This gives significant observational biases on the mass estimate of globular clusters. The situation is even worse for low mass, less concentrated clusters evolving in the tidal field of their host galaxy. We will make mock observations of our model clusters putting them together with simulated field star distribution of the host galaxy. We will then measure the mass of SC based on their “observed” SB profile and compare it to the actual cluster mass. For our study of the impact of observational biases on cluster mass estimates in the Solar neighborhood we will use the GALAXIA model (Sharma et al., 2011). The GALAXIA model reproduces the distribution of Galactic field stars in a given field of view in a heliocentric framework. We will integrate our simulation outputs into the GALAXIA model with tools we are currently developing. We will then produce mock observations of model clusters in the sea of Galactic field stars to study the observational biases. For our studies of star clusters in external galaxies, we will use some synthetic observation codes like COCOA (Askar et al., 2018) or MYSO (Khorrami, Vakili, and Chesneau, 2016, private communication with Dr. Z. Khorrami), or develop our own tools of mock observations if needed.
- Assuming the canonical power-law initial cluster mass function (ICMF), a log-normal distribution of SFEs (e.g. as estimated by Kainulainen, Federrath, and Henning, 2014) and different star-formation histories we will build the corresponding cluster age-mass distribution using our simulated star clusters and reproduce the cluster distributions observed in the Solar neighborhood and LMC for cluster ages younger than a few Gyr.

Furthermore, analyzing the outputs of our grid of simulations we will study star cluster structures and tidal tails. We will try to detect tidal tails of open clusters analyzing and comparing the mock observations of our simulations with the Gaia data. Many other interesting studies can be done based on the model of cluster evolution considered in this thesis.

Part V

APPENDIX



GASPOTENTIAL ACCELERATION PLUG-IN FOR MKHALO

A.1 MANUAL

I use program MKHALO from the package falCON (McMillan and Dehnen, 2007) to generate the initial phase-space distribution of stars in virial equilibrium within total (stars + gas) gravitational potential for my N-body simulations. I developed the special acceleration plug-in 'GASPOTENTIAL' to introduce the external gravitational potential of the residual gas. In order to start to use MKHALO with GASPOTENTIAL plug-in, one need to install the falCON (the "Force Algorithm with Complexity $\mathcal{O}(N)$ ") package.

falCON package can be installed easily with extensible Stellar Dynamics Tools NEMO (Teuben et al., 1995).

The official web-page of NEMO on github portal provides a simple 4 step instruction to install NEMO. Before proceed to this simple instruction I would like to note few issues I have found useful relying on my own experience:

- Work in C-shell. Whenever I tried to install NEMO within usual bash, I failed. Once I started C-shell by typing csh in terminal, everything goes very smooth. Even after successful installation, start C-shell before you run MKHALO.
- Do not change the recommended installation path. When I tried to install in other directory, I failed. But once I used the same path as given in the github web-page of NEMO it works without any problem.
- I tried only on Linux Operating system.

Here are the instruction from <https://teuben.github.io/nemo/#installation>:

```
%1 wget https://teuben.github.io/nemo/install_nemo
%2 chmod +x install_nemo
%3 ./install_nemo nemo=$HOME/opt/nemo
%4 source $HOME/opt/nemo/nemo_start.csh
```

After successful installation of NEMO you can use any program of falCON including MKHALO, which you can find in the following path:

```
$HOME/opt/nemo/usr/dehnen/falCON/bin/
```

Program MKHALO generates initial conditions for a spherical self-consistent N-body system in virial equilibrium within a given external potential. If you run MKHALO without any parameter, it gives nice description of all its parameters. Any available external potential can be used in MKHALO with parameter "acname". All available external potentials, also called acceleration plug-in, can be found in the following path:

```
$HOME/opt/nemo/usr/dehnen/falCON/acc/
```

Now we need to add our own, specially developed acceleration plug-in GASPOTENTIAL describing the gravitational potential of residual gas into falCON package.

To do so, first download the source file of acceleration plug-in GasPotential.cc from github: <https://github.com/BS-astronomer/GasPotential> or type in your terminal

```
git clone https://github.com/BS-astronomer/GasPotential.git
```

Once you have downloaded it, put the file `GasPotential.cc` into the acceleration plug-in source directory of `falcON`:

```
$HOME/opt/nemo/usr/dehnen/falcON/src/public/acc/
```

Next step to do, in order to compile the `GASPOTENTIAL` plug-in, is to add into `$HOME/opt/nemo/usr/dehnen/falcON/makepub` file under the commented line ‘accelerations’ the following lines (‘%1’ and ‘%2’ are given to indicate the numbers of lines and should not be added into `makepub` file):

```
%1 $(ACC)GasPotential.so: $(SACC)GasPotential.cc $(ACCT) $(
    defacc_h) $(makefiles)
%2 $(MAKE_ACC)
```

As for the next step, proceed into the main directory of `falcON`

```
cd $HOME/opt/nemo/usr/dehnen/falcON/
```

then compile the plug-in `GASPOTENTIAL`:

```
g++ -o $HOME/opt/nemo/usr/dehnen/falcON/acc/GasPotential.so $HOME
/opt/nemo/usr/dehnen/falcON/src/public/acc/GasPotential.cc -
Iinc/ -Iinc/utils/ -I$HOME/opt/nemo/inc -I$HOME/opt/nemo/lib
-D_FILE_OFFSET_BITS=64 -std=c++0x -march=native -mfpmath=sse
-mpreferred-stack-boundary=4 -ggdb3 -Wall -Wextra -Winit-
self -Wshadow -O2 -fPIC -fopenmp -funroll-loops -fforce-addr
-rdynamic -Llib/ -lfalcON -Lutils/lib -LWDutils -L$HOME/
opt/nemo/lib -lnemo -ldl -shared
```

and re-compile `MKHALO`

```
g++ -o $HOME/opt/nemo/usr/dehnen/falcON/bin/mkhalo $HOME/opt/nemo
/usr/dehnen/falcON/src/public/exe/mkhalo.cc -Iinc/ -Iinc/
utils/ -D_FILE_OFFSET_BITS=64 -std=c++0x -march=native -
mfpmath=sse -mpreferred-stack-boundary=4 -ggdb3 -Wall -Wextra
-Winit-self -Wshadow -O2 -fPIC -fopenmp -funroll-loops -
fforce-addr -rdynamic lib/halo.o -DfalcON_SINGLE -
DfalcON_NEMO -Llib/ -lfalcON -Lutils/lib -LWDutils -L$HOME
/opt/nemo/lib -lnemo -ldl -lm
```

Now, `MKHALO` program with `GASPOTENTIAL` acceleration plug-in is ready to use. In order to run, you need to copy the binary files

```
$HOME/opt/nemo/usr/dehnen/falcON/bin/mkhalo
```

and

```
$HOME/opt/nemo/usr/dehnen/falcON/acc/GasPotential.so
```

into your work directory. You also will need the program

```
$HOME/opt/nemo/usr/dehnen/falcON/s2a
```

to convert the output file of `MKHALO` from binary format into ASCII format.

`GASPOTENTIAL` plug-in recovers the gravitational potential of the residual gas using two parameters: ϵ_{ff} – SFE per free-fall time, and t_{SF} – star-formation duration.

The star cluster must have a Plummer model density profile, therefore the option: `model=Plummer` must be given always. The plug-in `GASPOTENTIAL` works in the same units as `MKHALO` program, that is

$$G = 1, \quad M_{\star} = 1, \quad a_{\star} = 1.$$

Here a_{\star} is the characteristic radius of Plummer model for a stellar cluster, G is the gravitational constant, and M_{\star} is the total stellar mass.

We calculate the global SFE as SFE within 10 Plummer radii,

$$\text{SFE}_{gl} = \frac{M_{\star}(r \leq 10a_{\star})}{M_{\star}(r \leq 10a_{\star}) + M_{\text{gas}}(r \leq 10a_{\star})}.$$

The residual gas mass can be simply calculated by taking an integral of residual gas density function

$$M_{\text{gas}}(r \leq 10a_*) = \int_0^{10a_*} r^2 \rho_{\text{gas}}(r) dr,$$

where

$$\rho_{\text{gas}}(r) = \frac{1}{k^2} - \frac{\rho_*}{2} - \frac{1}{2} \sqrt{K_2 + \frac{8}{k^6 K_1} + K_1},$$

$$k = \sqrt{\frac{8G}{3\pi} \epsilon_{\text{ff}} t_{\text{SF}}},$$

$$\rho_*(r) = \frac{3M_*}{4\pi a_*^3} \left(1 + \frac{r^2}{a_*^2}\right)^{-5/2}, \quad (\text{a Plummer model})$$

$$K_1 = \sqrt{\frac{\alpha^2 + \alpha(K_0 + 24) + K_0(K_0 + 12)}{12k^4 K_0}},$$

$$K_2 = \frac{(\alpha - K_0 + 24)(K_0 - \alpha)}{3k^4 K_0},$$

$$\alpha = k^4 \rho_*^2,$$

$$K_0 = \sqrt[3]{\alpha^3 + 36\alpha^2 + 216\alpha + 24\alpha\sqrt{3}(\alpha + 27)}.$$

Here we provide some values of SF duration, t_{SF} , corresponding to a given global SFE for $\epsilon_{\text{ff}} = 0.05$ in the following table:

SFE _{gl}	0.05	0.10	0.13	0.15	0.17	0.20	0.25	0.30	0.35	0.40	0.45	0.50
t _{SF}	2.14	6.30	9.58	12.09	14.86	19.53	28.74	39.96	53.53	69.94	89.85	114.22

Now, we can generate the initial conditions for N-body simulations. Here I provide an example bash-script to generate the initial conditions for N = 10k equal mass stars with SFE_{gl} = 0.15:

```
#!/bin/csh
### number of particles
N=10000
### SFE per free-fall time
e_ff=0.05
### SF time-span
t_sf=12.09
### random seed
seed=1111
### the name of output file
outfile=outputfilename
### running the code
./mkhalo out=${outfile} nbody=${N} model=Plummer accname=
  GasPotential accpars=${e_ff},${t_sf} seed=${seed}
### converting the output binary file into ASCII-file. header=f
  means we do not print a header of the ASCII file.
./s2a in=${outfile} out=${outfile}.dat rformat=%24.16 header=f
```

Before running the script make sure that the falcON environment is loaded, otherwise you run the following command:

```
source $HOME/opt/nemo/nemo_start.csh
```

This script will result an ASCII-file with N lines and 7 columns: one for mass, three for positions and three for velocities. However, PHI-GRAPE snapshot-file format is a bit different from this, and have three header lines describing the number of snapshot, total number of particles in snapshot and time of snapshot in each and one additional column for particles ordinal numbers. To bring the output of MKHALO into a PHI-GRAPE snapshot-file format one can use the following PYTHON script ‘makeinp.py’ (listing A.1), which can be run simply by typing ‘python makeinp.py’ in command line.

```
# makeinp.py
import numpy as np
in = 'inputfilename' #input file name should be provided inside
    the script
out = open('data.inp', 'w')
data = np.genfromtxt(in, unpack=True)
N = len(data[0])
#correction to the center of mass
M = np.sum(data[0])
for i in np.arange(6):
    data[i+1] -= np.sum(data[0]*data[i+1])/M
m = data[0]
x, y, z = data[1], data[2], data[3]
vx, vy, vz = data[4], data[5], data[6]
out.write("%06d\n%06d\n%.8e\n"%(0, N, 0))
for i in np.arange(N):
    out.write(
        '%06d\t %.10e\t % .10e % .10e % .10e\t % .10e % .10e % .10e\n'
        % (i, m[i], x[i], y[i], z[i], vx[i], vy[i], vz[i])
    )
out.close()
```

Now, the file named ‘data.inp’ is ready to use as initial conditions for the subsequent direct N -body simulation with PHI-GRAPE code. For that you need to copy the file into the directory with PHI-GRAPE executable file and run the simulations.

If you want to run with a given IMF, you just need to replace the masses of particles with the sample you generate according to your desired IMF. Since the both, kinetic and potential energies of particles contain their mass in each, the ratio of them, therefore the virial ratio of cluster does not change significantly when we sample the IMF.

A.2 GASPOTENTIAL CODE LISTING

```
#define POT_DEF
#include <cmath>
#include <defacc.h> // $NEMOINC/defacc.h

#define SQR(x) x*x
#define Pi 3.141592653589793

double M_sc = 1.0, a_pl = 1.0; //mass and scale radius of a star
    cluster
double K, RmaxGasPot;
double G_const = 1.0, e_ff, t_sf;
```

```

// rs() - calculates density of stars at given r (distance from
// the center) for a Plummer sphere
double rs(double const r){
    double rhos = (3.0 * M_sc)/(4.0 * Pi * a_pl*a_pl*a_pl)*
        pow((1 + r*r/a_pl*a_pl),(-(5./2.)));
    return rhos;
}

// rg3() - calculates density of residual gas at given r (
// distance from the centre)
// and parameter k, which calculates as
//  $K = \sqrt{8.0 * G\_const / (3.0 * Pi)} * e\_ff * t\_sf$ ;
double rg3(double const r, double const k){

    double k4 = k*k*k*k;
    double k6 = k*k*k*k*k*k;
    double aa = k4 * rs(r) * rs(r);

    double K0 = pow(( aa*aa*aa + 36*aa*aa + 216*aa + 24*aa*
        sqrt(3*(aa + 27)) ),(1.0/3.0));
    double K1 = sqrt( (aa*aa + aa*(K0 + 24) + K0*(K0 + 12))
        /(12*k4*K0) );
    double K2 = (aa - K0 + 24)*(K0 - aa)/(3*k4*K0);

    double rhog= 1.0/(k*k) - 0.5*rs(r) + K1 - 0.5*sqrt(K2 +
        8.0/(k6*K1) );
    return rhog;
}

namespace {

class GasPotential {

public:
    static const char* name() { return "GasPotential"; }
    GasPotential(const double*pars,
        int npar,
        const char *file)
    {
        if(npar < 2)
            warning("%s: recognizing 2 parameters:\n"
                " e_ff      star formation efficiency per free-
                fall time      [0.05]\n"
                " t_sf      duration of star formation phase [NB
                ]                [1.0]\n"
                "\n\n",name());
        if(file && file[0])
            warning("%s: file \"%s\" ignored",name(),file);
        double
            eff  = npar>0? pars[0] : 0.05,
            tsf  = npar>1? pars[1] : 1.0;

        if (!(eff < 1.0)&&(eff > 0))
            error("e_ff value is out of range: %f\n"
                "\t\t\t correct range is : 0.0 < e_ff < 1.0",eff);
        if (tsf <=0.0)

```

```

        error("t_sf value is out of range: %f\n"
              "\t\t\t correct range is : 0.0 < t_sf",tsf);
RmaxGasPot = 32.0; // Maximum radius for Plummer sphere with
                  a = 1 is 32 in mkhalo

e_ff      = eff;
t_sf      = tsf;

if(npar > 2) warning("%s: skipped parameters beyond 2\n"
                    " parameters : e_ff  = %f\n"
                    "                t_sf  = %f\n",
                    e_ff, t_sf ,name());
nemo_dprintf (1,
              "initializing %s\n"
              " parameters : e_ff  = %f\n"
              "                t_sf  = %f\n",
              name(), e_ff, t_sf);
}
template<typename scalar>
void potacc(scalar const&Rq,
            scalar      &P,
            scalar      &T) const
{
    register scalar R = std::sqrt(Rq);

    double ff_in, ff_out,
           R_min, R_max, R_len,
           R_len_1_2,
           R_len_1_4,
           R_in_min,
           R_out_max,
           R_in_max,
           R_out_min;

    int i1, i2, ii, bins, indx = 512;

    double dr_in, dr_out,
           R_in, R_out;

    R_min = 0.0;
    R_max = RmaxGasPot;

    R_len = R_max-R_min;
    R_len_1_2 = R_len/2.0;
    R_len_1_4 = R_len/4.0;

    K = sqrt(8.0 * G_const/(3.0 * Pi)) * e_ff * t_sf;
    // check whether we close to the center or to the outskirts in
    // order to find most efficient binning
    if (R < R_len_1_4){
        i1 = 1 * indx;
        i2 = 3 * indx;
    }
    else if (R > R_len_1_2 + R_len_1_4){
        i1 = 3 * indx;

```

```

        i2 = 1 * indx;
    }
    else{
        i1 = 2 * indx;
        i2 = 2 * indx;
    }

    R_in_min = R_min;
    R_out_max = R_max;

    if (!(R > R_max)) {
        R_in_max = R;
        R_out_min = R;
    }
    else{
        R_in_max = R_max;
        ff_out = 0.0;
        nemo_dprintf (1,
                    "warning in %s\t"
                    "max_R < R\n"
                    ,name());
        goto in_edge;
    }

    ii = i2;
    bins = 1+ii*2;

    dr_out = 1.0*(R_out_max - R_out_min)/(bins-1.0);
    ff_out= 0.0;
    for (int i = 0; i < bins; i++){
        R_out = dr_out * i + R_out_min;
        if ((i > 0)&&(i < bins-1)){
            if (i % 2 == 0)
                ff_out += 2 * rg3(R_out,K) * (R_out);
            else
                ff_out += 4 * rg3(R_out,K) * (R_out);
        }
        else
            ff_out += rg3(R_out,K) * (R_out);
    }
    ff_out *= dr_out / 3.0 * 4.0 * Pi;

in_edge:
    ii = i1;
    bins = 1+ii*2;

    dr_in = 1.0*(R_in_max - R_in_min)/(bins-1.0);

    ff_in = 0.0;
    for (int i = 0; i < bins; i++){
        R_in = dr_in * i + R_in_min;
        if ((i > 0)&&(i < bins-1)){
            if (i % 2 == 0)
                ff_in += 2 * rg3(R_in,K) * SQR(R_in);
            else
                ff_in += 4 * rg3(R_in,K) * SQR(R_in);
        }
    }

```

```

        }
        else
            ff_in += rg3(R_in,K) * SQR(R_in);
    }
    ff_in *= dr_in / 3.0 * 4.0 * Pi;

//ff_in - cumulative mass of gas inside R
//that is an integral : Int_0^R[4 Pi r^2 \rho_{gas}(r) dr]
//ff_out - an integral : Int_R^R_max[4 Pi r \rho_{gas}(r) dr]
    P = - (G_const * ff_in / R + G_const * ff_out);
    T = - G_const * ff_in / (R*R*R);
// nemo_dprintf (1,"R = %.8E P = %.8E T = %.8E\n",R,P,T);
    }
};
}
//-----

__DEF__ACC(SphericalPot<GasPotential>)
__DEF__POT(SphericalPot<GasPotential>)

//-----

```

BIBLIOGRAPHY

- Adams, F. C. (2000). “Theoretical Models of Young Open Star Clusters: Effects of a Gaseous Component and Gas Removal.” In: *ApJ* 542, pp. 964–973. DOI: [10.1086/317052](https://doi.org/10.1086/317052). eprint: [astro-ph/0006231](https://arxiv.org/abs/astro-ph/0006231).
- Askar, Abbas, Mirek Giersz, Wojciech Pych, and Emanuele Dalessandro (2018). “COCOA code for creating mock observations of star cluster models.” In: *MNRAS* 475, pp. 4170–4185. DOI: [10.1093/mnras/sty101](https://doi.org/10.1093/mnras/sty101).
- Banerjee, S. and P. Kroupa (2013). “Did the Infant R136 and NGC 3603 Clusters Undergo Residual Gas Expulsion?” In: *ApJ* 764, 29, p. 29. DOI: [10.1088/0004-637X/764/1/29](https://doi.org/10.1088/0004-637X/764/1/29). arXiv: [1301.3491](https://arxiv.org/abs/1301.3491).
- Bastian, N., A. Adamo, M. Gieles, E. Silva-Villa, H. J. G. L. M. Lamers, S. S. Larsen, L. J. Smith, I. S. Konstantopoulos, and E. Zackrisson (2012). “Stellar clusters in M83: formation, evolution, disruption and the influence of the environment.” In: *MNRAS* 419, pp. 2606–2622. DOI: [10.1111/j.1365-2966.2011.19909.x](https://doi.org/10.1111/j.1365-2966.2011.19909.x). arXiv: [1109.6015](https://arxiv.org/abs/1109.6015).
- Bate, Matthew R. (2009). “Stellar, brown dwarf and multiple star properties from hydrodynamical simulations of star cluster formation.” In: *MNRAS* 392, pp. 590–616. DOI: [10.1111/j.1365-2966.2008.14106.x](https://doi.org/10.1111/j.1365-2966.2008.14106.x). arXiv: [0811.0163](https://arxiv.org/abs/0811.0163) [[astro-ph](https://arxiv.org/abs/astro-ph)].
- Baumgardt, H. (2001). “Scaling of N-body calculations.” In: *MNRAS* 325, pp. 1323–1331. DOI: [10.1046/j.1365-8711.2001.04272.x](https://doi.org/10.1046/j.1365-8711.2001.04272.x). arXiv: [astro-ph/0012330](https://arxiv.org/abs/astro-ph/0012330) [[astro-ph](https://arxiv.org/abs/astro-ph)].
- Baumgardt, H., P. Hut, and D. C. Heggie (2002). “Long-term evolution of isolated N-body systems.” In: *MNRAS* 336, pp. 1069–1081. DOI: [10.1046/j.1365-8711.2002.05736.x](https://doi.org/10.1046/j.1365-8711.2002.05736.x). eprint: [astro-ph/0206258](https://arxiv.org/abs/astro-ph/0206258).
- Baumgardt, H. and P. Kroupa (2007). “A comprehensive set of simulations studying the influence of gas expulsion on star cluster evolution.” In: *MNRAS* 380, pp. 1589–1598. DOI: [10.1111/j.1365-2966.2007.12209.x](https://doi.org/10.1111/j.1365-2966.2007.12209.x). arXiv: [0707.1944](https://arxiv.org/abs/0707.1944).
- Baumgardt, H. and J. Makino (2003). “Dynamical evolution of star clusters in tidal fields.” In: *MNRAS* 340, pp. 227–246. DOI: [10.1046/j.1365-8711.2003.06286.x](https://doi.org/10.1046/j.1365-8711.2003.06286.x). eprint: [astro-ph/0211471](https://arxiv.org/abs/astro-ph/0211471).
- Berczik, P., K. Nitadori, S. Zhong, R. Spurzem, T. Hamada, X. Wang, I. Berentzen, A. Veles, and W. Ge (2011). “High performance massively parallel direct N-body simulations on large GPU clusters.” In: *International conference on High Performance Computing, Kyiv, Ukraine, October 8-10, 2011.*, p. 8-18, pp. 8–18.
- Berczik, P., R. Spurzem, L. Wang, S. Zhong, and S. Huang (2013). “Up to 700k GPU cores, Kepler, and the Exascale future for simulations of star clusters around black holes.” In: *Third International Conference “High Performance Computing”, HPC-UA 2013*, pp. 52–59. arXiv: [1312.1789](https://arxiv.org/abs/1312.1789) [[astro-ph](https://arxiv.org/abs/astro-ph).IM].

- Boily, C. M. and P. Kroupa (2003a). “The impact of mass loss on star cluster formation - I. Analytical results.” In: *MNRAS* 338, pp. 665–672. DOI: [10.1046/j.1365-8711.2003.06076.x](https://doi.org/10.1046/j.1365-8711.2003.06076.x). eprint: [astro-ph/0210378](https://arxiv.org/abs/astro-ph/0210378).
- (2003b). “The impact of mass loss on star cluster formation - II. Numerical N-body integration and further applications.” In: *MNRAS* 338, pp. 673–686. DOI: [10.1046/j.1365-8711.2003.06101.x](https://doi.org/10.1046/j.1365-8711.2003.06101.x). eprint: [astro-ph/0211026](https://arxiv.org/abs/astro-ph/0211026).
- Bonell, F., A. M. Bataille, S. Andrieu, C. Tiusan, B. Kierren, G. Lenguaigne, and D. Lacour (2008). “Influence of interfacial oxygen on single-crystal magnetic tunnel junctions.” In: *European Physical Journal Applied Physics* 43, pp. 357–361. DOI: [10.1051/epjap:2008100](https://doi.org/10.1051/epjap:2008100).
- Bonnell, I. A., R. J. Smith, P. C. Clark, and M. R. Bate (2011). “The efficiency of star formation in clustered and distributed regions.” In: *MNRAS* 410, pp. 2339–2346. DOI: [10.1111/j.1365-2966.2010.17603.x](https://doi.org/10.1111/j.1365-2966.2010.17603.x). arXiv: [1009.1152](https://arxiv.org/abs/1009.1152).
- Boutloukos, S. G. and H. J. G. L. M. Lamers (2003). “Star cluster formation and disruption time-scales - I. An empirical determination of the disruption time of star clusters in four galaxies.” In: *MNRAS* 338, pp. 717–732. DOI: [10.1046/j.1365-8711.2003.06083.x](https://doi.org/10.1046/j.1365-8711.2003.06083.x). eprint: [astro-ph/0210595](https://arxiv.org/abs/astro-ph/0210595).
- Brinkmann, N., S. Banerjee, B. Motwani, and P. Kroupa (2017). “The bound fraction of young star clusters.” In: *A&A* 600, A49, A49. DOI: [10.1051/0004-6361/201629312](https://doi.org/10.1051/0004-6361/201629312). arXiv: [1611.05871](https://arxiv.org/abs/1611.05871).
- Bruzual, G. and S. Charlot (2003). “Stellar population synthesis at the resolution of 2003.” In: *MNRAS* 344, pp. 1000–1028. DOI: [10.1046/j.1365-8711.2003.06897.x](https://doi.org/10.1046/j.1365-8711.2003.06897.x). arXiv: [astro-ph/0309134](https://arxiv.org/abs/astro-ph/0309134) [[astro-ph](https://arxiv.org/abs/astro-ph)].
- Calzetti, D. et al. (2015). “Legacy Extragalactic UV Survey (LEGUS) With the Hubble Space Telescope. I. Survey Description.” In: *AJ* 149, 51, p. 51. DOI: [10.1088/0004-6256/149/2/51](https://doi.org/10.1088/0004-6256/149/2/51). arXiv: [1410.7456](https://arxiv.org/abs/1410.7456).
- Chandar, R., S. M. Fall, and B. C. Whitmore (2010). “New Tests for Disruption Mechanisms of Star Clusters: The Large and Small Magellanic Clouds.” In: *ApJ* 711, pp. 1263–1279. DOI: [10.1088/0004-637X/711/2/1263](https://doi.org/10.1088/0004-637X/711/2/1263). arXiv: [1002.0779](https://arxiv.org/abs/1002.0779).
- Chandar, R., B. C. Whitmore, D. Calzetti, and R. O’Connell (2014). “Star-cluster Mass and Age Distributions of Two Fields in M83 Based on HST/WFC3 Observations.” In: *ApJ* 787, 17, p. 17. DOI: [10.1088/0004-637X/787/1/17](https://doi.org/10.1088/0004-637X/787/1/17). arXiv: [1406.1157](https://arxiv.org/abs/1406.1157).
- Chandar, R., B. C. Whitmore, D. Dinino, R. C. Kennicutt, L.-H. Chien, E. Schinnerer, and S. Meidt (2016). “The Age, Mass, and Size Distributions of Star Clusters in M51.” In: *ApJ* 824, 71, p. 71. DOI: [10.3847/0004-637X/824/2/71](https://doi.org/10.3847/0004-637X/824/2/71).
- Chandrasekhar, Subrahmanyan (1942). *Principles of stellar dynamics*.
- Clarke, C. (2010). “The physics and modes of star cluster formation: simulations.” In: *Philosophical Transactions of the Royal Society of London Series A* 368, pp. 733–754. DOI: [10.1098/rsta.2009.0262](https://doi.org/10.1098/rsta.2009.0262). arXiv: [0911.0780](https://arxiv.org/abs/0911.0780) [[astro-ph](https://arxiv.org/abs/astro-ph).GA].

- Dib, S., J. Gutkin, W. Brandner, and S. Basu (2013). "Feedback-regulated star formation - II. Dual constraints on the SFE and the age spread of stars in massive clusters." In: *MNRAS* 436, pp. 3727–3740. DOI: [10.1093/mnras/stt1857](https://doi.org/10.1093/mnras/stt1857). arXiv: [1306.6338](https://arxiv.org/abs/1306.6338).
- Duboshin, G. N. (1968). *Nebesnaia mekhanika, Osnovnyye zadachi i metody*. Nauka, Moscow, 1968.
- Elson, R. A. W., S. M. Fall, and K. C. Freeman (1987). "The structure of young star clusters in the Large Magellanic Cloud." In: *ApJ* 323, pp. 54–78. DOI: [10.1086/165807](https://doi.org/10.1086/165807).
- Ernst, A., P. Berczik, A. Just, and T. Noel (2015). "Roche volume filling and the dissolution of open star clusters." In: *Astronomische Nachrichten* 336, p. 577. DOI: [10.1002/asna.201512192](https://doi.org/10.1002/asna.201512192). arXiv: [1506.02862](https://arxiv.org/abs/1506.02862).
- Evans II, N. J. et al. (2009). "The Spitzer c2d Legacy Results: Star-Formation Rates and Efficiencies; Evolution and Lifetimes." In: *ApJS* 181, 321–350, pp. 321–350. DOI: [10.1088/0067-0049/181/2/321](https://doi.org/10.1088/0067-0049/181/2/321). arXiv: [0811.1059](https://arxiv.org/abs/0811.1059).
- Fall, S. M. and R. Chandar (2012). "Similarities in Populations of Star Clusters." In: *ApJ* 752, 96, p. 96. DOI: [10.1088/0004-637X/752/2/96](https://doi.org/10.1088/0004-637X/752/2/96). arXiv: [1206.4237](https://arxiv.org/abs/1206.4237).
- Fall, S. M., R. Chandar, and B. C. Whitmore (2009). "New Tests for Disruption Mechanisms of Star Clusters: Methods and Application to the Antennae Galaxies." In: *ApJ* 704, pp. 453–468. DOI: [10.1088/0004-637X/704/1/453](https://doi.org/10.1088/0004-637X/704/1/453). arXiv: [0910.1044](https://arxiv.org/abs/0910.1044).
- Farias, J. P., R. Smith, M. Fellhauer, S. Goodwin, G. N. Candlish, M. Blaña, and R. Dominguez (2015). "The difficult early stages of embedded star clusters and the importance of the pre-gas expulsion virial ratio." In: *MNRAS* 450, pp. 2451–2458. DOI: [10.1093/mnras/stv790](https://doi.org/10.1093/mnras/stv790). arXiv: [1504.02474](https://arxiv.org/abs/1504.02474).
- Farias, J. P., M. Fellhauer, R. Smith, R. Domínguez, and J. Dabringhausen (2018). "Gas expulsion in highly substructured embedded star clusters." In: *MNRAS* 476, pp. 5341–5357. DOI: [10.1093/mnras/sty597](https://doi.org/10.1093/mnras/sty597).
- Fellhauer, M. and P. Kroupa (2005). "Star Cluster Survival in Star Cluster Complexes under Extreme Residual Gas Expulsion." In: *ApJ* 630, pp. 879–886. DOI: [10.1086/432110](https://doi.org/10.1086/432110). eprint: [astro-ph/0505411](https://arxiv.org/abs/astro-ph/0505411).
- Fujii, M. S. and S. Portegies Zwart (2016). "The Formation and Dynamical Evolution of Young Star Clusters." In: *ApJ* 817, 4, p. 4. DOI: [10.3847/0004-637X/817/1/4](https://doi.org/10.3847/0004-637X/817/1/4). arXiv: [1512.00090](https://arxiv.org/abs/1512.00090).
- Fukushige, T. and D. C. Heggie (1995). "Pre-collapse evolution of galactic globular clusters." In: *MNRAS* 276, pp. 206–218. DOI: [10.1093/mnras/276.1.206](https://doi.org/10.1093/mnras/276.1.206). eprint: [astro-ph/9405058](https://arxiv.org/abs/astro-ph/9405058).
- Geyer, M. P. and A. Burkert (2001). "The effect of gas loss on the formation of bound stellar clusters." In: *MNRAS* 323, pp. 988–994. DOI: [10.1046/j.1365-8711.2001.04257.x](https://doi.org/10.1046/j.1365-8711.2001.04257.x). eprint: [astro-ph/0007413](https://arxiv.org/abs/astro-ph/0007413).
- Gieles, M. and H. Baumgardt (2008). "Lifetimes of tidally limited star clusters with different radii." In: *MNRAS* 389, pp. L28–L32. DOI: [10.1111/j.1745-3933.2008.00515.x](https://doi.org/10.1111/j.1745-3933.2008.00515.x). arXiv: [0806.2327](https://arxiv.org/abs/0806.2327).

- Gieles, M., S. F. Portegies Zwart, H. Baumgardt, E. Athanassoula, H. J. G. L. M. Lamers, M. Sipior, and J. Leenaarts (2006). “Star cluster disruption by giant molecular clouds.” In: *MNRAS* 371, pp. 793–804. DOI: [10.1111/j.1365-2966.2006.10711.x](https://doi.org/10.1111/j.1365-2966.2006.10711.x). eprint: [astro-ph/0606451](https://arxiv.org/abs/astro-ph/0606451).
- Girichidis, P., C. Federrath, R. Allison, R. Banerjee, and R. S. Klessen (2012). “Importance of the initial conditions for star formation - III. Statistical properties of embedded protostellar clusters.” In: *MNRAS* 420, pp. 3264–3280. DOI: [10.1111/j.1365-2966.2011.20250.x](https://doi.org/10.1111/j.1365-2966.2011.20250.x). arXiv: [1111.5440](https://arxiv.org/abs/1111.5440) [astro-ph.SR].
- Goodwin, S. P. (1997). “Residual gas expulsion from young globular clusters.” In: *MNRAS* 284, pp. 785–802. DOI: [10.1093/mnras/284.4.785](https://doi.org/10.1093/mnras/284.4.785). eprint: [astro-ph/9607083](https://arxiv.org/abs/astro-ph/9607083).
- (2009). “The effect of the dynamical state of clusters on gas expulsion and infant mortality.” In: *Ap&SS* 324, pp. 259–263. DOI: [10.1007/s10509-009-0116-5](https://doi.org/10.1007/s10509-009-0116-5). arXiv: [0802.2207](https://arxiv.org/abs/0802.2207).
- Goodwin, S. P. and N. Bastian (2006). “Gas expulsion and the destruction of massive young clusters.” In: *MNRAS* 373, pp. 752–758. DOI: [10.1111/j.1365-2966.2006.11078.x](https://doi.org/10.1111/j.1365-2966.2006.11078.x). eprint: [astro-ph/0609477](https://arxiv.org/abs/astro-ph/0609477).
- Gutermuth, R. A., J. L. Pipher, S. T. Megeath, P. C. Myers, L. E. Allen, and T. S. Allen (2011). “A Correlation between Surface Densities of Young Stellar Objects and Gas in Eight Nearby Molecular Clouds.” In: *ApJ* 739, 84, p. 84. DOI: [10.1088/0004-637X/739/2/84](https://doi.org/10.1088/0004-637X/739/2/84). arXiv: [1107.0966](https://arxiv.org/abs/1107.0966).
- Higuchi, A. E., Y. Kuroono, M. Saito, and R. Kawabe (2009). “A Mapping Survey of Dense Clumps Associated with Embedded Clusters: Evolutionary Stages of Cluster-forming Clumps.” In: *ApJ* 705, pp. 468–482. DOI: [10.1088/0004-637X/705/1/468](https://doi.org/10.1088/0004-637X/705/1/468). arXiv: [0909.1132](https://arxiv.org/abs/0909.1132).
- Hillenbrand, L. A. and J. M. Carpenter (2000). “Constraints on the Stellar/Substellar Mass Function in the Inner Orion Nebula Cluster.” In: *ApJ* 540, pp. 236–254. DOI: [10.1086/309309](https://doi.org/10.1086/309309). eprint: [astro-ph/0003293](https://arxiv.org/abs/astro-ph/0003293).
- Hills, J. G. (1980). “The effect of mass loss on the dynamical evolution of a stellar system - Analytic approximations.” In: *ApJ* 235, pp. 986–991. DOI: [10.1086/157703](https://doi.org/10.1086/157703).
- Hopkins, P. F., D. Narayanan, N. Murray, and E. Quataert (2013). “Dense molecular gas: a sensitive probe of stellar feedback models.” In: *MNRAS* 433, pp. 69–77. DOI: [10.1093/mnras/stt688](https://doi.org/10.1093/mnras/stt688). arXiv: [1209.0459](https://arxiv.org/abs/1209.0459).
- Hurley, J. R., O. R. Pols, and C. A. Tout (2000). “Comprehensive analytic formulae for stellar evolution as a function of mass and metallicity.” In: *MNRAS* 315, pp. 543–569. DOI: [10.1046/j.1365-8711.2000.03426.x](https://doi.org/10.1046/j.1365-8711.2000.03426.x). eprint: [astro-ph/0001295](https://arxiv.org/abs/astro-ph/0001295).
- Johnson, Harold L. (1954). “Galactic Clusters and Stellar Evolution.” In: *ApJ* 120, p. 325. DOI: [10.1086/145918](https://doi.org/10.1086/145918).
- Just, A., P. Berczik, M. I. Petrov, and A. Ernst (2009). “Quantitative analysis of clumps in the tidal tails of star clusters.” In: *MNRAS* 392, pp. 969–981. DOI: [10.1111/j.1365-2966.2008.14099.x](https://doi.org/10.1111/j.1365-2966.2008.14099.x). arXiv: [0808.3293](https://arxiv.org/abs/0808.3293).

- Kainulainen, J., C. Federrath, and T. Henning (2014). "Unfolding the Laws of Star Formation: The Density Distribution of Molecular Clouds." In: *Science* 344, pp. 183–185. DOI: [10.1126/science.1248724](https://doi.org/10.1126/science.1248724). arXiv: [1404.2722](https://arxiv.org/abs/1404.2722).
- Kennicutt, Robert C. and Neal J. Evans (2012). "Star Formation in the Milky Way and Nearby Galaxies." In: *Annual Review of Astronomy and Astrophysics* 50, pp. 531–608. DOI: [10.1146/annurev-astro-081811-125610](https://doi.org/10.1146/annurev-astro-081811-125610).
- Khorrami, Zeinab, Farrokh Vakili, and Olivier Chesneau (2016). "Image modeling of compact starburst clusters: I. R136." In: *ArXiv e-prints*, arXiv:1605.07533, arXiv:1605.07533. arXiv: [1605.07533](https://arxiv.org/abs/1605.07533) [astro-ph.SR].
- Kroupa, P. (2001). "On the variation of the initial mass function." In: *MNRAS* 322, pp. 231–246. DOI: [10.1046/j.1365-8711.2001.04022.x](https://doi.org/10.1046/j.1365-8711.2001.04022.x). eprint: [astro-ph/0009005](https://arxiv.org/abs/astro-ph/0009005).
- Kroupa, Pavel, Sverre Aarseth, and Jarrod Hurley (2001). "The formation of a bound star cluster: from the Orion nebula cluster to the Pleiades." In: *MNRAS* 321, pp. 699–712. DOI: [10.1046/j.1365-8711.2001.04050.x](https://doi.org/10.1046/j.1365-8711.2001.04050.x). arXiv: [astro-ph/0009470](https://arxiv.org/abs/astro-ph/0009470).
- Kruijssen, J. M. Diederik, F. Inti Pelupessy, Henny J. G. L. M. Lamers, Simon F. Portegies Zwart, and Vincent Icke (2011). "Modelling the formation and evolution of star cluster populations in galaxy simulations." In: *MNRAS* 414, pp. 1339–1364. DOI: [10.1111/j.1365-2966.2011.18467.x](https://doi.org/10.1111/j.1365-2966.2011.18467.x). arXiv: [1102.1013](https://arxiv.org/abs/1102.1013) [astro-ph.CO].
- Krumholz, M. R. and C. D. Matzner (2009). "The Dynamics of Radiation-pressure-dominated H II Regions." In: *ApJ* 703, pp. 1352–1362. DOI: [10.1088/0004-637X/703/2/1352](https://doi.org/10.1088/0004-637X/703/2/1352). arXiv: [0906.4343](https://arxiv.org/abs/0906.4343) [astro-ph.SR].
- Krumholz, M. R. and J. C. Tan (2007). "Slow Star Formation in Dense Gas: Evidence and Implications." In: *ApJ* 654, pp. 304–315. DOI: [10.1086/509101](https://doi.org/10.1086/509101). eprint: [astro-ph/0606277](https://arxiv.org/abs/astro-ph/0606277).
- Kudryavtseva, N. et al. (2012). "Instantaneous Starburst of the Massive Clusters Westerlund 1 and NGC 3603 YC." In: *ApJ* 750, L44, p. L44. DOI: [10.1088/2041-8205/750/2/L44](https://doi.org/10.1088/2041-8205/750/2/L44). arXiv: [1204.5481](https://arxiv.org/abs/1204.5481).
- Lada, C. J., M. Lombardi, and J. F. Alves (2010). "On the Star Formation Rates in Molecular Clouds." In: *ApJ* 724, pp. 687–693. DOI: [10.1088/0004-637X/724/1/687](https://doi.org/10.1088/0004-637X/724/1/687). arXiv: [1009.2985](https://arxiv.org/abs/1009.2985).
- Lada, C. J., M. Margulis, and D. Dearborn (1984). "The formation and early dynamical evolution of bound stellar systems." In: *ApJ* 285, pp. 141–152. DOI: [10.1086/162485](https://doi.org/10.1086/162485).
- Lada, Charles J. and Elizabeth A. Lada (2003). "Embedded Clusters in Molecular Clouds." In: *Annual Review of Astronomy and Astrophysics* 41, pp. 57–115. DOI: [10.1146/annurev.astro.41.011802.094844](https://doi.org/10.1146/annurev.astro.41.011802.094844).
- Lada, E. A., D. L. Depoy, N. J. Evans II, and I. Gatley (1991). "A 2.2 micron survey in the L1630 molecular cloud." In: *ApJ* 371, pp. 171–182. DOI: [10.1086/169881](https://doi.org/10.1086/169881).
- Lamers, H. J. G. L. M., H. Baumgardt, and M. Gieles (2010). "Mass-loss rates and the mass evolution of star clusters." In: *MNRAS* 409, pp. 305–328. DOI: [10.1111/j.1365-2966.2010.17309.x](https://doi.org/10.1111/j.1365-2966.2010.17309.x). arXiv: [1007.1078](https://arxiv.org/abs/1007.1078).

- Lamers, H. J. G. L. M., M. Gieles, and S. F. Portegies Zwart (2005). "Disruption time scales of star clusters in different galaxies." In: *A&A* 429, pp. 173–179. DOI: [10.1051/0004-6361:20041476](https://doi.org/10.1051/0004-6361:20041476). eprint: [astro-ph/0408235](https://arxiv.org/abs/astro-ph/0408235).
- Lamers, H. J. G. L. M., M. Gieles, N. Bastian, H. Baumgardt, N. V. Kharchenko, and S. Portegies Zwart (2005). "An analytical description of the disruption of star clusters in tidal fields with an application to Galactic open clusters." In: *A&A* 441, pp. 117–129. DOI: [10.1051/0004-6361:20042241](https://doi.org/10.1051/0004-6361:20042241). eprint: [astro-ph/0505558](https://arxiv.org/abs/astro-ph/0505558).
- Lamers, Henny J. G. L. M. (2009). "The Baltimore and Utrecht models for cluster dissolution." In: *Ap&SS* 324, pp. 183–186. DOI: [10.1007/s10509-009-0125-4](https://doi.org/10.1007/s10509-009-0125-4). arXiv: [0804.2148](https://arxiv.org/abs/0804.2148).
- Lee, P. L. and S. P. Goodwin (2016). "Surviving gas expulsion with substructure." In: *MNRAS* 460, pp. 2997–3001. DOI: [10.1093/mnras/stw988](https://doi.org/10.1093/mnras/stw988).
- Leisawitz, D., F. N. Bash, and P. Thaddeus (1989). "A CO survey of regions around 34 open clusters." In: *ApJS* 70, pp. 731–812. DOI: [10.1086/191357](https://doi.org/10.1086/191357).
- Linden, S. T. et al. (2017). "Massive Star Cluster Formation and Destruction in Luminous Infrared Galaxies in GOALS." In: *ApJ* 843, 91, p. 91. DOI: [10.3847/1538-4357/aa7266](https://doi.org/10.3847/1538-4357/aa7266). arXiv: [1705.03370](https://arxiv.org/abs/1705.03370).
- Lynden-Bell, D. (1967). "Statistical mechanics of violent relaxation in stellar systems." In: *MNRAS* 136, p. 101. DOI: [10.1093/mnras/136.1.101](https://doi.org/10.1093/mnras/136.1.101).
- McMillan, P. J. and W. Dehnen (2007). "Initial conditions for disc galaxies." In: *MNRAS* 378, pp. 541–550. DOI: [10.1111/j.1365-2966.2007.11753.x](https://doi.org/10.1111/j.1365-2966.2007.11753.x). eprint: [astro-ph/0703534](https://arxiv.org/abs/astro-ph/0703534).
- Messa, M. et al. (2018). "The young star cluster population of M51 with LEGUS - II. Testing environmental dependences." In: *MNRAS* 477, pp. 1683–1707. DOI: [10.1093/mnras/sty577](https://doi.org/10.1093/mnras/sty577). arXiv: [1803.08527](https://arxiv.org/abs/1803.08527).
- Meyer-Hofmeister, E. (1969). "A theoretical Hertzsprung-Russell-diagram for the star cluster NGC 1866." In: *A&A* 2, pp. 143–150.
- Meylan, Georges (2002). "Mass Determinations of Star Clusters." In: *Extragalactic Star Clusters*. Ed. by Douglas Paul Geisler, Eva K. Grebel, and Dante Minniti. Vol. 207, p. 555. arXiv: [astro-ph/0107063](https://arxiv.org/abs/astro-ph/0107063) [[astro-ph](https://arxiv.org/abs/astro-ph)].
- Miyamoto, M. and R. Nagai (1975). "Three-dimensional models for the distribution of mass in galaxies." In: *PASJ* 27, pp. 533–543.
- Moeckel, N., C. Holland, C. J. Clarke, and I. A. Bonnell (2012). "The rapid dispersal of low-mass virialized clusters." In: *MNRAS* 425, pp. 450–459. DOI: [10.1111/j.1365-2966.2012.21494.x](https://doi.org/10.1111/j.1365-2966.2012.21494.x). arXiv: [1205.1677](https://arxiv.org/abs/1205.1677) [[astro-ph](https://arxiv.org/abs/astro-ph).SR].
- Murray, N. (2011). "Star Formation Efficiencies and Lifetimes of Giant Molecular Clouds in the Milky Way." In: *ApJ* 729, 133, p. 133. DOI: [10.1088/0004-637X/729/2/133](https://doi.org/10.1088/0004-637X/729/2/133). arXiv: [1007.3270](https://arxiv.org/abs/1007.3270).
- Murray, N., E. Quataert, and T. A. Thompson (2010). "The Disruption of Giant Molecular Clouds by Radiation Pressure & the Efficiency of Star Formation in Galaxies." In: *ApJ* 709, pp. 191–

209. DOI: [10.1088/0004-637X/709/1/191](https://doi.org/10.1088/0004-637X/709/1/191). arXiv: [0906.5358](https://arxiv.org/abs/0906.5358) [astro-ph.GA].
- Parmentier, G. and H. Baumgardt (2012). “The mass function and dynamical mass of young star clusters: why their initial crossing-time matters crucially.” In: *MNRAS* 427, pp. 1940–1952. DOI: [10.1111/j.1365-2966.2012.22004.x](https://doi.org/10.1111/j.1365-2966.2012.22004.x). arXiv: [1209.0766](https://arxiv.org/abs/1209.0766).
- Parmentier, G. and G. Gilmore (2007). “The origin of the Gaussian initial mass function of old globular cluster systems.” In: *MNRAS* 377, pp. 352–372. DOI: [10.1111/j.1365-2966.2007.11611.x](https://doi.org/10.1111/j.1365-2966.2007.11611.x). eprint: [astro-ph/0702258](https://arxiv.org/abs/astro-ph/0702258).
- Parmentier, G. and S. Pfalzner (2013). “Local-density-driven clustered star formation.” In: *A&A* 549, A132, A132. DOI: [10.1051/0004-6361/201219648](https://doi.org/10.1051/0004-6361/201219648). arXiv: [1211.1383](https://arxiv.org/abs/1211.1383).
- Peterson, Dawn E. et al. (2011). “The Spitzer Survey of Interstellar Clouds in the Gould Belt. III. A Multi-wavelength View of Corona Australis.” In: *The Astrophysical Journal Supplement Series* 194. DOI: [10.1088/0067-0049/194/2/43](https://doi.org/10.1088/0067-0049/194/2/43).
- Pfalzner, S., G. Parmentier, M. Steinhausen, K. Vincke, and K. Menten (2014). “The Evolutionary Tracks of Young Massive Star Clusters.” In: *ApJ* 794, 147, p. 147. DOI: [10.1088/0004-637X/794/2/147](https://doi.org/10.1088/0004-637X/794/2/147). arXiv: [1408.6021](https://arxiv.org/abs/1408.6021).
- Pfeffer, Joel, J. M. Diederik Kruijssen, Robert A. Crain, and Nate Bastian (2018). “The E-MOSAICS project: simulating the formation and co-evolution of galaxies and their star cluster populations.” In: *MNRAS* 475, pp. 4309–4346. DOI: [10.1093/mnras/stx3124](https://doi.org/10.1093/mnras/stx3124).
- Piskunov, A. E., A. Just, N. V. Kharchenko, P. Berczik, R.-D. Scholz, S. Reffert, and S. X. Yen (2018). “Global survey of star clusters in the Milky Way VI. Age distribution and cluster formation history.” In: *ArXiv e-prints*. arXiv: [1802.06779](https://arxiv.org/abs/1802.06779).
- Plummer, H. C. (1911). “On the problem of distribution in globular star clusters.” In: *MNRAS* 71, pp. 460–470. DOI: [10.1093/mnras/71.5.460](https://doi.org/10.1093/mnras/71.5.460). URL: <http://adsabs.harvard.edu/abs/1911MNRAS...71..460P>.
- Proszkow, E.-M. and F. C. Adams (2009). “Dynamical Evolution of Young Embedded Clusters: A Parameter Space Survey.” In: *ApJS* 185, pp. 486–510. DOI: [10.1088/0067-0049/185/2/486](https://doi.org/10.1088/0067-0049/185/2/486). arXiv: [0910.4679](https://arxiv.org/abs/0910.4679) [astro-ph.SR].
- Rahner, D., E. W. Pellegrini, S. C. O. Glover, and R. S. Klessen (2017). “Winds and radiation in unison: a new semi-analytic feedback model for cloud dissolution.” In: *MNRAS* 470, pp. 4453–4472. DOI: [10.1093/mnras/stx1532](https://doi.org/10.1093/mnras/stx1532). arXiv: [1704.04240](https://arxiv.org/abs/1704.04240).
- (2018). “Forming clusters within clusters: how 30 Doradus recollapsed and gave birth again.” In: *MNRAS* 473, pp. L11–L15. DOI: [10.1093/mnrasl/slx149](https://doi.org/10.1093/mnrasl/slx149). arXiv: [1710.02747](https://arxiv.org/abs/1710.02747).
- Reggiani, M., M. Robberto, N. Da Rio, M. R. Meyer, D. R. Soderblom, and L. Ricci (2011). “Quantitative evidence of an intrinsic luminosity spread in the Orion nebula cluster.” In: *A&A* 534, A83, A83. DOI: [10.1051/0004-6361/201116946](https://doi.org/10.1051/0004-6361/201116946). arXiv: [1108.1015](https://arxiv.org/abs/1108.1015).

- Renaud, F. (2018). “Star clusters in evolving galaxies.” In: *New A Rev.* 81, pp. 1–38. DOI: [10.1016/j.newar.2018.03.001](https://doi.org/10.1016/j.newar.2018.03.001). arXiv: [1801.04278](https://arxiv.org/abs/1801.04278).
- Renaud, F., C. M. Boily, J. J. Fleck, T. Naab, and Ch. Theis (2008). “Star cluster survival and compressive tides in Antennae-like mergers.” In: *MNRAS* 391, pp. L98–L102. DOI: [10.1111/j.1745-3933.2008.00564.x](https://doi.org/10.1111/j.1745-3933.2008.00564.x). arXiv: [0809.2927](https://arxiv.org/abs/0809.2927) [astro-ph].
- Ross, David J., Andrew Mennim, and Douglas C. Heggie (1997). “Escape from a tidally limited star cluster.” In: *MNRAS* 284, pp. 811–814. DOI: [10.1093/mnras/284.4.811](https://doi.org/10.1093/mnras/284.4.811).
- Rossi, L. J., K. Bekki, and J. R. Hurley (2016). “Evolution of star cluster systems in isolated galaxies: first results from direct N-body simulations.” In: *MNRAS* 462, pp. 2861–2877. DOI: [10.1093/mnras/stw1827](https://doi.org/10.1093/mnras/stw1827).
- Salpeter, E. E. (1955). “The Luminosity Function and Stellar Evolution.” In: *ApJ* 121, p. 161. DOI: [10.1086/145971](https://doi.org/10.1086/145971).
- Sharma, Sanjib, Joss Bland-Hawthorn, Kathryn V. Johnston, and James Binney (2011). “Galaxia: A Code to Generate a Synthetic Survey of the Milky Way.” In: *ApJ* 730, 3, p. 3. DOI: [10.1088/0004-637X/730/1/3](https://doi.org/10.1088/0004-637X/730/1/3). arXiv: [1101.3561](https://arxiv.org/abs/1101.3561) [astro-ph.GA].
- Shukirgaliyev, B., G. Parmentier, P. Berczik, and A. Just (2017). “Impact of a star formation efficiency profile on the evolution of open clusters.” In: *A&A* 605, A119, A119. DOI: [10.1051/0004-6361/201730607](https://doi.org/10.1051/0004-6361/201730607). arXiv: [1706.03228](https://arxiv.org/abs/1706.03228).
- Shukirgaliyev, Bekdaulet, Geneviève Parmentier, Andreas Just, and Peter Berczik (2018a). “The Long-term Evolution of Star Clusters Formed with a Centrally Peaked Star Formation Efficiency Profile.” In: *ApJ* 863, 171, p. 171. DOI: [10.3847/1538-4357/aad3bf](https://doi.org/10.3847/1538-4357/aad3bf).
- Shukirgaliyev, Bekdaulet, Genevieve Parmentier, Peter Berczik, and Andreas Just (2018b). “The star cluster survivability after gas expulsion is independent of the Galactic tidal field impact.” In: *MNRAS* (submitted).
- Silva-Villa, E., A. Adamo, N. Bastian, M. Fouesneau, and E. Zackrisson (2014). “The age distribution of stellar clusters in M83.” In: *MNRAS* 440, pp. L116–L120. DOI: [10.1093/mnrasl/slu028](https://doi.org/10.1093/mnrasl/slu028). arXiv: [1402.3595](https://arxiv.org/abs/1402.3595).
- Smith, R., M. Fellhauer, S. Goodwin, and P. Assmann (2011). “Surviving infant mortality in the hierarchical merging scenario.” In: *MNRAS* 414, pp. 3036–3043. DOI: [10.1111/j.1365-2966.2011.18604.x](https://doi.org/10.1111/j.1365-2966.2011.18604.x). arXiv: [1102.5360](https://arxiv.org/abs/1102.5360) [astro-ph.SR].
- Smith, R., S. Goodwin, M. Fellhauer, and P. Assmann (2013). “Infant mortality in the hierarchical merging scenario: dependence on gas expulsion time-scales.” In: *MNRAS* 428, pp. 1303–1311. DOI: [10.1093/mnras/sts106](https://doi.org/10.1093/mnras/sts106). arXiv: [1210.0908](https://arxiv.org/abs/1210.0908) [astro-ph.SR].
- Spitzer, Lyman (1987). *Dynamical evolution of globular clusters*.
- Spurzem, R., M. Giersz, K. Takahashi, and A. Ernst (2005). “Anisotropic gaseous models of tidally limited star clusters: comparison with other methods.” In: *MNRAS* 364, pp. 948–960. DOI: [10.1111/j.1365-2966.2005.09631.x](https://doi.org/10.1111/j.1365-2966.2005.09631.x). arXiv: [astro-ph/0412698](https://arxiv.org/abs/astro-ph/0412698) [astro-ph].

- Takahashi, K. and S. F. Portegies Zwart (2000). "The Evolution of Globular Clusters in the Galaxy." In: *ApJ* 535, pp. 759–775. DOI: [10.1086/308857](https://doi.org/10.1086/308857). eprint: [astro-ph/9903366](https://arxiv.org/abs/astro-ph/9903366).
- Tanikawa, Ataru and Toshiyuki Fukushige (2005). "Mass-Loss Timescale of Star Clusters in an External Tidal Field. I. Clusters on Circular Orbits." In: *Publications of the Astronomical Society of Japan* 57, pp. 155–164. DOI: [10.1093/pasj/57.1.155](https://doi.org/10.1093/pasj/57.1.155). arXiv: [astro-ph/0409148](https://arxiv.org/abs/astro-ph/0409148).
- Teuben, P., R. A. Shaw, H. E. Payne, and J. J. E. Hayes (1995). "The Stellar Dynamics Toolbox NEMO." In: *Astronomical Data Analysis Software and Systems IV*. Vol. 77, p. 398.
- Tutukov, A. V. (1978). "Early Stages of Dynamical Evolution of Star Cluster Models." In: *A&A* 70, p. 57.
- Verschueren, W. and M. David (1989). "The effect of gas removal on the dynamical evolution of young stellar clusters." In: *A&A* 219, pp. 105–120.
- Vesperini, E. and S. E. Zepf (2003). "Effects of the Dissolution of Low-Concentration Globular Clusters on the Evolution of Globular Cluster Systems." In: *ApJ* 587, pp. L97–L100. DOI: [10.1086/375313](https://doi.org/10.1086/375313). eprint: [astro-ph/0305343](https://arxiv.org/abs/astro-ph/0305343).
- Wang, Long, Rainer Spurzem, Sverre Aarseth, Mirek Giersz, Abbas Askar, Peter Berczik, Thorsten Naab, Riko Schadow, and M. B. N. Kouwenhoven (2016). "The DRAGON simulations: globular cluster evolution with a million stars." In: *MNRAS* 458, pp. 1450–1465. DOI: [10.1093/mnras/stw274](https://doi.org/10.1093/mnras/stw274).
- Whitmore, B. C. (2017). "Universal and Environmental Influences on Star Clusters." In: *Formation, Evolution, and Survival of Massive Star Clusters*. Ed. by C. Charbonnel and A. Nota. Vol. 316. IAU Symposium, pp. 202–207. DOI: [10.1017/S1743921315010522](https://doi.org/10.1017/S1743921315010522).
- Whitmore, B. C., R. Chandar, and S. M. Fall (2007). "Star Cluster Demographics. I. A General Framework and Application to the Antennae Galaxies." In: *AJ* 133, pp. 1067–1084. DOI: [10.1086/510288](https://doi.org/10.1086/510288). eprint: [astro-ph/0611055](https://arxiv.org/abs/astro-ph/0611055).

أَلْحَمْدُ لِلَّهِ رَبِّ الْعَالَمِينَ ﴿١﴾ الرَّحْمَنِ الرَّحِيمِ

(The Quran, 1:2-3)

ACKNOWLEDGMENTS

First and foremost, I would like to thank my supervisor PD Dr. Geneviève Parmentier for offering the project, for her guidance, her confidence in my work, for her spending her time on long discussions, rehearsals of my talks, improving my English and also the generous support throughout my PhD time. This is very much appreciated!

I want to thank my co-supervisor apl. Prof Andreas Just, for his guidance, the numerous helpful discussions and many useful advices and support during my studies.

My deep gratitude goes to Dr. Peter Berczik, who always was available for discussions, answers even being on the other side of the Planet by on-line, for his useful advices and kind support in all aspects of life.

I am also thankful to Prof. Ralf Klessen for kindly agreeing to be the second referee of this thesis, and to Prof. Björn Malte Schäfer and PD Dr. Thorsten Lisker for agreeing to be part of the examination committee.

I express my gratitude to Dr. Christian Fendt and the International Max-Planck Research School (IMPRS) for providing this great opportunity to do PhD research in Heidelberg, helping with solving bureaucratic issues, for welcoming and providing the financial support with the accommodation during the first month stay in Heidelberg. My gratitude to Prof. Dr. Eva Grebel for her being very kind and for the financial support provided though the work contract in the framework of SFB 881 "The Milky Way System" (subproject B2). I would like to thank Dr. Glenn van de Ven for his agreement to be a member of my thesis committee and very useful discussions and comments on the process of my PhD research project. I gratefully acknowledge Prof. Dr. Rainer Spurzem for his support, advices and for providing access to the high-performance computing clusters (JURECA in Jülich Computing Center, Germany and LAOHU in NAOC/CAS, China) where I ran my large simulations. I also gratefully acknowledge Prof. Dr. Walter Dehnen (University of Leicester, UK) for his support and discussions in connection with implementing the code MKHALO for the purposes of this thesis, Prof. Dr. Rupali Chandar (University of Toledo, OH, USA) for stimulating discussions. My special gratitude goes to Dr. Chingis Omarov, who involved me into international collaborative Project STARDISK between Kazakhstan and Germany, which was my starting point into consequent research works and this PhD study, and also for he always supports me in my research works. I also acknowledge my colleagues in Fesenkov Astrophysical Institute for their kind support and helpful discussions.

I also would like to acknowledge the Graduate Academy Service Center and the Welcome Center of the University of Heidelberg for their help with solving the issues regarding the visa and permission to stay in Germany. In particular, I thank Chiara Rottaro for finding the useful pieces of the German law.

All of the ARI staff has contributed to a very nice and positive work environment and I would like to thank in particular Martina Buchhaupt, Besma Klinger-Araifa, Eleonora Grauer, Saskia Mayer, Helga Ballmann, Hildrun Pisch, and Diana Schwalbe for their help in all administrative issues, Dr. Peter Schwekendiek and Sven Weimann for the help in sorting out IT

problems, Dr. Robert Schmidt, Dr. Guido Thimm and Dr. Anna Pasquali for always being available to answer any of my questions.

I would also like to thank the other PhD students with whom I shared this experience and a lot of cheerful moments. In particular, I thank my officemates, Frederik, Clio, and Gergely who were always available for helpful discussions and chats. My special gratitude to my friend and colleague from Kazakhstan, Taras Panamarev for his help, support and many useful discussions, for his friendship. I gratefully acknowledge my friend Daniel Rahner, who immediately agreed and translated into German the abstract of this thesis. I thank all my friend and colleagues in Heidelberg.

A special acknowledgment goes to my parents and sisters for providing a world of possibilities, love, and understanding without which this work would not have been possible. Last but certainly not least, I would like to express the deepest of all gratitudes to Aigerim, my love, my soulmate, my wingman. Thank you for your tireless support even in the most difficult situations, for your cheerful attitude, for numerous tasty cakes and cookies, for coming to Germany with me and creating a small paradise at home. You have become such an important part of my life!

This work was supported by Sonderforschungsbereich SFB 881 “The Milky Way System” (subproject B2) of the German Research Foundation (DFG).

I also acknowledge the use of supercomputers of the Jülich Supercomputing Center (JSC) JURECA (hhd28), of the Baden-Württemberg HPC infrastructure (bwforCluster, national and state funded through grant INST 35/1134-1 FUGG, and funded by SFB 881), of the KEPLER GPU cluster funded by Volkswagen foundation project I/81 396, and of NAOC/CAS (LAOHU at Center of Information and Computing).

